Investigation and computation of the interface dynamic during magnetic pulse welding

Jishuai Li

▶ **To cite this version:**

Jishuai Li. Investigation and computation of the interface dynamic during magnetic pulse welding. Mechanics of materials [physics.class-ph]. Université de Technologie de Compiègne, 2021. English. NNT : 2021COMP2598 . tel-03613573

HAL Id: tel-03613573

https://theses.hal.science/tel-03613573v1

Submitted on 18 Mar 2022

HAL is a multi-disciplinary open access archive for the deposit and dissemination of scientific research documents, whether they are published or not. The documents may come from teaching and research institutions in France or abroad, or from public or private research centers.

L'archive ouverte pluridisciplinaire **HAL**, est destinée au dépôt et à la diffusion de documents scientifiques de niveau recherche, publiés ou non, émanant des établissements d'enseignement et de recherche français ou étrangers, des laboratoires publics ou privés.

Par **Jishuai LI**

Investigation and computation of the interface dynamic during magnetic pulse welding

Thèse présentée
pour l'obtention du grade
de Docteur de l'UTC

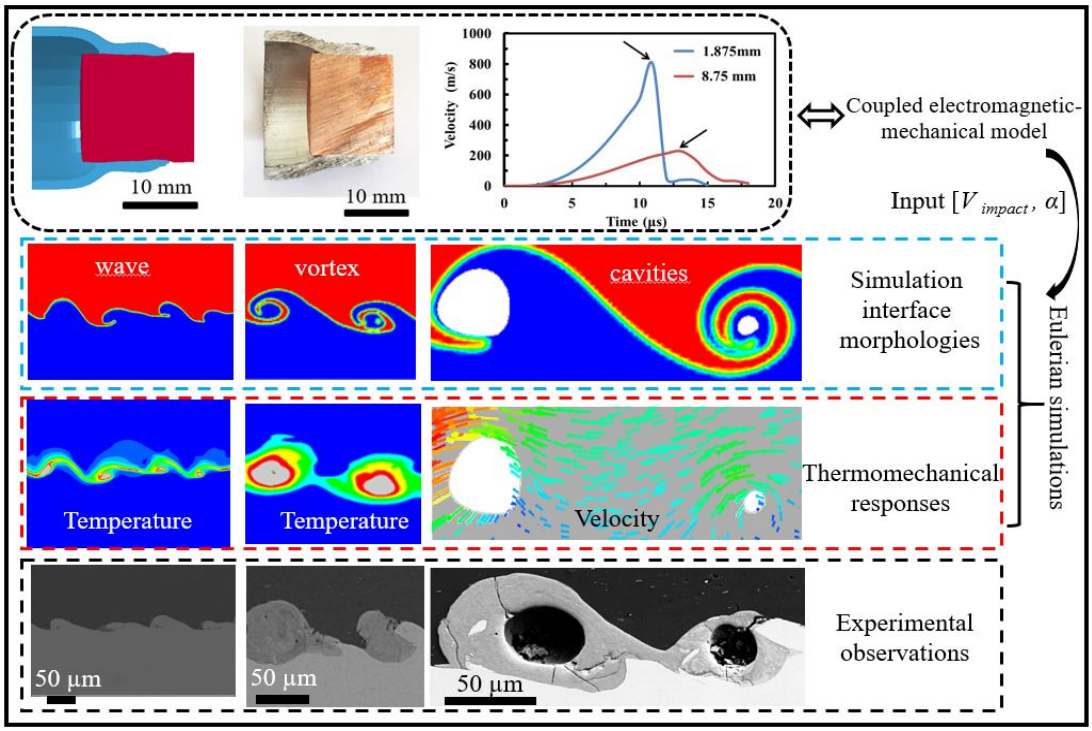

Soutenue le 25 mars 2021
Spécialité : Mécanique et Matériaux : Unité de recherche en Mécanique - Laboratoire Roberval (FRE UTC - CNRS 2012)
D2598

Investigation and computation of the interface dynamic during magnetic pulse welding

Jishuai LI

Laboratoire Roberval, CNRS UMR 7337

Sorbonne Universités, Université de Technologie de Compiègne

25 mars 2021

Spécialité : Mécanique et Matériaux

Composition of the Jury

Reviewers:
François BAY, Professeur des Universités, CEMEFMINES ParisTech, France
Sachin KORE, Professeur des Universités, Indian Institute of Technology Goa, Indian

Examiners:
Verena PSYK, Professeur Fraunhofer Institute for Machine Tools and Forming Technology IWU, Germany
Mario FAFARD, Professeur des Universités, Université Laval, Canada
Jérôme FAVERGEON, Professeur des Universités, Université de Technologie de Compiègne, France
Rija Nirina RAOELISON, Maitre de Conférences, Université de Technologie de Belfort-Montbéliard, France (Co-Supervisor)
Mohamed RACHIK, Maitre de Conférences, HDR, Université de Technologie de Compiègne, France (Supervisor)

Invited members:
Aude SIMAR, Professeur des Universités, Université catholique de Louvain, Belgium
Guillaume RACINEUX, Professeur des universités, Ecole Centrale de Nantes, France
Thaneshan SAPANATHAN, Chargé de recherche FNRS, Université catholique de Louvain, Belgium

This thesis is lovingly dedicated to my parents, my sister and my fiancée for their love, encouragement and support

Acknowledgments

Saying thank you is probably very little compared to everything that I have received from my supervisors, colleagues, friends and my family during all these years of my thesis. But I still think it is important at this special moment to find some words to say thank you. Let me first simple to say: Thank you to all of you.

I would like to express my sincere gratitude for my two supervisors, Prof. Mohamed Rachik and Prof. Rija-Nirina Raoelison. Thank you all for trusting me from the start of this journey and for giving me a lot of freedom in my daily work. Mohamed, thank you always for encouraging and supporting me to participate academic activities and to go for a research stay at Université catholique de Louvain (UCLouvain), Belgium, which expand my knowledge and enrich my experience. The lively discussions as well as the trip to Nantes will remain as wonderful memories of these years. Rija, thank you for your tireless encouragement and the time you have always taken for me. Thank you for always treating me as a friend more than a PhD candidate under your supervision. Without you, the thermomechanical models of this thesis would not have taken a much exciting. Dear Mohamed and Rija, your scientific and human qualities will remain as good examples to me and that I will try my best to follow in my future professional life.

I am grateful to Prof. Francois Bay and Prof. Sachin Kore for carefully reading my thesis, and providing valuable comments and suggestions. I am honored that Prof Verena Psyk, Prof. Mario Fafard and Prof. Jérôme Favergeon agreed to be the juries of my PhD work. Thanks for their interest, I really appreciate it.

I would like to thank Prof. Aude Simar, Dr. Thaneshan Sapnathan, Dr. Audrey Favache, whom I worked at UCLouvain, during my research stay. Thanks to Thaneshan, from day one, I obtained continuous help from him and he also introduced me to UCLouvain. He answered me a lot of questions by phone calls and emails not only just about scientific but also about life. The numerous discussions on weekday or weekend will always remain in my mind and continue to motivate me to pursue

higher-quality researchers. Thanks to Aude, she was my supervisor at UCLouvain and provided valuable discussions for my experimental work and also helped me to improve my academic writing skills. Thanks to Audrey for her discussions on nanoindentaion experimental work. I would also like to thank Prof. Yuliang Hou, who works in Zhengzhou University, for his valuable comments, passion and rigorous attitude in our collaboration.

I would like to thanks to Prof. Daniel Marceau, Prof. X. Grant Chen and Dr. Zhan Zhang, who work at Université du Québec à Chicoutimi, Canada. They provided the TEM data and gave me many valuable discussions. I also would like to thank Prof Guillaume Racineux, who works at Ecole Centrale Nantes. He introduced me to many experimental equipment that related to MPW which helped me more intuitive understanding this welding process.

I would like to thank Caroline Verdari for her training on SEM and assisting me in metallurgical sample preparation and Isabelle Velluet for her help to teach me how to use the micro chain saw cutting machine. I also want to thank Prof. Pirre-Emmanuel Mazeran for his help on nanoindentation tests at UTC.

I would like to thank my nice friends from UTC, with whom I have shared these wonderful memorable years. They always encouraged me to express my ideas loudly and confidently in my second or third language and gave me help whenever I need during my study abroad. Special, thanks to Adelita, Baptiste, Corentin, Cong Uy, Dong, Ernesto, Guoqiang, Hussein, Ivan, Jichang, Julie, Ke, Khalil, Maiqi, Mekro, Phong, Tea, Xiang Jun, Xingyi, Ye, Yunbo et al.-there has always been time for sports, a coffee or a drink to share, I am really grateful for that.

I would like to also thank China Scholarship Council (CSC) for the financial support during my PhD. Without it I cannot finish my PhD research. It is a great honor for me to obtain this Scholarship. Thank you so much my motherland and wish you thriving prosperity. I would also thank the Doctoral School of UTC for offering a financial support during my research stay at UCLouvain.

Last but not least, I would like to dedicate the following text to thank my family. Mom and dad, thank you for your endless love, and for supporting me each step and each choice that I have made so far. My elder sister, Jing, thank you for your continuous encouragement, and for taking care of our parents, which made me to concentrate on my research during my study abroad. My fiancée, Na, thank you for your great understanding, for believing in me and accompany with me these years. Your love is my source of courage to face the difficulties of each day. Although we are thousands of miles apart during my PhD research, our hearts are very close. I am looking forward to explore and experience more adventure with you in future.

Contents

Abstract

Joining dissimilar metals with different thermal properties using traditional fusion welding processes remains a challenging task. Magnetic pulse welding (MPW) is a solid state process that enables to join dissimilar metals using high speed impact without creating a weld pool. MPW involves multiphysics phenomena under fast dynamic conditions that affect the joint. The aim of this thesis is to understand the mechanisms, thermomechanical kinetics and metallurgical changes at the interface during Al/Cu MPW.

The effects of the field-shaper materials and input discharge voltage on the microstructure and local mechanical behaviours of the joints were investigated. A coupled electromagnetic-mechanical model was used to predict the impact velocity and impact angle along the whole welding interface at macroscopic scale, and they were used to understand the impact kinematics and the physics behind the formation of various welding zones of the joint. The obtained impact conditions were then analysed using thermomechanical simulation based on Eulerian formulation. These thermomechanical simulations helped to understand the local microstructural evolutions, and in particular the interface morphologies, to the development of thermomechanical and kinematics field variables within the material, particularly at and around the interface. The structural changes within the interface were depicted depending on governing parameters. Finally, we established the material/process interactions that govern the behaviour of MPW to predict and specify the weldability conditions for Al/Cu MPW combination.

The experimental and computational investigations of the interface dynamic enable to comprehensively understand the fundamental mechanism, thermomechanical kinetics and consequences of interface instabilities in MPW. Moreover, they efficiently contribute to bridge the gap between scientific research and industrial application of MPW.

List of publications

[J1] **J.S. Li**, R.N. Raoelison, T. Sapanathan, G. Racineux, M. Rachik. Assessing the influence of field-shaper material on magnetic pulse welded interface of Al/Cu joints. Procedia Manufacturing, Vol 29, pp. 337-344, 2019. https://doi.org/10.1016/j.promfg.2019.02.146

[J2] R. N. Raoelison, **J.S. Li**, T. Sapanathan, E. Padayodi, N. Buiron, D. Racine, Z. Zhang, D. Marceau, M. Rachik. A new nature of microporous architecture with hierarchical porosity and membrane template via high strain rate collision. Materialia, 5 (2019) 100205. https://doi.org/10.1016/j.mtla.2018.100205

[J3] **J.S. Li**, T. Sapanathan, R.N. Raoelison, Z. Zhang, X. G. Chen, D. Marceau, A. Simar, M. Rachik. Inverse prediction of local interface temperature during electromagnetic pulse welding via precipitate kinetics. Materials Letters, 249 (2019) 177-179. https://doi.org/10.1016/j.matlet.2019.04.094

[J4] **J.S. Li**, R.N. Raoelison, T. Sapanathan, Z. Zhang, X. G. Chen, D. Marceau, Y.L. Hou, M.Rachik, An anomalous wave formation at the Al/Cu interface during magnetic pulse welding. Applied Physics letters, 116 (2020), 161601. https://doi.org/10.1063/5.0005299

[J5] **J.S. Li**, R.N. Raoelison, T. Sapanathan, Y.L. Hou, M. Rachik, Interface evolution during magnetic pulse welding under extremely high strain rate collision: mechanisms, thermomechanical kinetics and consequences. Acta Materialia, 195 (2020), 404-415. https://doi.org/10.1016/j.actamat.2020.05.028

[J6] **J.S. Li**, T. Sapanathan, R.N. Raoelison, Y.L. Hou, A. Simar, M. Rachik, On the complete interface development for Al/Cu magnetic pulse welding via experimental characterizations and multiphysics numerical simulations, Journal of Materials Processing Technology, 296 (2021), 117185. https://doi.org/10.1016/j.jmatprotec.2021.117185

List of conference participations

[C1] **J.S. Li**, R.N. Raoelison, T. Sapanathan, G. Racineux, M. Rachik. Assessing the influence of field-shaper material on magnetic pulse welded interface of Al/Cu joints. 18th International Conference on Sheet Metal, Leuven, Belgium, April 15th-17th, 2019.

[C2] **J.S. Li**, R.N. Raoelison, T. Sapanathan, M. Rachik. A coupled thermal-mechanical model based on Eulerian formulation for magnetic pulse welding, VIII International Conference on Coupled Problems in Science and Engineering, Sitges (Barcelona), Spain, 3-5 June 2019.

[C3] **J.S. Li**, R.N. Raoelison, T. Sapanthan, M. Rachik, A predictive and reliable Eulerian model to compute the interfface kinetics of magnetic pulse welding, Numiform 2019: The 13th International Conference on Numerical Methods in Industrial Forming Processes, Portsmouth, New Hamphire, USA, 23-27 June 2019

[C4] R. N. Raoelison, **J.S Li**, T. Sapanathan, M. Rachik, Instabilités à forte vitesse de déformation lors de collisions balistiques en soudage par impact et conséquences structurales thermomécaniques, Le 28e congrès annuel de la Société Française de Thermique, June 2020, Belfort, France, https://doi.org/10.25855/SFT2020-064.

List of acronyms

Acronyms	Description
ALE	Arbitary Lagrangian-Eulerian
AP	Amorphous phase
BEM	Boundary element method
BSE	Backscattered Electron
CEMM	Coupled electromagnetic-mechanical
DOF	Degree of freedom
EDS	Energy-dispersive X-ray spectroscopy
EXW	Explosive welding
FEM	Finite element method
FS	Field-shaper
HAZ	Heat affected zone
HSIW	High speed impact welding
IM	Intermediate
IMC	Intermetallic compound
IMZs	Intermediate zones
IPAZ	Intermediate phase affected zone
IZ	Interface zone
K-H	Kelvin–Helmholtz
MD	Molecular dynamic
MPW	Magnetic pulse welding
OM	Optical microscope
PDV	Photon Doppler velocimetry
SAED	Selected area electron diffraction
SE	Secondary Electron
SEM	Scanning electron microscope
SP	Stagnation point
SPH	Smooth particle hydrodynamics
TEM	Transmission Electron Microscopy
WZ	Wavy zone

List of Latin symbols

Symbol	Description
E	discharge energy
C	capacitance of the bank capacitor
U	discharge voltage
μ_0	magnetic permeability
k	coefficient depending on the geometry of the coil
n	the number of coil turn
U	discharge voltage
C	capacitance of the bank capacitor
L	inductance of the discharge circuit system
R	resistance of the discharge circuit system
l_w	the length of the coil working zone
δ	skin depth
ρ'	the electrical resistivity of the flyer
f *(HZ)*	discharge current frequency
$\vec{E}$	electric field
$\vec{B}$	magnetic flux density
$\vec{H}$	magnetic field intensity
$\vec{J}$	total current density
ε	electrical permittivity
ρ	total charge density
ρ_0	mass density
σ	electrical conductivity
$\overrightarrow{J_s}$	source current density
μ	magnetic permeability
$\emptyset$	the electric scalar potential
$\vec{A}$	the magnetic vector potential
σ_y	the yielding stress
ε_p	the effective plastic strain
$\dot{\varepsilon}_p$	the effective plastic strain rate
$\dot{\varepsilon}_{p0}$	the reference strain rate
A	Initial yield strength
B	Hardening coefficient

Symbol	Description
C	Strain rate constant
n	Strain hardening exponent
m	Softening exponent
T^*	the dimensionless temperature
T_o	Reference temperature
T_m	Melting temperature
s	Slope of linear Rankine–Hugoniot's law
$\gamma 0$	Mie-Grüneisen's coefficient
G	Shear modulus
ρ_1	Reference mass density
Cp	Specific heat capacity
λ	Thermal conductivity
$\vec{\mu}$	Velocity vector
$\underline{\sigma}$	Cauchy stress
$\vec{F_v}$	Internal body force vector
$\underline{D}$	Strain rate tensor
e	Specific internal energy
V_{impact}	Impact velocity
α	Impact angle

List of Tables

List of Figures

Chapter 1

Introduction

1.1. General context

Hybrid metallic structures are growing in high demands in modern engineering applications since they can improve performances [1–3], such as light weighting, structural reinforcements, or other specific functionalization. The bimetallic aluminium to copper combinations are typical examples of such hybrid structures that are particularly attractive for electric power, electronic and piping applications due to their excellent corrosion resistance, thermal properties and electrical conductivity [4].

The use of dissimilar metal combinations in industries can be limited by the materials joining technology. Welding is one of the usual method to join dissimilar metals and it has been widely used in many applications, such as the construction of automotive, gasoline pipeline and aircraft [5–8]. However, the conventional fusion welding processes of dissimilar metals can be laborious when the joined metals exhibit very different melting temperature and it can suffer from intermetallic compound (IMC) layers formation that results from phase changes caused by the dissimilarities in thermal and mechanical properties between the metal pairs. These IMC layers usually contain solidification defects (cracks, porosities) that can deteriorate the mechanical properties of the joint. Therefore, a safer welding solution is necessary to join the dissimilar metals.

Thus, solid-state welding methods become attractive alternatives and they provide efficient multi-metallic joints without the typical defects of fusion welds. However, most common friction-based solid state welding methods inevitably introduce heat affected zones (HAZ) [9,10]. Impact welding offers the advantages of obtaining dissimilar joints without HAZ under appropriate welding conditions. Hence, impact welding is already used for specific applications of many industries. The

impact welding processes include pressure-driven using explosives (explosive welding) [11–13], electromagnetic impulse (magnetic pulse welding) [14,15], laser impulse (laser impact welding) [16,17] or vaporization (vaporizing foil actuator welding) [18,19]. Among these impact welding methods, magnetic pulse welding (MPW) is especially growing in automotive and electrical industries, due to its environmental friendliness, flexibility and capability to join dissimilar lightweight metals [20]. MPW uses pressure to accelerate one metal impact into another fixed metal and then creates a weld. Furthermore, it was demonstrated that the MPW process can work with a robot to produce a weld in various positions similarly to industrial welding processes, that means MPW can be applied under mass production conditions.

MPW completes within very short process (commonly within 100 μs) along with high-speed collision, while the interface is subjected to an extremely high strain rate of 10^6–10^7 s^{-1} [21,22]. The velocity is usually limited to 1000 m/s in practical application to maintain the service life of the tools (e.g. coils and field-shaper) and to lower the input power requirements [23]. During the process, the welding is governed by the collision velocity and the collision angle [24,25].

Therefore, it is foreseeable that a complex kinematics and thermomechanical kinetics occur at the interface, especially for MPW of dissimilar materials due to the mismatch of strain hardening and thermal expansion coefficients during the instantaneous high-speed collision. Moreover, the weld characteristics in MPW strongly depend on the multi-physics and transient response of the interface material. However, the high speed of this process makes it almost impossible to directly obtain the experimental observation to investigate the dynamic interaction of the contact interface. Many aspects of the MPW process and of the ensuing bonding mechanism are still investigated and require further studies, especially regarding the complex interface behaviours for MPW dissimilar material combinations. Therefore, a better understanding and prediction of the interface dynamic phenomena is crucial to gain proficiency on the optimization of the MPW process. For this purpose, modelling and

simulation of the MPW process can thus be used to gain a better insight into the relevant interface dynamic phenomena.

1.2. Research objectives and proposed methodologies

The main objective of this PhD work is to investigate the interface dynamic phenomena during MPW of dissimilar metals. This will be studied across metallurgical characterizations and numerical simulations. The proposed methodologies are shown in Fig. 1.1. During MPW, the flyer behaviour which is mainly governed by the electromagnetic field determines the impact velocity and impact angle prior to the collision. These impacts conditions govern the interfacial phenomena. Therefore, a coupled electromagnetic-mechanical computation is performed to obtain the spatial and temporal evolution of velocity at macroscopic scale. This model will be validated with welding samples. The impact conditions will be analysed using an Eulerian simulation that is found to be a suitable and powerful method for investigating the multi-physics and transient response of the interface at microscopic scale [26,27]. The Eulerian models will be validated with experiment observation of the interface. Then one can deeply investigate the development of thermomechanical and kinematic field variables within the material, particularly in the welded interface vicinity. Then, the structural changes within the interface will be depicted depending on the governing parameters that can provide guidelines for parameter selection at the process level. Meantime, it will investigate the impact of MPW on the microstructure and mechanical behaviours under different processing conditions using optical microscope (OM), scanning electron microscope (SEM), energy-dispersive X-ray spectroscopy (EDS), transmission electron microscopy (TEM) and nanoindentation analysis. Finally, we will establish the material/process interactions that govern the behaviour of MPW to predict and specify the weldability conditions for Al/Cu joints produced by MPW.

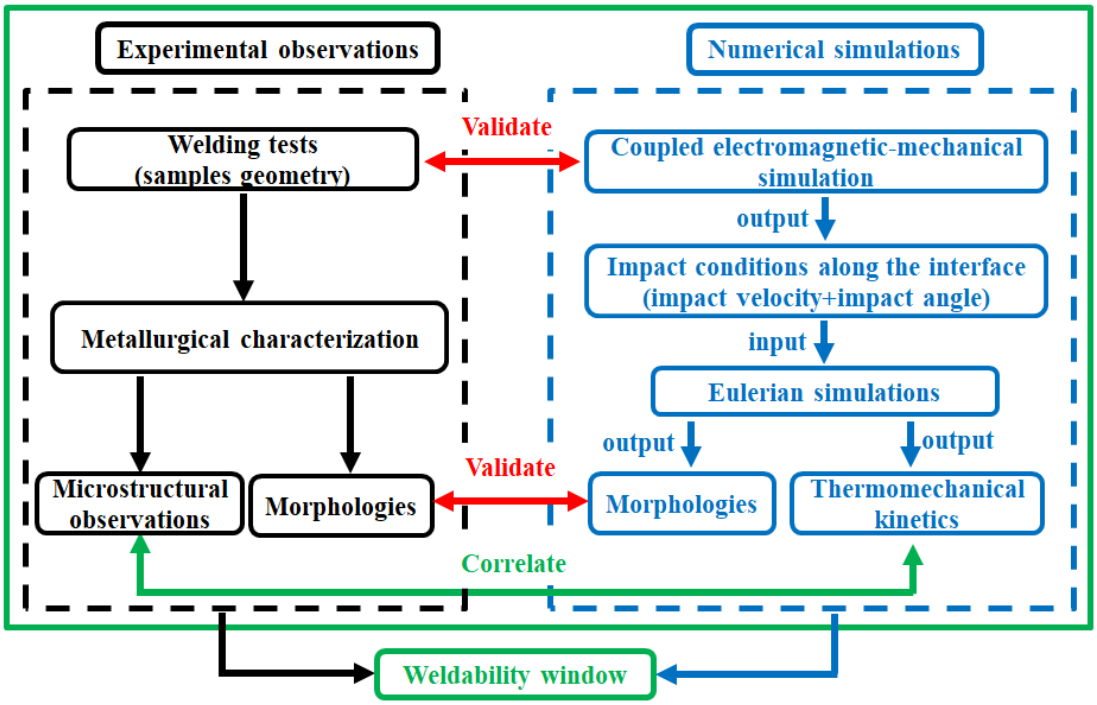

Fig.1.1 Illustration of the experimental procedures and the multiscale and multi-physics modelling strategies used for the MPW analysis in this PhD works.

1.3. Thesis outline

The previous paragraphs have already presented a general introduction about the thesis, including the background, research objectives and proposed methodologies. For the sake of completeness, the structure of the PhD works is described in the following text:

The next chapter addresses a general description of the MPW process, and then a literature review on the formation mechanisms of the wavy interface which is generally regarded as a guarantee of successful welding. This review will also report numerical and simulation of mechanisms and thermomechanical kinematics responsible for the complex morphologies at the interface. Thereafter, the notion of weldability is included in the review so that this chapter can help to understand the current research and to situate our contribution.

The chapter 3 focuses on the effects of field-shaper material and input voltage on microstructure evolution during MPW. The interface microstructure will be

investigated by micro-scale and nano-scale characterizations. Local mechanical behaviours at the interface of Al/Cu magnetic pulse welds were investigated using nanoindentation test. Observations and recommendations were addressed. The findings not only provide a theoretical basis for fundamental welding principle of MPW, but also bring guidance for microstructure optimization for the fabrication of good welds.

In chapter 4, a coupled electromagnetic-mechanical model is proposed to determine the impact angle and impact velocity along the interface during the MPW process. Eulerian simulation models are then proposed to compute the complex interface behaviours. A description of these numerical models, including governing equations, boundary conditions and numerical implementations is provided.

The chapter 5 focuses on the investigation of various types of waves formation under low impact intensity during Al/Cu MPW. In this chapter, it will present four types of waves from my experimental results (chapter 3) and will attempt to explain their formation mechanisms using numerical simulations. A high-fidelity thermomechanical model enables to predict various types of waves. Temperature distribution, averaged equivalent plastic strain, history of thermomechanical kinetics, development kinematics and shear instability at the wavy interface will be investigated, in addition to analysis of relationship between the wave morphology and the jetting kinematics, collision pressure and collision velocity.

The chapter 6 is devoted to a study of interface evolution under extremely high strain rate collision. To elucidate the formation mechanisms of experimentally observed wakes, vortices, swirls and mesoscale cavities under extremely high strain rate collision, a local coupled thermomechanical analysis will be performed. This numerical approach is suitable to describe the fluid-like behaviour of the solid material using Kelvin-Helmholtz instability and successive developments of wakes and vortices confined within the interface zone (within 100 μm). This approach will be discussed in terms of the capability of predicting the interfacial instabilities of dissimilar welds with high fidelity that enables to understand the fundamental

mechanisms, thermomechanical kinetics and consequences of interface instabilities in MPW.

In chapter 7, it is recommended to use the local coupled thermomechanical model to build a weldability window which gives an operative welding range.

In chapter 8, it will give some concluding remarks on the work carried out in the course of the thesis and provides perspectives for future research on this subject. Note that results of chapter 3, 4, 5 and 6 were published in peer reviewed papers [J1] and [J4-J6].

Chapter 2

State of the art

2.1 Abstract

The first chapter of this report addresses the need to investigate the interface dynamic phenomena during MPW of Al/Cu combinations. This chapter presents a complementary review of further aspects of this subject. The general understanding of the MPW process, including principle, potential applications and processing parameters are briefly described. Then, literature review that focuses on the experimental aspects of interface dynamics will report both issues and challenges, including the formation mechanisms of the wavy interface during MPW. A detailed discussion of numerical models and simulation of the complex interfacial morphologies and interfacial parameters is then presented with the notion of weldability window. Finally, a conclusion will summarise the main points of our investigations.

2.2 Magnetic pulse welding

2.2.1 Principle of the magnetic pulse welding process

The MPW principle was patented by Lysenko *et al.* in the 1970s [28] and is phenomenologically similar to explosive welding (EXW) which was discovered several years before. Both methods create a metallurgical joint using a high-speed impact of the workpieces under controlled conditions. However, MPW is cleaner and safer than the EXW due to the use of an electromagnetic impulse as driving force instead of a detonation such as in EXW. Fig. 2.1 shows the typical MPW discharge system. It includes a high voltage supply, a capacitor bank, a gap switch and a coil. In the outside area, a control system and trigger system are installed. The gap switch is used to connect the capacitor bank and the coil so that a current discharge delivered

by the capacitor bank will pass through the coil once the gap switch is closed.

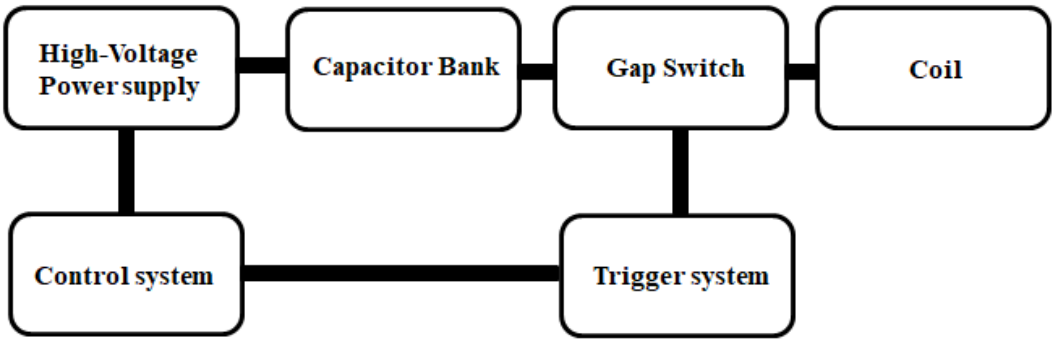

Fig. 2.1 MPW process [29].

The typical architecture of MPW for tubular assemblies is illustrated in Fig. 2.2. It consists of a pulse generator and a workstation. The pulse generator consists of a high-power source, an electrical capacitor and a discharge switch. It is designed to store unusual high electrical energy. The workstation contains a coil, an optional field-shaper to concentrate the magnetic field in the working area, and workpieces (a flyer and an inner fixed part).

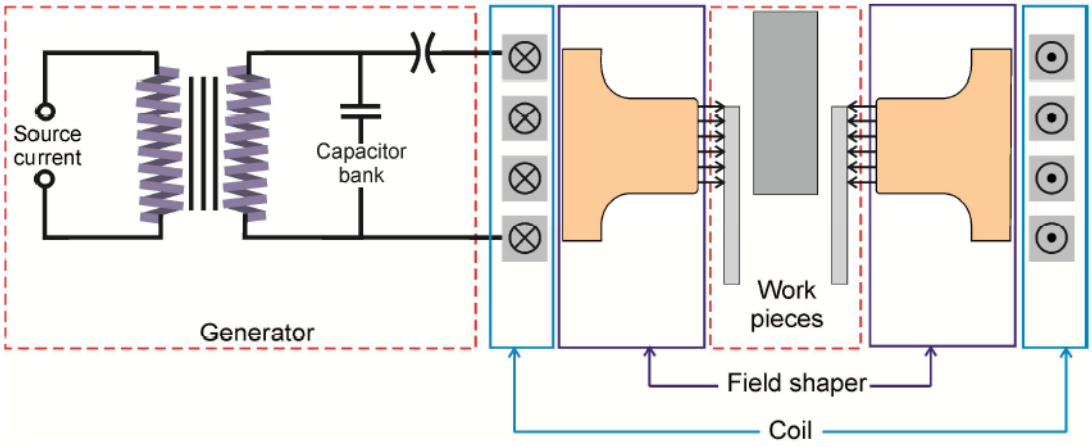

Fig. 2.2 A typical MPW setup for tubular assemblies [20].

MPW process is based on Ampere's law which establishes that force can be generated by separated parallel conductors carrying currents I_1 and I_2. Fig. 2.3 illustrates the principle of MPW for tubular set-up. A high primary current (up to 1.6 MA) produces an electrical charge stored in the capacitor bank [30]. Then, the discharge is released during few microseconds. A magnetic field is thus created by the coil which in turn generates an eddy current on the outer surface of the flyer metal

(outer conductor) placed inside the coil. The interaction of this induced eddy currents with the magnetic field around the flyer results in a Lorentz force that accelerates the flyer towards the inner part, leading to a high-speed collision between the two parts (flyer and fixed part).

During the high velocity impact collision, the interfacial pressure brings the surface atoms into an intimate contact [23,31]. If the impact creates the suitable combination of impact angle and velocity, a jetting phenomenon is created and subsequently mechanical interlocking or chemical bonding takes place at the interface and finally successful welding joint is produced.

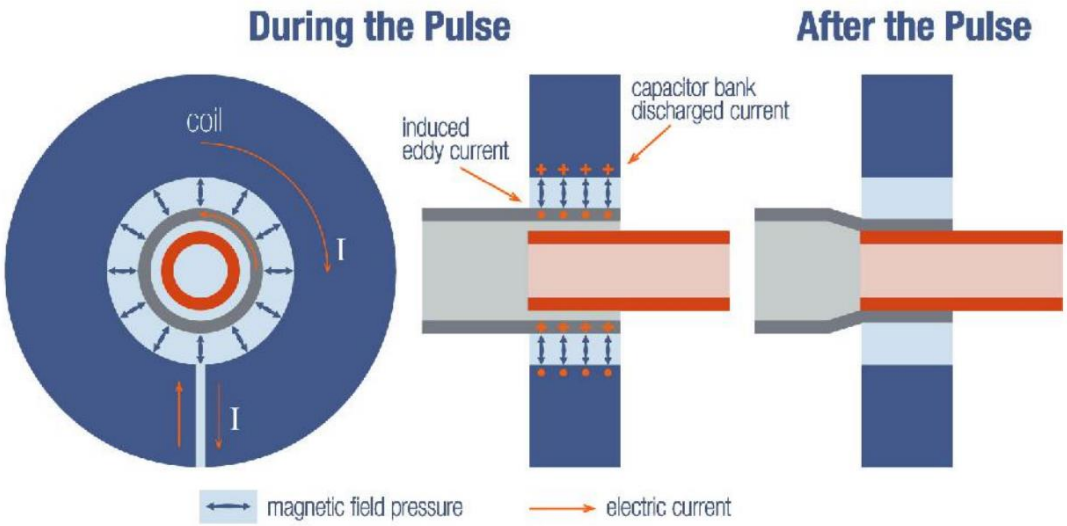

Fig. 2.3 Principle of the high-speed MPW process [30].

2.2.2 Potential applications of magnetic pulse welding

The MPW technique was initially developed to weld components of nuclear fuel rods particularly the closing caps and end closers as illustrated in Fig. 2.4 [32]. In spite of 50 years of development, there is a renewed interest an important investigation of MPW by the end of twentieth century (Fig. 2.5). MPW is receiving a growing interest according to the scientific publications [33].

Fig. 2.4 End enclosures for nuclear fuel rods [32].

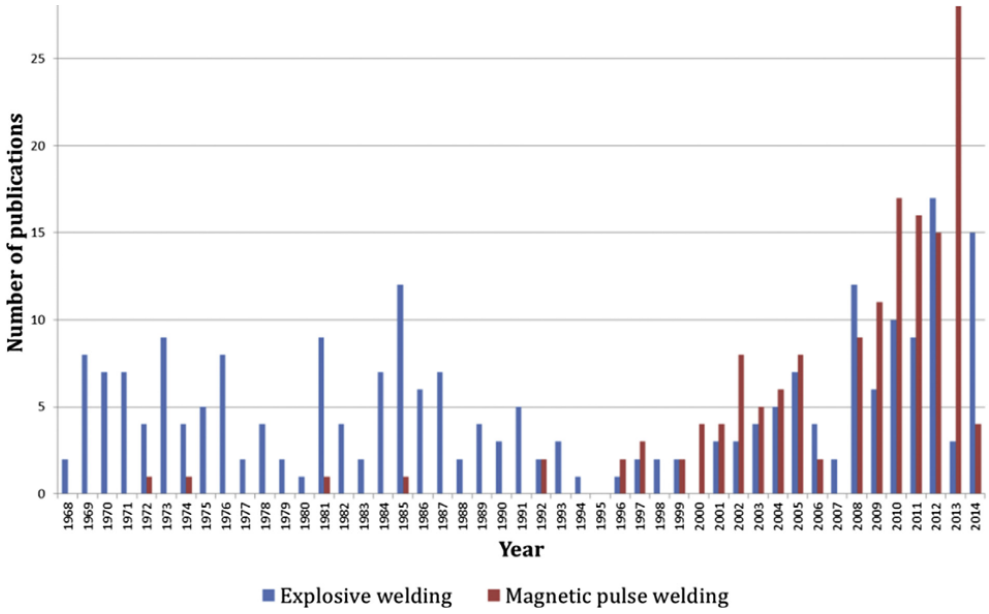

Fig. 2.5 Scientific publications of MPW and EXW since 1968 [33].

Nowadays, MPW is especially attractive for transportation industry owing to its ability to weld light-weight materials that enables a CO2 emissions limitation and thus, a less effect of global warming [33]. A majority of the MPW machines has been developed by PULSAR and DANA companies. Their MPW machines have been used for various development in automotive industry, such as the joining of drive shift made of aluminium/steel joints, automotive aluminium fuel filters, components of air conditioners, automotive earth connector (Fig. 2.6) … [34]. In addition, MPW has recently gained importance and already been successfully used in aerospace industry [35]. For instance, the MPW process has been used to weld aircraft control tubes which can resist torque test (Fig. 2.7). The MPW can also be used to join flexible printed circuit boards [36], high voltage cables, copper tubes on coaxial cables [37].

These components are successfully utilized in electrical industry.

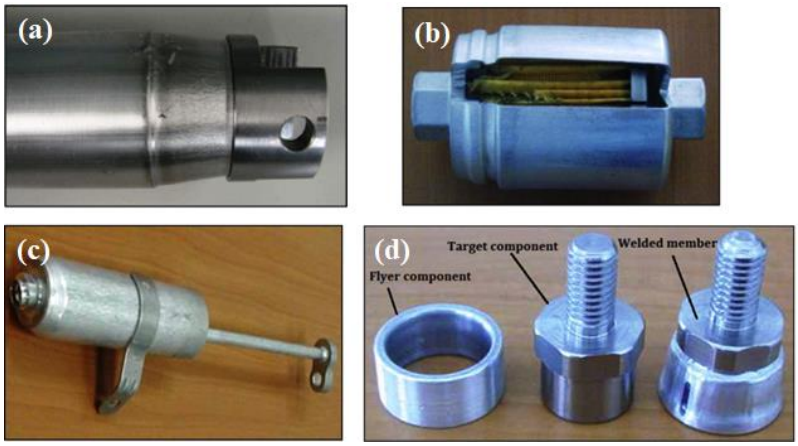

Fig. 2.6 Components of automotive sector obtained with MPW: (a) drive shaft (Al/steel joint), (b) fuel filter (Al/Al joint), (c) automotive A/C receiver-dryer, (d) automotive earth connector [34].

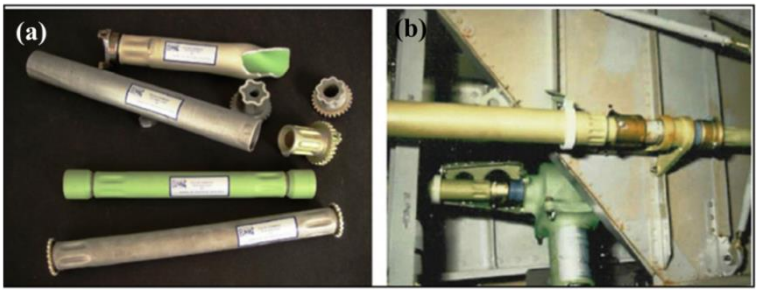

Fig. 2.7 (a) aircraft flight torque tubes [35], (b) aircraft flight control tubes in use [33].

Besides, the application of the MPW configuration also flourishes in processing crimped parts for different applications [20], as shown in Fig. 2.8. Although MPW is mainly highlighted for manufacturing tubular and cylindrical parts, various previous research studies show that it is also well suited to weld sheet metals [29,38–42]. The welding of sheet metals requires a flat coil. Manufacturing company also successfully implemented the MPW for performing various tasks using semi or fully automated process. The company PST products GmbH succeed in implementing such innovation using robotic arms, and portable coil system. This achievement can perform industrial welding of flat sheets to metal bars (Fig. 2.9) [43]. This automated welding can cover a broad range of similar and dissimilar material combinations, e.g. Al/Al[44,45], Al/Cu [46–52]. Al/Ti [53], Al/Steel [53], Al/Ni [54], Ti/Ni [55], Al/Mg [56], carbon

fiber-reinforced plastic /Al [57], Al/metallic glass [58], Cu/Manganin [38], Cu/Steel [59]. With these benefits, the MPW process is always explored and progressively optimized to bring new potential advancements.

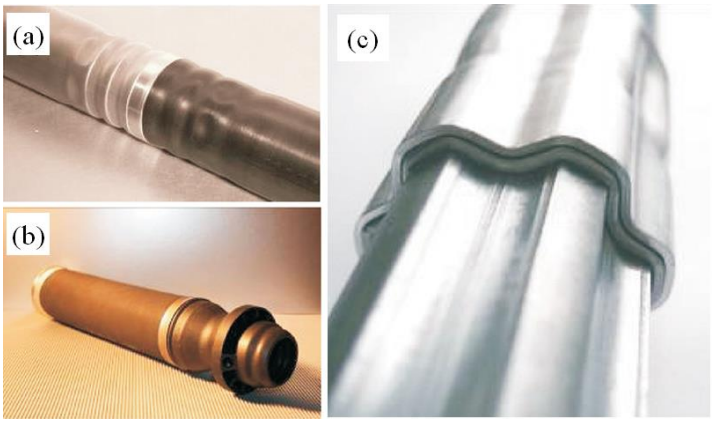

Fig. 2.8 (a) Al/steel crimped tube for instrumental panel beam (b) crimped air suspension, (c) crimped drive shaft [20].

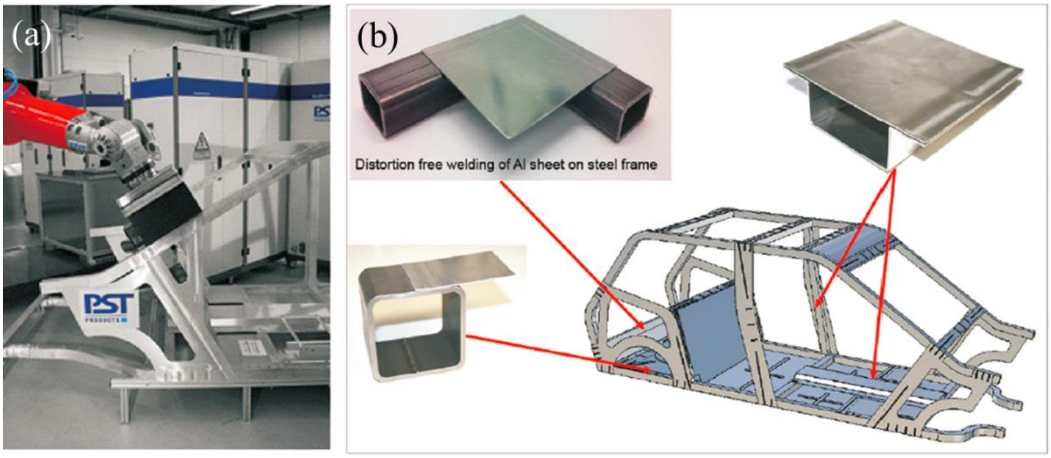

Fig. 2.9 (a) Automated robotic arm used to implement MPW during a Body in White (BIW) construction and (b) various components welded by MPW with the robotic arm developed by "PST products" company [43].

2.2.3 MPW process parameters

Magnetic pulse welding parameters can be broadly classified into three major categories: electromagnetic parameters, geometrical parameters and workpiece parameters. Each category can be further divided into sub-categories as shown in Fig. 2.10.

Name	Major categories	Sub-categories	Unit
MPW parameters	Electromagnetic parameters	Discharge energy	J
		Magnetic pressure	Pa
	Geometrical parameters	Standoff distance	m
		Coil geometry	-
		Fieldshaper	-
	Workpiece parameters	Flyer dynamic behavior	-
		Skin depth	m
		Impact velocity	m/s
		Impact angle	°

Fig. 2.10 MPW working parameters

2.2.3.1 Electromagnetic parameters

The stored energy in the capacitor is rapidly discharged through the coil to produce high collision velocities between the flyer and the target workpiece. Fig. 2.11 shows typical curves of discharge energy. The discharge current curves were recorded using a Rogowski probe during a MPW test. The discharge energy increases with the charging voltage. According to the results in [60], the travelling velocity of the flyer and the collision pressure increase with the discharge energy. This phenomenon will increase the shearing strength between the workpieces and then the wavelength of the wavy interface of the bonded zone.

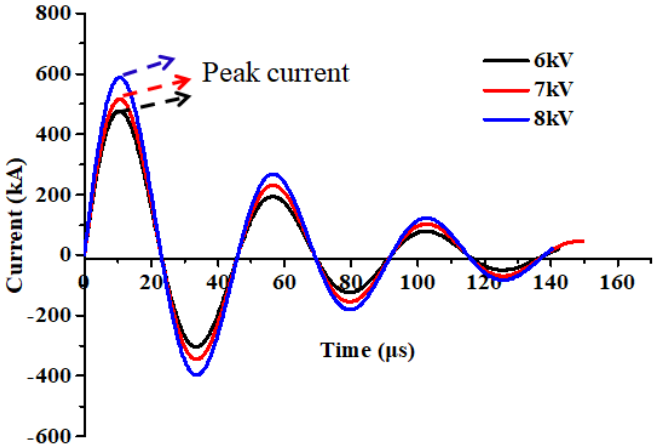

Fig. 2.11 Typical current discharges measured by a Rogowski probe during MPW.

Moreover, the discharge energy is directly proportional to the square of the input voltage (Eq. 2.1). Generally, for each similar or dissimilar material combination, there

is a particular discharge energy range of welding. Therefore, the weld quality can be controlled by adjusting the discharge energy before a welding test. Basically, this can be done by changing the value of the input discharge voltage in accordance with the following rule.

$$\boldsymbol{E = \frac{1}{2} C U^2} \qquad (2.1)$$

Where *E* is the discharge energy (J), *C* is the capacitance of the bank capacitor (F) and *U* is the input discharge voltage (V).

Another electromagnetic parameter is the magnetic pressure that is responsible for driving the flyer plate/tube onto the target piece to form a joint. Generally, a successful bonding requires a high magnetic pressure [32]. During the MPW process, the high magnetic pressure can be achieved with high discharge energy or high frequency current. The magnetic pressure is defined by Eq. (2.2) [61].

$$\mathrm{P} = \frac{\mu_0 K^2 n^2 U^2 C \sin^2\left(\frac{1}{2\pi\sqrt{LC}}t\right) exp\left(-\frac{R}{L}t\right)}{2Ll_w^2} \qquad (2.2)$$

where, μ_0 is the magnetic permeability, k is a coefficient depending on the geometry of the coil, n is the number of coil turn, L and R are the inductance and resistance of the discharge circuit system respectively, l_w is the length of the coil working zone and t is the time.

2.2.3.2 Geometrical parameters

The air gap between the inner surface of the flyer and the outer surface of the target plate, called standoff distance, is shown in Fig. 2.12a [32]. It plays an important role in gaining velocity and kinetic energy that directly affects the weld quality [62]. Previous study [63] revealed that either lower distance or higher distance can decrease the shear strength of the weld (Fig. 2.12b, wherein, sample A and C are cut from edges of the weld zone, sample B is cut from the central zone). Moreover, different material combinations have different optimum standoff distance that depends on the material properties. Fig. 2.12c presents the effects of the standoff distance on the Al/Ti MPW interface [64]. The standoff distance gradually increases from the left

side to the right side. We can clearly see that there is no bonding (left zone of the picture 2.12c) with low standoff distance. Intermetallic and cracks are formed (right zone of the picture 2.12c) with high standoff distance. Excellent bonding (middle zone of the picture 2.12c) is observed within the optimum standoff distance.

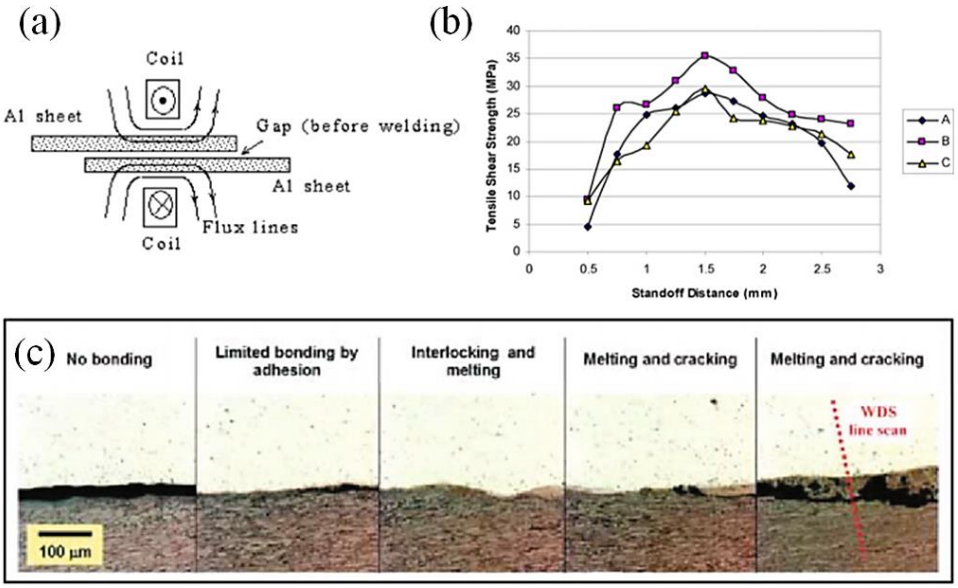

Fig. 2.12 (a) illustration of the standoff distance (air gap) [32], (b) influence of the standoff distance on the tensile shear strength of the weld [63], (c) set of images showing the interface of the Al/Ti MPW welds [64].

Generally, the coils are designed and manufactured considering three aspects: number of turns, shape and material. The coil could be single or multi-turn. Circular and helix coil are used to weld tubular assemblies, and flat coils (such as I-shape, H-shape and E-shape) are used to weld sheet metals. The coils are mostly made of copper-based alloys, such as copper-chromium or copper –beryllium, but aluminium alloys coil can also be used in industrial production.

A field-shaper (FS) is usually used to concentrate the electromagnetic field and consequently improve the electromagnetic forming and welding efficiency. It can increase the magnetic pressure generated on flyer part. The FS manufacturing is mainly considered with the shape design and the material selection. There are various FS geometries depending on the inclination angle [65] or the dimensions (tapered FS, single step FS, and double step FS) [66] of the work zone. Copper alloys or bronze are the most used material to fabricate a FS. A recent new material named “Siclanic”

(Cu-Ni-Si alloy） is proposed due to its good mechanical properties [67]. Moreover, a FS can be imbedded in a single turn coil. However, using a multi turn coil with a FS becomes a promising alternative way to reduce the replacement cost in case of tool damage. MPW process can also be carried out without a FS.

2.2.3.3 Workpiece parameters

The electrical and mechanical properties of the flyer should be considered since they affect the flyer dynamic behaviour during MPW. The most important parameter is the flyer electrical conductivity that influences the eddy currents value on the workpiece. Sufficient flyer electrical conductivity is necessary to generate a high current and consequently a sufficient magnetic field to produce the required magnetic pressure. This is important to meet the requirements for welding. The flyer will be subjected to a very high deformation and the interface also experiences a significantly high strain rate (10^6-10^7 s^{-1}) during MPW. However, the mechanical behaviour of metals changes for strain rates above 10^4 s^{-1}. Therefore, the strain rate dependency must be taken into account. Moreover, the constitutive model should take into account the materials temperature sensitivity since various heating sources (i.e., the plastic deformation, joule effect) may affect the interface temperature. Therefore, Johnson-Cook model is the most commonly used one when we come to MPW modelling and simulation.

Skin depth is the penetration distance that the magnetic field penetrates into the flyer surface zone. It reflects the degree of magnetic flux and the eddy current penetration into the conductor (flyer). The magnetic field and the current density decrease exponentially from the surface of the conductive flyer to the inside. The combination of the eddy current with the magnetic field around the coil generates the Lorentz force that drives the flyer until a collision with the target plate. In other words, the flyer cannot be move without the skin depth effect. The skin depth can be mathematically calculated by the Eq. (2.3) [20]. The discharge current frequency is a crucial process parameter that affects the skin depth for a specific material. Therefore,

the discharge pulse frequency should be selected to generate a skin depth lower than the wall thickness of the flyer in order to obtain an effective collision.

$$\delta = \sqrt{\frac{\rho'}{\pi f \mu_0}} \qquad (2.3)$$

Where δ is the skin depth (m), ρ' is the electrical resistivity of the flyer (Ωm), μ_0 is the magnetic permeability of the flyer (N/A^2) and f is the discharge current frequency (Hz).

During the MPW process, impact velocity and impact angle (Fig 2.13a) are crucial parameters that can determine the interface behaviours [68]. They are influenced by the discharge energy and the air gap. Fig. 2.13b presents the relationship between the discharge energy and the impact velocity. It is clearly shown that impact velocity increases with increasing the discharge energy. Moreover, the time of discharge from the capacitor also affects the impact velocity, as shown in Fig 2.13c. The maximum flyer plate velocity is obtained in the first half cycle discharging time. After that time, the obtained velocity becomes lower. The suitable combination of impact velocity and impact angle is essential for a successful welding. This will be discussed in detail in the section 2.6.

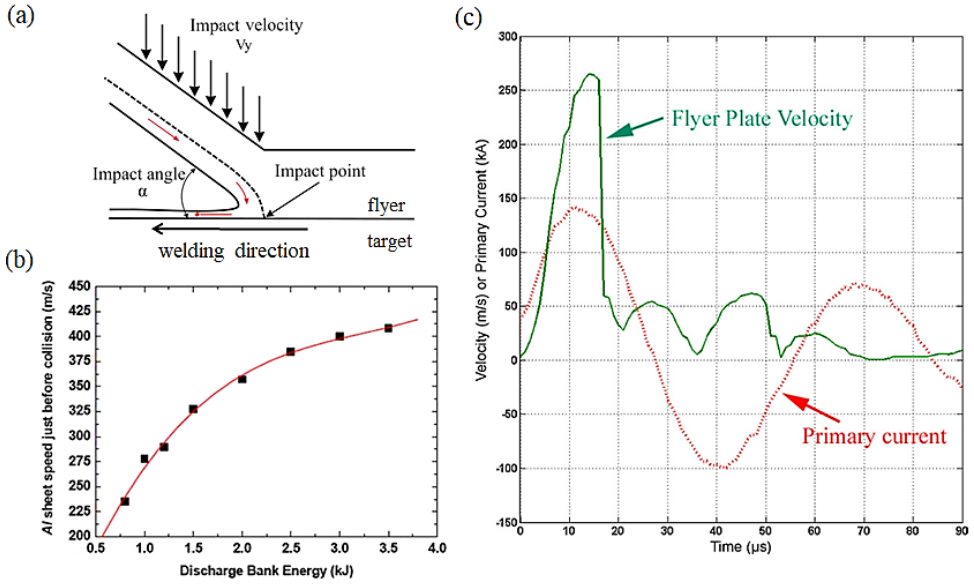

Fig. 2.13 (a) a schematic illustration showing the impact velocity and impact angle [69] (b) relationship between the flyer velocity prior to the collision and the discharge energy [33] (c) effects of the discharge energy on the impact velocity [70].

2.3 Experimental studies on interface dynamic

2.3.1 Interface bonding mechanisms

Investigation and understanding of the bonding mechanisms are important tasks. According to the previously published work, two joining mechanisms have been proposed to explain the MPW bonding, that are solid-state welding and rapid melting followed by rapid solidification.

Previous work stated that the high strain rates and severe plastic deformation are responsible for the solid state bonding. The work in [71] devoted to Al/Al joints, reported that heat source produced by the plastic work due to the extensive shear deformation during welding causes the $\beta'' \rightarrow \beta' \rightarrow \beta$ transformation and dispersoids dissolution near the Al/Al interface. The authors further used this observation to estimate the temperature at the interface zone (IZ) through the precipitate analysis at the fine scale resolution of Transmission Electron Microscopy (TEM). They found that the IZ itself is subjected to a temperature level in between 360°C and 500 °C (lower than the melting temperature of Al) under low impact intensity. The solid-state theory was further extended to dissimilar al/steel joints [72]**.** Conclusions based on numerical model show that the interface temperature is not sufficient to melt neither aluminium nor steel. This finding is also supported by experimental works of Fan *et al.* who found that the Al/Fe interface is composed of a 10 nm amorphous layer formed by atomic interdiffusion [73]. The melting and solidification concept becomes conceivable for MPW.

Recently, some researchers evidenced melting and solidification at welded interface using numerical simulations coupled with experimental observations. Geng *et al.* [74] revealed the bonding mechanism of MPW Al/Fe joint by observation of amorphous structure due to a high cooling rate of about 10^{14}–10^{15} K/s. The authors also identified transition recrystallized zone due to melting and low cooling rate (10^{8} K/s) at the interface. It was concluded that the local melting plays an important role on the phase formation and bonding process in MPW. In the literature, a study

suggests that the formation of intermetallic compounds relies on mass transportation and atoms interdiffusion in solid or liquid state [49]. Moreover, formation of the interfacial microstructural defects such as nanoscale porous structure, voids and microcracks at the MPW joints could also appear due to evidence of interface melting (Fig. 2.14) [75].

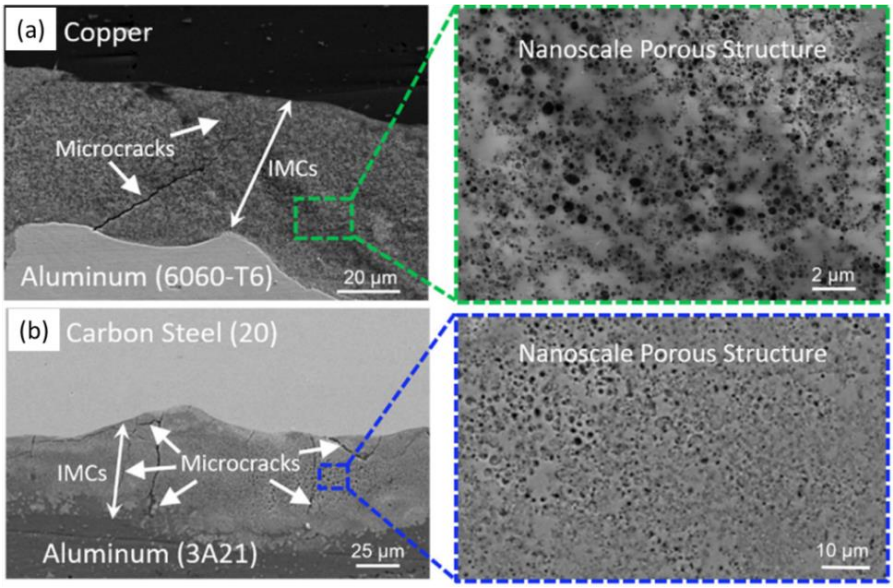

Fig. 2.14 Samples welded by MPW (a) Al/Cu [47], (b) Al/Steel [76].

2.3.2 Interface morphologies

Much effort has been devoted to investigate the interface morphologies in MPW. The interface morphologies are considered to play an important role on the joint strength. It was reported that a characteristic interface feature is the formation of a wavy or rippled pattern [77]. The presence of wavy interface has been observed for both similar [26] and dissimilar [73,78,79] MPW joints (Fig. 2.15). They are generally regarded as an indication of a successful weld in MPW [80,81]. Tubular MPW joints of aluminium alloys with wavy interface without voids show a good and permanent bonding [61]. Hahn *et al.* performed peel tests of MPW joints to show the effects of wavy morphology on the weld quality [82]. Their results showed that the wavy interface pattern can increase the joint strength. The weld with wavy morphology can also present a high fracture resistance [25]. However, other results suggested that the presence of the wavy pattern is not essential to obtain a successful

weld [83,84]. In a recent work performed by Yoon *et al.* [85], a successful weld has been obtained with a flat interface.

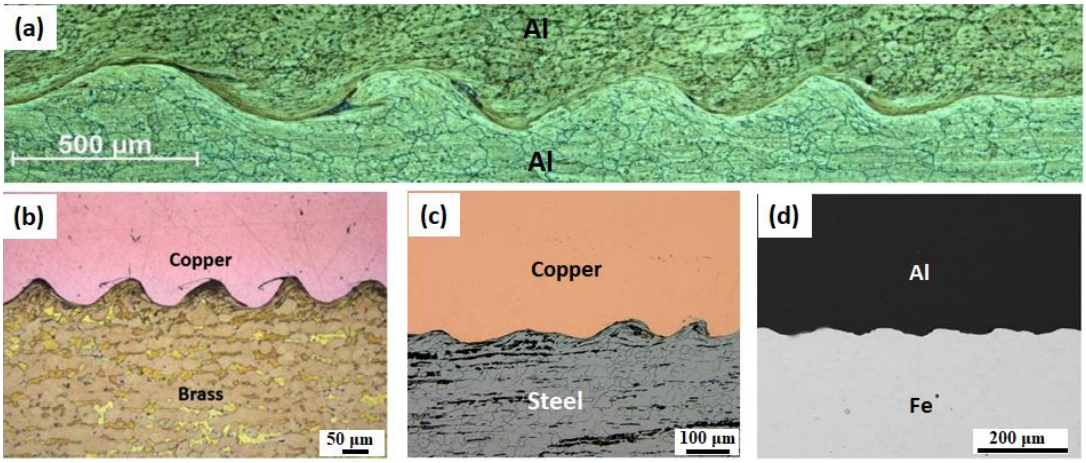

Fig. 2.15 Wavy morphology observed during MPW (a) Al/Al [26], (b) Copper/Brass [78], (c) Copper/steel [79], (d)Al/Fe [73]

Another interface characteristic of MPW joints is the presence of intermediate layers. Yu *et al.* [76,86] carried out MPW of aluminium alloy-steel tubes and found a non-uniform transition zone at the welded interface. They further investigated this transition zone using scanning energy spectrum and found $FeAl_3$ intermetallics. Heterogeneous layer was also shown for some other MPW material combinations, such as Al/Mg [87], Al/Zn [88]. Although many researchers claimed that the formation of intermetallic compounds could be completely avoided during MPW, it was demonstrated by Gobel *et al.* [83] that intermetallic phase formation is inevitable. They reported that the intermetallic compounds are centralized in "melt pockets" within the wavy interface. Considering the straight interface, it was stated that the intermetallic phase films with different thickness are formed at the interface. These findings were also supported by some results of Raoelison *et al.* [47,52]. The authors found that the morphologies of intermetallic compounds in the Al/Cu MPW interface could be wavy shaped or straight. They also discussed the relationship between the intermediate phase formation and the input voltage. A reasonably tiny intermediate layer is produced with low input voltage whereas the growth of intermetallic layer is promoted by higher input voltage. Cracks and different sizes of cavities are generated

at the welded interface when the input voltage is unsuitable. These conclusions were further supported by the work of Yu *et al.* [76] who found that multiple direction microcracks and micro-apertures occur if the input voltage is really high.

Kwee *et al.* conducted MPW experiments on aluminium-copper sheets members and evaluated the influence of process parameters on the interface morphology and weld quality [39]. It was revealed that unsuitable process parameters result in interface melting and formation of intermetallic phase which led to cracking and pore formation at the welded zone that jeopardized the weld quality. Wang *et al.* [58] investigated the interface of Zr-based bulk metallic glass/aluminium plates MPW joint. The interface had a thin interlayer, which consisted of amorphous phase and Al nano-particles, exhibiting features of vortex structure. They concluded that these vortex structures within the interlayer were initially triggered by local metal melting and subsequently driven by stress wave that was caused by high strain rate collision. Recently, Sapanathan *et al.* [44,45,89] found the formation of porous structure at the Al/Al interface during MPW. The porous structures are in the range of few nanometers to a few micrometers. They referred to sequential phenomena of pores nucleation, coalescence and growth within the molten intermediate phase to explain the porous structure formation. This phenomenon was also detected in Al/Cu and Al/Steel interfaces produced by MPW (Fig. 2.14).

2.3.3 Structural analysis

A comprehensive understanding of the structural strength of the weld is necessary since many failures occur in these regions [90]. A lot of work has been done to investigate the structural performance of MPW joints. Pourabbas *et al.* [25] studied the effects of the collision angle and discharge energy on the ultimate load of the welded zone. They found that the joint fabricated with the collision angle of 6° and discharge energy of 7.35 kJ exhibits the highest rupture force. The welded samples manufactured with higher collision angle and/or discharge energy show lower rupture force. Kore *et al.* [91] concluded that the shear strength of Al/Mg MPW

joints is not increasing monotonically with the discharge energy increasing, due to much high discharge energy that could result in severe plastic deformation and easy failure within the weld. The effects of discharge energy on shear strength of MPW joints were also studied by Cui *et al.* [92]**.** In their work, they reported that the AA5182/HC340LA joints could achieve higher shear strength than the parent metal when the discharge energy is carefully selected. Cui *et al.* [62] further extended their work to the effects of standoff distance on the shear strength of same materials combination. The authors claimed that the shear strength of the AA5182/HC340LA joint first increases and then decreases with the increasing of the standoff distance. Hahn *et al.* [82] performed peel test on the lap joints of 5000-series aluminium sheets and 6000-series aluminium hollow profiles. They revealed that the joint strength complied with the strength of weaker materials since failure took place in the flyer sheet. Patra *et al.* [93] conducted torsion tests on copper-steel joints and found that the failure occurred in the copper base metal. In the work of [94], the authors investigated the effects of the wall thickness of the inner tube on the mechanical properties of Al/Fe joints, and proposed a model for the prediction of the critical wall thickness of the inner tube. A linear relationship between the critical thickness of the inner tube and the discharge voltage was observed in their work. They also revealed that the tensile strength of the joint is higher than the base materials properties only when the thickness of the inner tube is higher than the critical wall thickness. Geng *et al.* [95] investigated the dynamic mechanical properties and fracture behaviour of Al-Fe joints using dynamic tensile test. Their finding reported that the maximum shear strength shows positive strain rate sensitivity that deviates the failure from base material zone to the interfacial zone.

The width of MPW interface is usually estimated at several micrometres [23,54]. There are many literatures focus on the micromechanical properties of the welding interface. Watanabe *et al.* [96] investigated the hardness of Cu/Ni MPW joint using nanoindentation technique. They reported that in the near vicinity of the interface, the hardness is significantly increased in the Ni side whereas the hardness is constant in

the Cu side. The authors attributed the increase of the hardness in the Ni side to the hardening effect that results from both solid-solution and grain refinement. Lee *et al.* [23] performed nanoindentation test on the MPW steel/aluminium interface and found that the hardness of the intermediate layer is higher than that of steel and aluminium side. Moreover, the intermediate layers were characterized with the heterogeneous nanohardness distribution. Their TEM results showed that the intermediate layer is composed of fine aluminium grains and intermetallic compound particles. Moreover, there is a thin work-hardened layer around the intermediate. All of these phenomena explained the hardness variation within the intermediate layers. These observations are also supported by the findings of Yu *et al.* [97]. They also stated that the hardness in the interface layer of the MPW steel/aluminium joints is higher than that of the base material. Moreover, they revealed that the hardness of both base metals near the interface layer also significantly increased due to the severe plastic deformation and grain refinement. Stern and Aizenshtein [98] conducted nanoindentation tests to measure the elastic modulus of the interfacial layer that is formed in a MPW Al/Mg joint. The measured values from the interfacial layer are reasonably close to the value calculated from quantum mechanics principle applied on $Mg_{17}Al_{12}$ intermetallic phase (a method to calculate physical properties directly from basic physical quantities based on the principle of quantum mechanics) [99].

Many efforts have also been done to study the influence of the weld geometry on the continuity of the weld. Kwee *et al.* [39] considered the weld length and weld width of magnetic pulse welded lap joint of sheets metals. They reported that the shear strength can significantly increase with the weld length whereas an increase in weld width does not necessarily result in an increase in shear strength. They also claimed that the weld width increases with the capacitor charging energy and air gap whereas the weld length decreases with increasing the air gap. Berlin *et al.* [100] performed MPW experiments on sheets metals using symmetric *H* shaped coils. The authors observed three distinct bond zones in the joint, i.e., one unwelded zone in the centre, two bonded zones and two unwelded zones at the outer zones (Fig. 2.16).

According to the authors, at the centre zone the collision angle is pretty small which cannot form the jetting, hence no bonding occurred. However, in the two bonded zones, collision angle increases and its value is enough to form the jetting that removes surface contaminants and oxides.

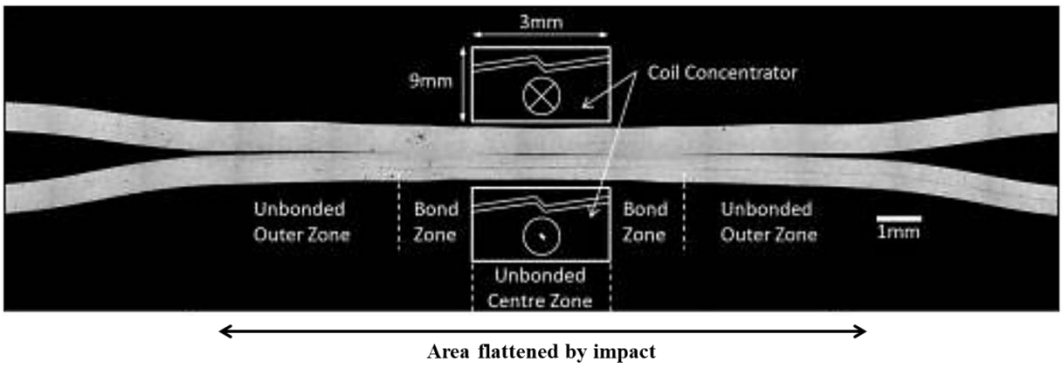

Fig. 2.16 Optical microscope image of cross-sectional area of the MPW weld [100].

2.4 Wave formation mechanism

2.4.1 Wave generation in impact welding

MPW and EXW have the similar interface characteristics. Therefore, many researchers adopt the wave formation of EXW for MPW. This also explains why only a few works attempt to investigate the wave formation in MPW [26,27,101] have been reported. The wave formation mechanisms are classified into the following four categories, i.e., (1) jet indentation mechanism [102–105], (2) shear instability mechanism [26,27,101,106–108] (3) stress reflection mechanism [106,109] and (4) vortex shedding mechanism [110,111].

The jet indentation mechanism describes how the weld interface obtains its characteristic wavy shape by a periodic indentation and hump [104]. According to this theory, the interface creates a re-entrant jet and a salient jet. When the two plates collide, a stagnation point (SP) occurs due to the high interface pressure. Subsequently, the target plate deforms and a hump is formed ahead of the SP. With the hump accumulation, it finally traps the re-entrant jet. The SP moves to the peak of the hump, moves down, goes up to form a new hump and so on. This periodicity

formation “indentation and hump” is assumed to produce the successive waves (Fig. 2.17). Their findings are further supported by the recent simulation work performed by Bataev *et al.* [103]. The authors successfully reproduced the experimental waves using Smooth Particle Hydrodynamics (SPH) method and revealed that the wave formation is due to a relay-race process of successive indentation of protrusions formed on opposite sides of the impacting plates.

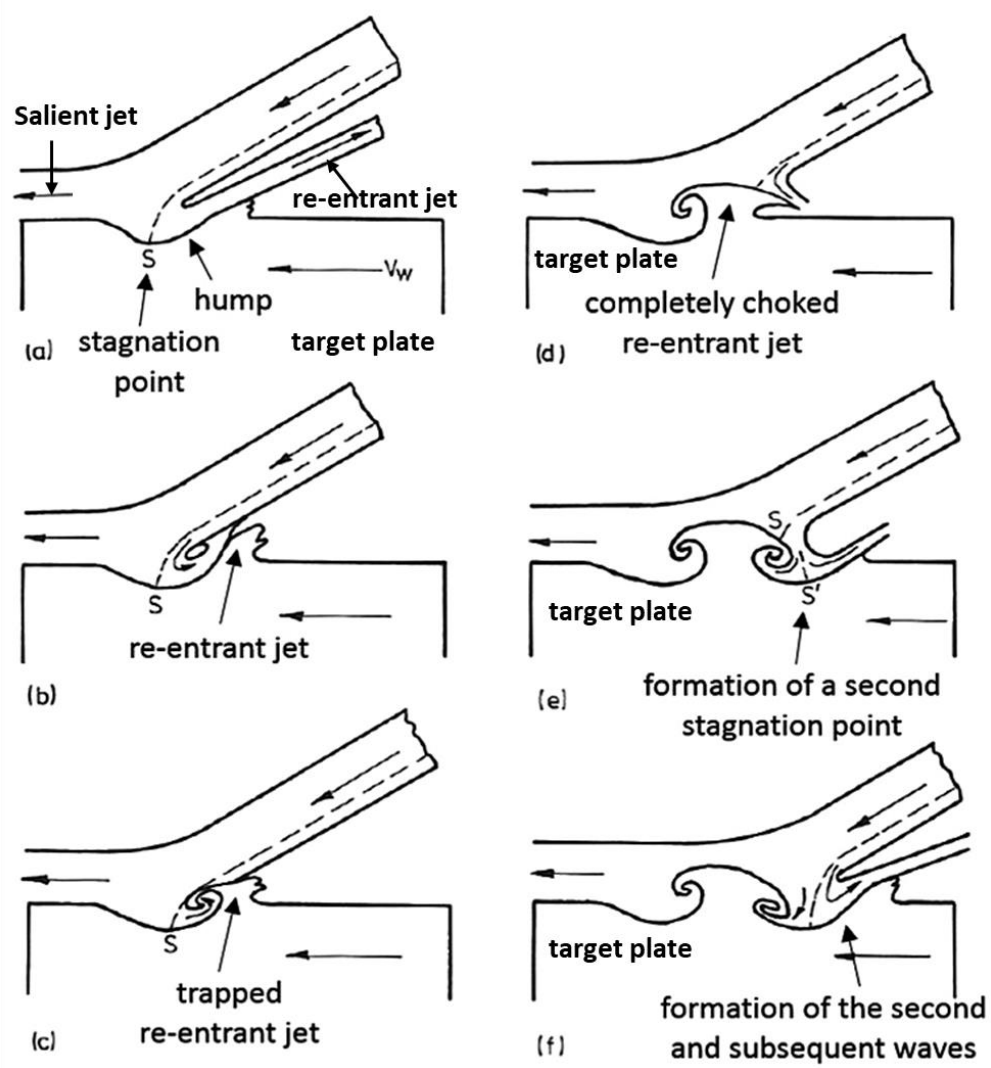

Fig. 2.17 Jet indentation mechanism for wave formation [104]**.**

Another theory was proposed based on the shear instability of the metal flow during the high strain rate collision, better known as Kelvin–Helmholtz (K-H) instability that deals with hydrodynamics. The K-H model predicts that instabilities will occur at the interface when there is an interaction between two different fluids

with different velocities. The interface instabilities involve a mass flow from the material with higher density towards to the material with lower density. As the interface instability happens, it has a certain direction and velocity. This phenomenon can induce the material transfer from one side of the interface to the other side (Fig. 2.18a). To balance the system, material from the side with less concentration gradient will immediately flow, in this way, the interface waves will form, as shown in Fig. 2.18b. The directionality and shape of the newly created interface waves are influenced by the mutual velocity of both flyer and target plates (Fig. 2.18c). In this model, the welded interface metals can be regarded as viscous solids.

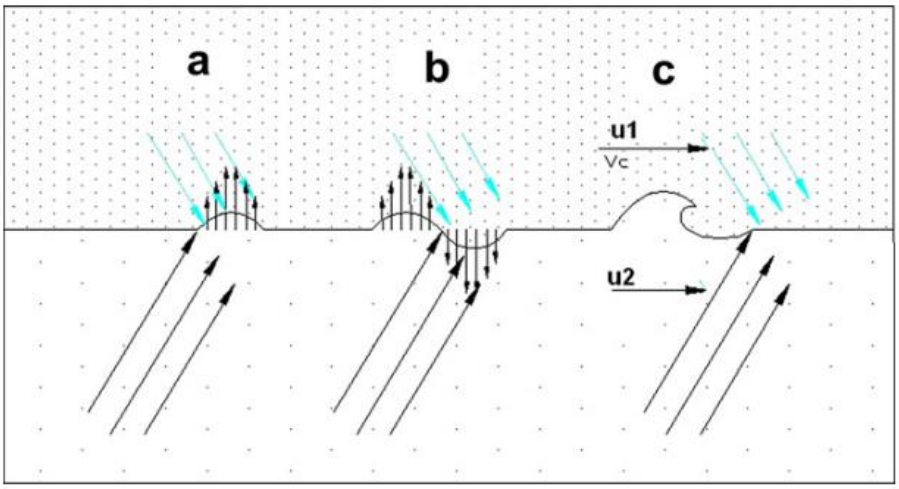

Fig. 2.18 Kelvin-Helmholtz instability along the weld interface (u1 > u2) [106].

The third mechanism (i.e., stress reflection mechanism) attributes the interfacial waves to the successive waves interference from both flyer and target plates. According to Ben-Artzy *et al.* [106], when the flyer collides with the target plates, compression waves will be generated at the impact point and travel through both flyer and target metals (Fig. 2.19a). Then, when the compression waves meet the back surface of the flyer plate/tube, they will be redirected as reflected waves, as marked by blue arrows in Fig. 2.19b. In the experimental work of Ben-Artzy *et al.* [106], the MPW setup is axi-symmetric. Therefore, the compression waves will meet reflected waves at the center of the inner part during a rigid collision [112]. Then it will be reflected and compression waves progress towards to the impact interface (black arrows in Fig. 2.19b). A superposition p-x diagram of (Fig. 2.19 a and b) is given in

(Fig. 2.19 c). Each new impact point will produce new compression waves. The interaction between the newly generated compression waves and reflected waves take place at the impact point and in its vicinity. Moreover, this only happens if the wave periods match. The combination of waves interaction with the extreme pressure and heating at the impact point result in the formation of the interface waves (Fig. 2.19d). Lee *et al.* also observed the occurrence of interface stress waves by simulation [109] (Fig. 2.20).

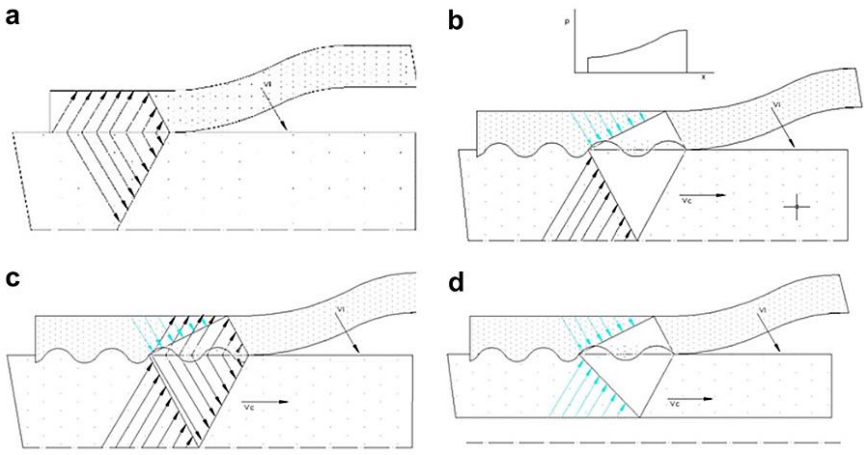

Fig. 2.19 Wave creation model for MPW [106].

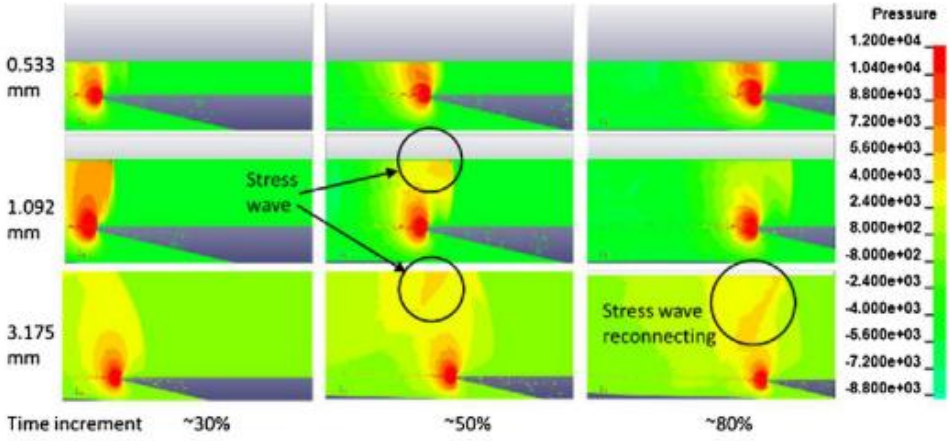

Fig. 2.20 Internal stress waves propagation in target plate with various thickness [109].

Crown *et al.* [111] were probably the first who linked the interfacial waves in EXW and the fluid flow around a barrier, in which regular pattern of eddies is found. After that, this idea was taken up and expanded by many researchers [113,114]. These authors claimed that the waves result from a vortex shedding mechanism. This

mechanism is analogous to the von Kármán vortex street that occurs during a flow past an obstacle (Fig. 2.21). They conjectured that the flow can be regarded as essentially Newtonian at the vicinity of the impact point due to the extreme pressure generated at this area. The interfacial waves occur for a Reynold number beyond a critical value. From their results, the dimension of the "barrier" in the flow is scaled with the jet thickness.

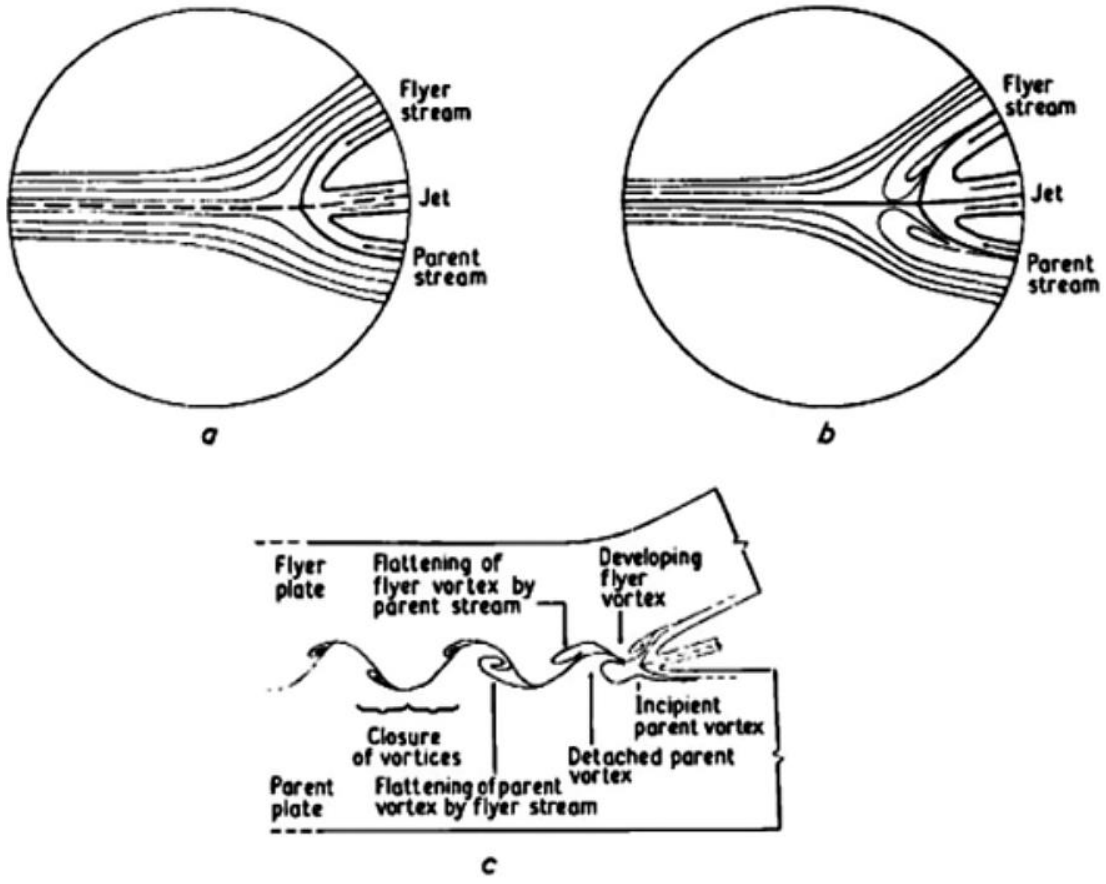

Fig. 2.21 Wave formation with vortex shedding mechanism (a) laminar flow at low Reynolds number (b) vortex formation following flow separation (c) periodic wave formation by vortex shedding [113]**.**

2.4.2 Parameters affecting the wave morphology

Substantial number of studies was devoted to the influencing parameters that affect on the wave morphology (wavelength and amplitude). These parameters range from the collision conditions to the target plate and flyer thickness [60,115].

Wang *et al.* [115] used the numerical simulation to investigate the effects of collision conditions on the waveforms in Ni/SS304 high speed impact welding (HSIW) interface. They claimed that the jet velocity and normal stress at the collision point are the key parameters that affect the wave amplitude at the interface. The flyer horizontal welding velocity is the main factor that influences the wavelength. They concluded that wavelength increases while decreasing the flyer horizontal welding velocity and the wave amplitude increases with the jetting velocity. However, contradictory conclusion was drown by Watanabe *et al.* [60]. The authors combined analytical formula with experimental work and found that the wavelength increases with the collision velocity. Zhang *et al.* suggested that the impact velocity should dictate the wave amplitude [70]. This finding was supported by the findings of Vivek *et al.* [116]. Their investigations showed that the wave amplitude is largely influenced by the impact velocity. Elsen *et al.* [117] confirmed this effect by numerical simulation of a MPW tube process. The wave amplitude increased with the impact velocity. Crown *et al.* [111] claimed that the wave amplitude is highly dependent on the collision angle whereas its dependency on the collision velocity is almost negligible.

In the study reported by Ben-Artzy *et al.* [106], the interface wavelength is influenced by the geometry of the inner part. Fig. 2.22 presents the evolution of the interface wavelength with the wall thickness (half of free propagation path of shock waves). The interface wavelength increases with the wall thickness regardless of the pulse energy level (8, 9 or 10 kJ). The results of Lee *et al.* [109] show that increasing the thickness of target part increases the interfacial wavelength. Chizari *et al.* [118] revealed that the wave shape and amplitude are influenced by the shape of the flyer plate. Wave interface with highest amplitude is produced using flat flyer plate whereas the U-shaped flyer produces wave interface with lowest amplitude. Lee *et al.* [119] studied the effect of flyer thickness on the interface wave morphologies during impact welding using experimental methods and numerical simulations. It was found that the interfacial wavelength increase with the flyer thickness.

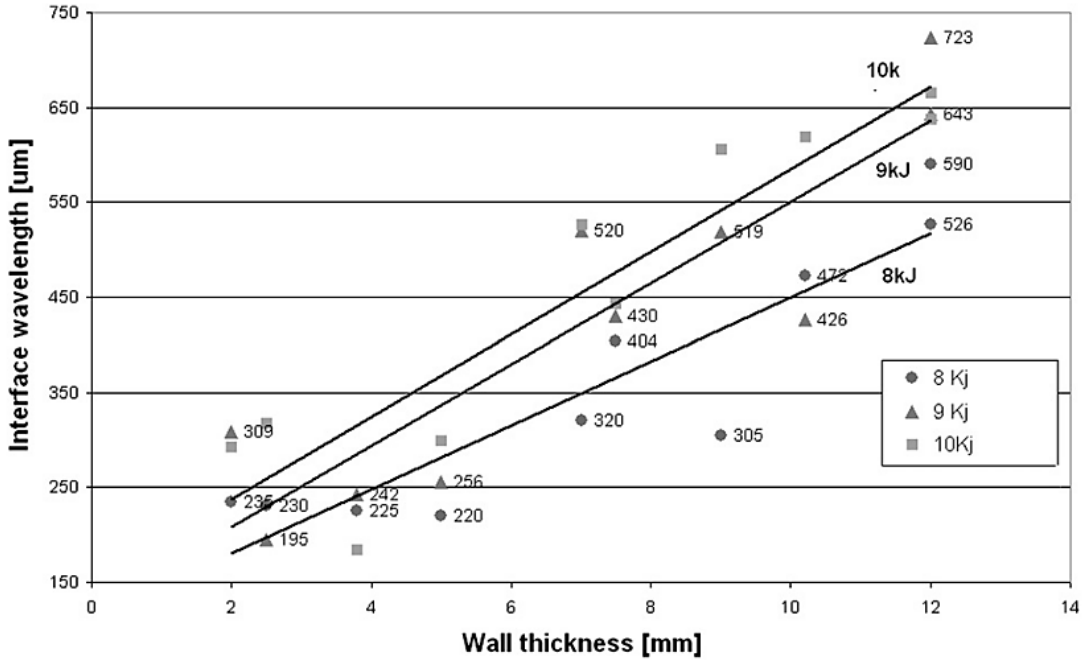

Fig.2.22 The relationship between wavelength and wall thickness in MPW [106].

2.5 Simulation investigation of the interface dynamic

2.5.1 Simulation of the welding interfacial morphologies

During HSIW, the interface zones experience severe plastic deformation producing complex and heterogeneous interfaces that involve a complex kinematics and thermomechanical kinetics. These phenomena are difficult to characterize by in situ experimental methods. However, the successful welding of material combinations needs an adequate depiction including the complex interface behaviour during the dynamic and transient process conditions. Recently, with computational modelling techniques progress, physical realistic simulation provides some understanding of the interface behaviour produced during HSIW.

Nassiri *et al.* [120,121] used the Arbitary Lagrangian-Eulerian (ALE) simulation solver available in ABAQUS software packages to simulate HSIW process of Al6061-T6 plates. The authors successfully captured the interface wavy patterns using fine mesh with a size of 5μm at the interface. They presented a qualitative comparison between spatial periodicity of disturbance functions and the physical wavelengths.

The accuracy of their model was further validated with the experimental observations. The simulation results showed good agreement with the experimental observations, in terms of temperature prediction and interfacial melting (Fig. 2.23). Sapanathan *et al.* [26] also used the ALE method to investigate the MPW interface characteristic changes. They claimed that ALE cannot successfully reproduce the interfacial morphological transition toward a wavy interface, the successive jetting formation, due to excessive interfacial shearing (Fig. 2.24).

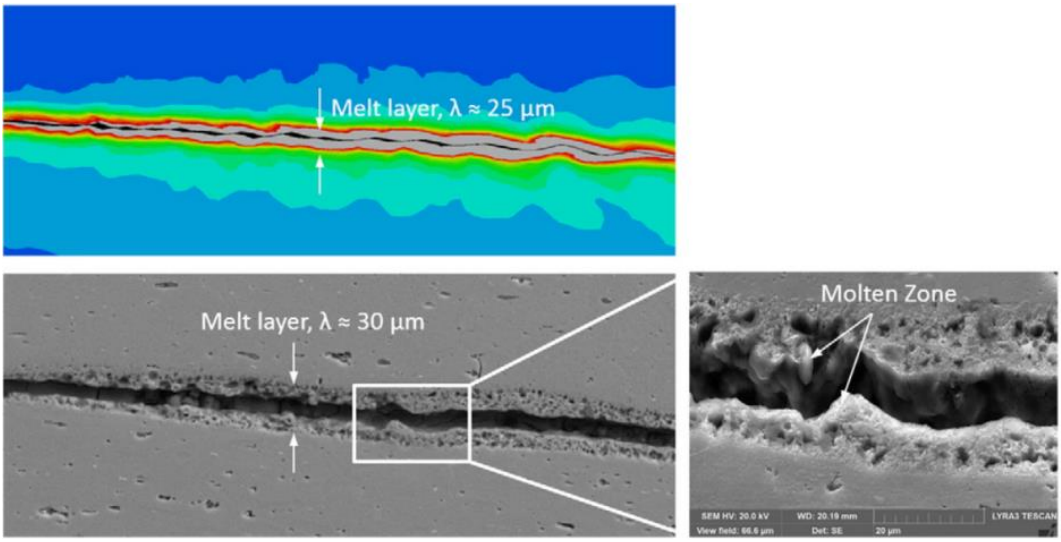

Fig.2.23 Comparison of molten layer between an ALE model and an experimental result [120].

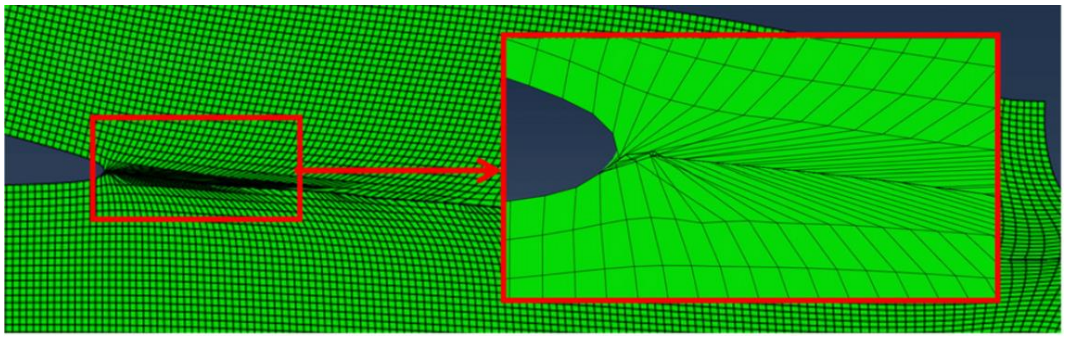

Fig.2.24 ALE limitations because of excessive interfacial shearing [26].

In the literature Eulerian simulation methods is found to be a good alternative to overcome the limitations of the ALE method [26]. It is well known that Eulerian method can well reproduce the experimentally observed wavy interface, in terms of shape, plastic deformation and shear strain orientation (Fig. 2.25). Moreover, the thermomechanical analysis of the interface obtained from Eulerian methods was

further used to explain the formation of experimental defects (Fig. 2.26). The Eulerian method is deemed to be capable of predicting the high speed collision interface behaviours [27]. Formation of regular wave, wake and vortex in Al/Al MPW interface are captured (Fig. 2.27). The wave formation is due to the successive upward and downward jetting. Moreover, the complex interfacial morphologies, including wake and vortex, result from the increasing of shearing instabilities. The experimentally observed deposited particles outside the welded region were attributed to material ejection. Zhang *et al.* [122] used the Eulerian computation with LS-Dyna to investigate the interfacial morphology of Cu/Ti impact welds. A weak vortex was found in their work. Sun and Xu [123] reproduced a weak interfacial morphology on MPW dissimilar material combinations, i.e., Al6061-T6 and AISI 1045, through Eulerian simulation.

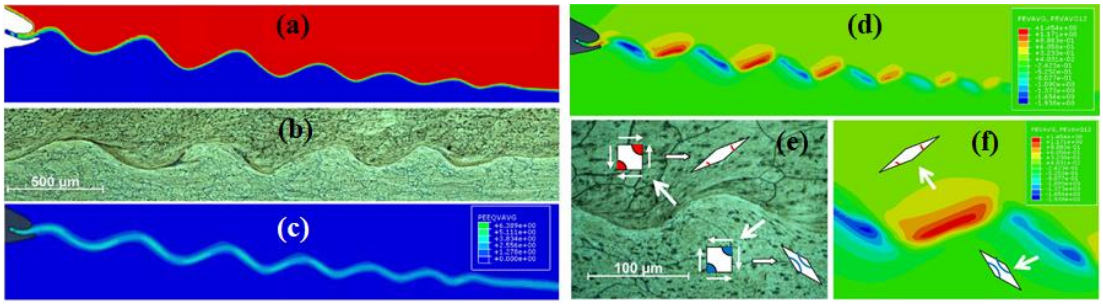

Fig. 2.25 Comparison the experimental results and the predictions from Eulerian approach results (a-b) simulation interface kinematics and wave formation (c) computation of plastic strain (d-f) interfacial shearing [26].

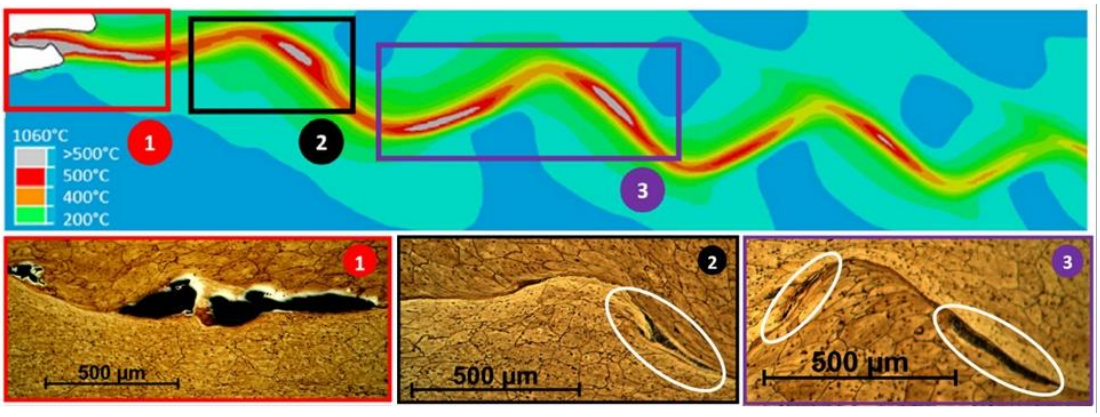

Fig. 2.26 Numerical and experimental results for defective zones due to significant interfacial heating confinement [26]**.**

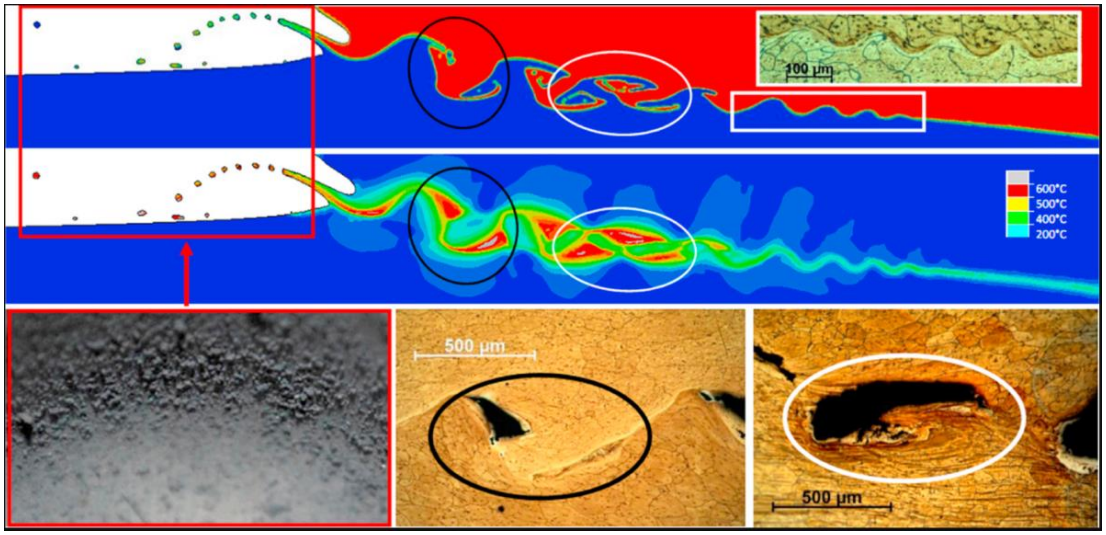

Fig. 2.27 Eulerian simulated interface behaviours during MPW [27].

In the publications of the HSIW, two meshless methods, i.e., the molecular dynamic (MD) [124–127] and SPH [13,74,103,128] have also been used to simulate interfacial collision behaviours. Kiselev *et al.* [124,125] stated that MD method can reproduce the phenomena of interface behaviours including jetting, ejection, wave and vortex formation. At the same time, the authors also pointed out that the sizes of the geometrical model using MD method are 4–5 orders smaller than the real size of plates used in the HSIW experiments. This restricts the capability of MD. Bataev *et al.* [103] simulated the interface behaviours of HSIW similar steel combinations using SPH method. The results showed that SPH method can accurately reproduce the jetting phenomenon, the formation of the wave boundary and also the vortex zones (Fig. 2.28). They concluded that the formation of vortex is associated with the squeezed movement of the flows. In the work performed by Geng *et al.* [74], the wave morphology and the local melt in Al/Fe MPW interface are well reproduced using SPH methods.

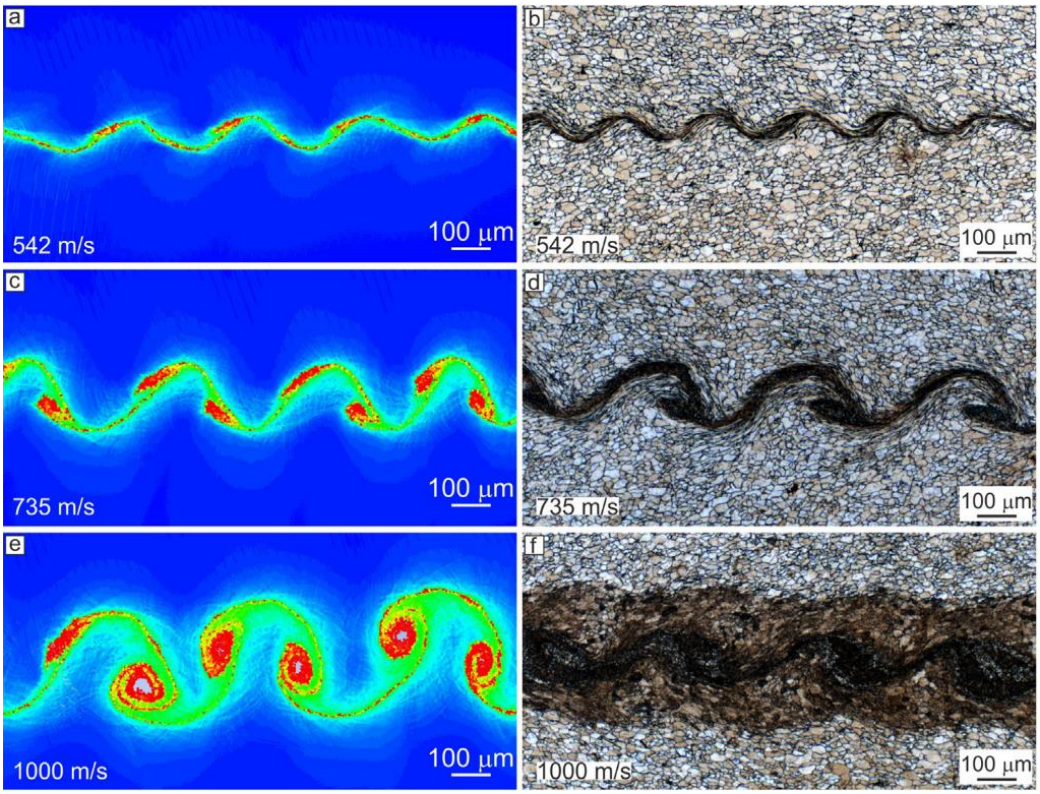

Fig. 2.28 Comparison of experimental results with SPH simulation [103].

2.5.2 Simulation of the welding interfacial parameters

Little literature has been dedicated to the interfacial state including structural changes, metallurgical transformations and whether a weld is successful or with an adverse situation. Sapanathan *et al.* [44,89] predicted the interface temperature and pressure history to identify the development of various sized pores (sub-micron size to few micron) in Al/Al MPW interface. It was found that the interface experienced ultra-high heating and cooling rates that provides the favourable condition for pore nucleation and solidification. Moreover, the increase and decrease of the interface pressure result in vaporization and depressurization phenomena that promote the nucleation, growth and expansion of the pores. Chen *et al.* [129] claimed that this ultra-fast heating and cooling rate during the high pressure impact process can induce a melting and a subsequent recrystallization which are evidenced by their experimental observations, i.e., the occurrence of significant grain refinement in the vicinity of the aluminium/magnesium interface. Lee *et al.* [130] analysed several interfacial parameters including local temperature, pressure, and strain distributions.

The authors correlated those parameters to interface microstructure development and studied the mechanisms of multiple features, including deformation twinning, adiabatic shear banding and dynamic recrystallization, observed in the copper/copper welded interface. The dynamic recrystallization was also found at EXW titanium/steel interface in the work conducted by Chu *et al.* [131]. The authors performed SPH simulations and reported the deformation-recovery-recrystallization at the interface that results from the rapid temperature increase combined with high cooling rates. Moreover, the melted zone at the interface is mainly due to trapped jet.

Mousavi *et al.* [132,133] extracted several interfacial parameters, i.e., contact pressure, normal stress, shear stress and strain, effective stress and strain, strain-rate, impact velocity-dynamic angle and temperature history, from simulation results. The authors used those parameters to identify some bonding criteria, for example, jetting phenomenon, critical effective plastic strain and shear stress, interfacial wave formation, and collision velocities depending on the collision angle. The authors also compared the simulation results with experimental observations and suggested some other bonding criteria using a critical value of pressure and velocity, both relying on the effective strain at the onset of bonding. Uhlmann *et al.* [134] used simulation method to investigate MPW sheet process and concluded that both calculated pressure and plastic work can be used as welding criterion. Some publications [132,133,135,136] pointed out that the interface can form a successful bonding when the following two conditions are met (1) the interface experiences opposite shear stresses, and (2) the shear stress should exceed a threshold value. Moreover, it was stated that the same shearing orientation prevents the interface bonding. The simulation results of Chen *et al.* [11] have shown that the metal jet during a collision of Al on high strength duplex stainless steel came from the aluminium side. The jet velocity was in the range of 4000-5000 m/s and the maximum temperature can reach 1727 °C - 2227 °C. They also concluded that the use of a stainless-steel interlayer at the interface can lower the interface plastic strain and temperature that may improve the weld quality.

2.6 Weldability window

2.6.1 Concept of weldability window

Weldability window is one of the most important topics since it can guide the practical industry production [137–139]. The weldability window is defined by the welding parameters, such as input discharge voltage, air gap, impact angle and impact velocity, collision angle-collision velocity and it consists of an area bounded by several situations. The weldability window denotes the presence or absence of a good weld for a given set of input parameters instead of quantifying the strength of the weld. The weldability window is different for various process parameters combinations and for each pair of metals. Fig. 2.29 shows a generic weldability window [140]. The shaded area in Fig.2.29 represents a region containing the optimal impact conditions that produce a wavy interface without melting. One may try to determine a weldability window using experimental tests and numerical simulations as we will discuss in sections 2.6.2 and 2.6.3.

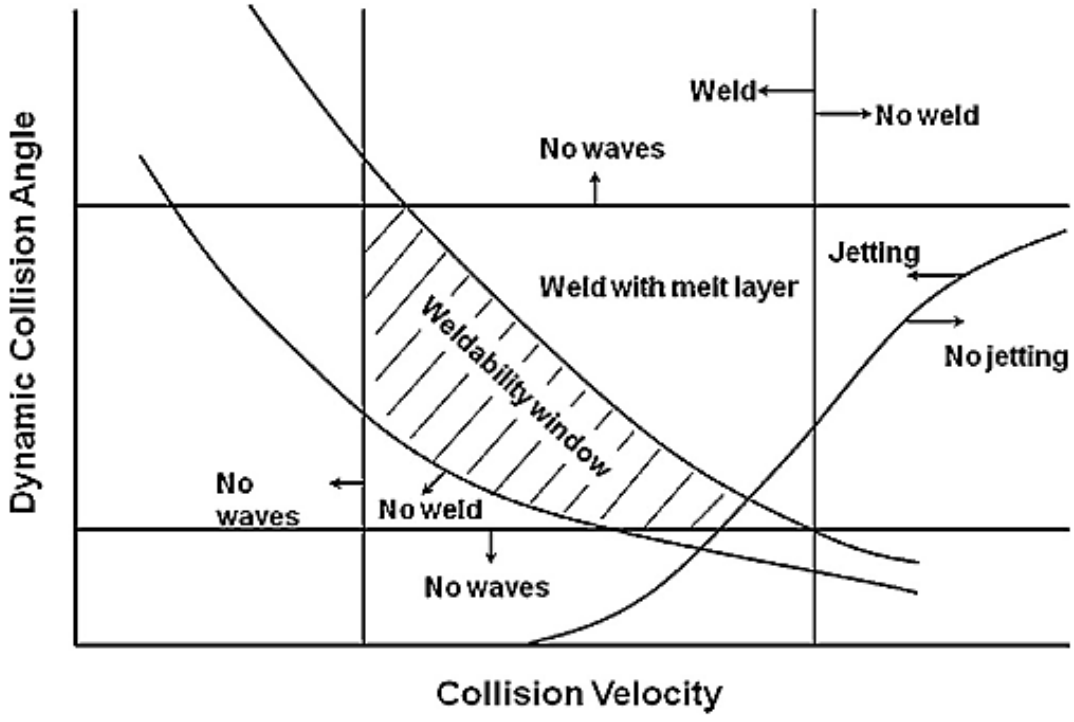

Fig. 2.29 Generic weldability window in HSIW [140].

2.6.2 Weldability window study based on experimental procedures

A developed weldability window is presented in Fig. 2.30 [141]. The window determines appropriate values of input charging voltage and air gap for obtaining a successful joint in case of MPW of AA6060T6 tubular assembly. The authors found that the welding is unsuccessful below the lower boundary of standoff distance whereas defective welds are produced above the higher boundary of standoff distance. Based on this weldability window, they concluded that intermediate gaps are suitable for achieving successful welding with potential permanent weld. Raoelison *et al.* [61] also developed another two windows for MPW assembly of AA6060T6 in terms of charge voltage (U) - air gap (g) diagram determined by a quantitative analysis of the welds (Fig. 2.31a) and a qualitative analysis of the welding velocity (Fig. 2.31b). They regarded the set (U-g) pair which induced the beginning of defective welds as the upper limit of the window. The U-g value creating the straight wavy interface was regarded as the lower boundary of the window. They concluded that both weld variance in U-g diagrams has a convex shape. A weldability window for MPW of AA6060T6/Cu assembly defined by U-g was also developed [137]. The authors found that welding range of good weld for the case of similar AA6060T6 assembly is wider than that for the case of AA6060T6/Cu assembly. Same welding parameters, i.e., U and g, were also used to develop the weldability windows for MPW of aluminium/steel sheet combination [86]. It was found that a lower limit and possible upper limit for discharge voltage were always observed in the weldability window regardless the width of the joining zone (Fig. 2.32). It can be seen that the range of the weldability window decreases with the increase of the width of the joining zone. The authors also pointed out that when the width of the joining zone is lower than 5 mm, it is difficult to meet the required collision angle to generate a metallurgical joint.

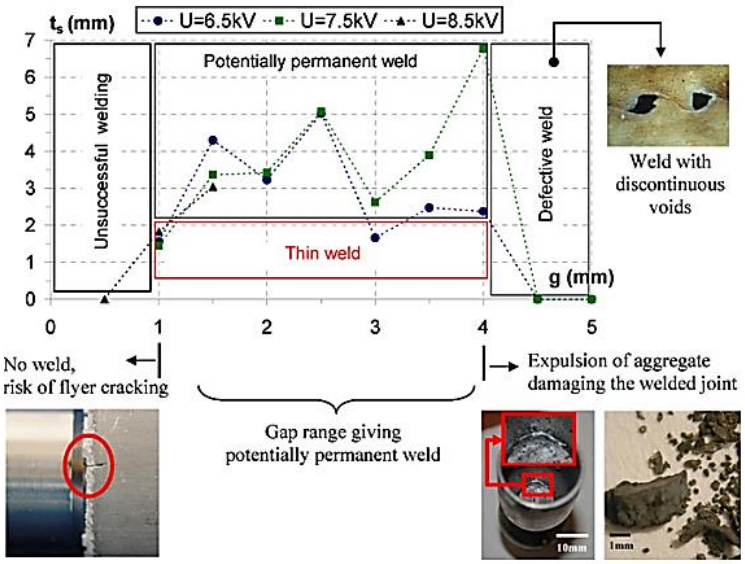

Fig. 2.30. Welding conditions and observed welded joints kinds [141].

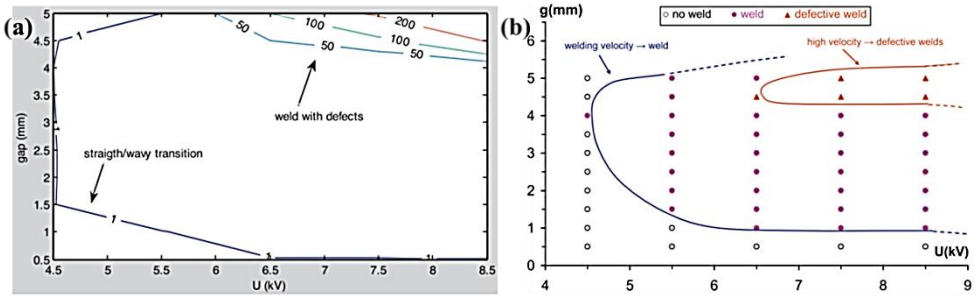

Fig. 2.31. Explanation of the weldability window: (a) quantitative result and (b) qualitative determination defined by the velocity isovalues [137].

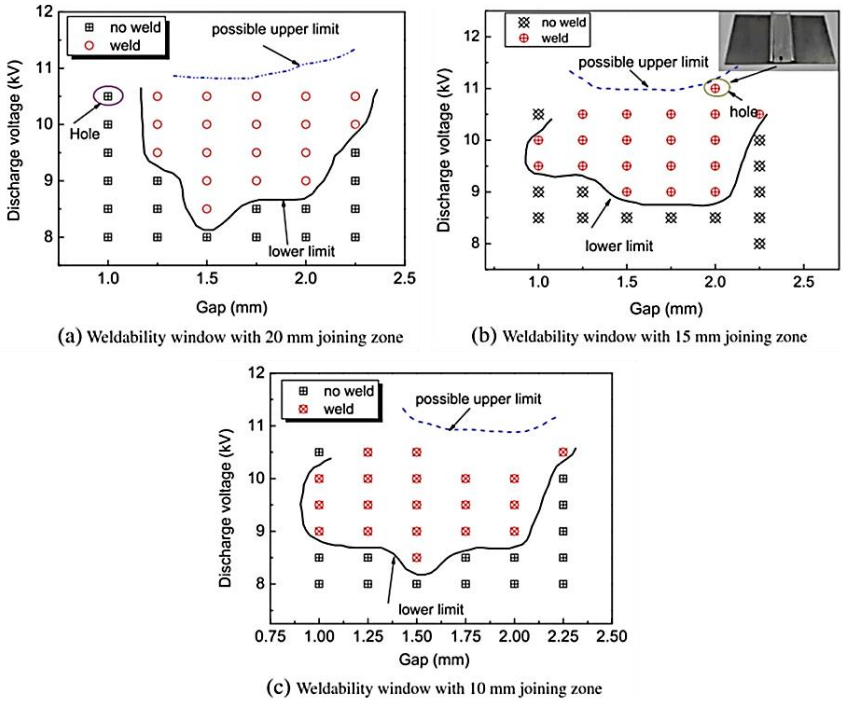

Fig. 2.32. Weldability window cited in [86].

Zhang *et al.* [142] built a weldability window for magnetic pulse welding of 0.254 mm thick Cu110 plate-to-plate, as shown in Fig. 2.33. They first performed several experiments and measured the impact velocities by Photon Doppler velocimetry (PDV). Subsequently, a mathematic model was developed to calculate the corresponding impact angle. They used the values of impact velocities and impact angles obtained from all experimentally successful weld cases, to build a window. The results show that successful welds are obtained with impact velocity and impact angle in the range of 200-350 m/s and 2° to 7°, respectively. The authors concluded that effective welding requires proper combination of impact velocity and impact angle. Oliver *et al.* [143] developed a weldability window for MPW of aluminium/copper tubular parts from results of the compression tests. The indication of the welding range is given in Fig.2.34, based on the values of discharge energy, gap and overlap distance. The conditions for successful experimental welds are located between two surfaces. The authors claimed that the combination of various gap and overlap distances can produce successful welds, if the selected energy generates an appropriate impact velocity.

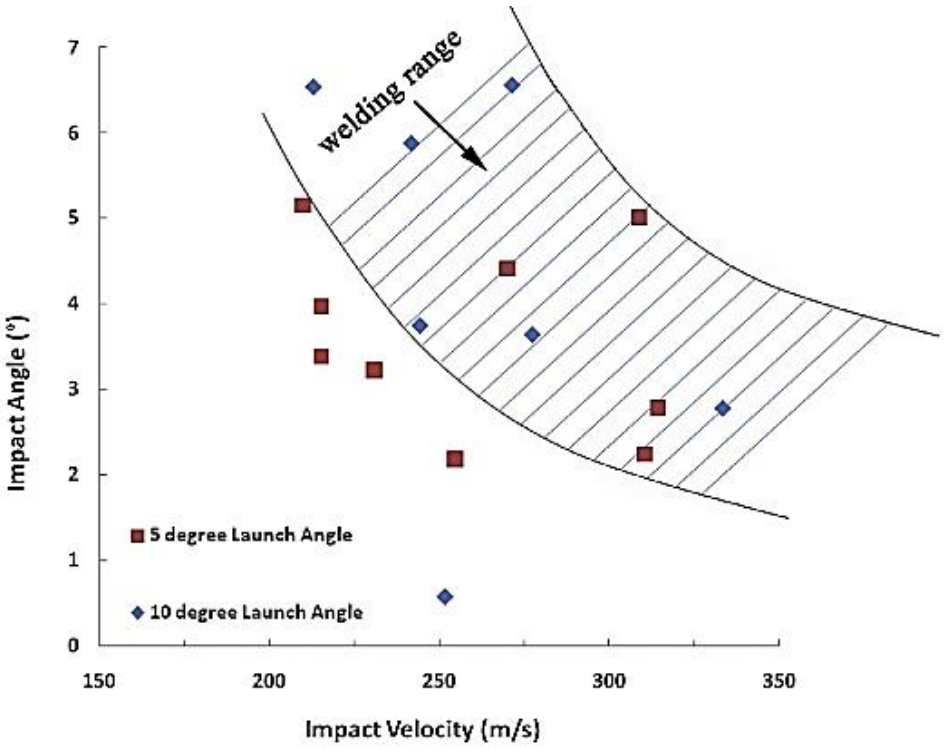

Fig. 2.33. Weldability window for MPW Cu110 joints [142].

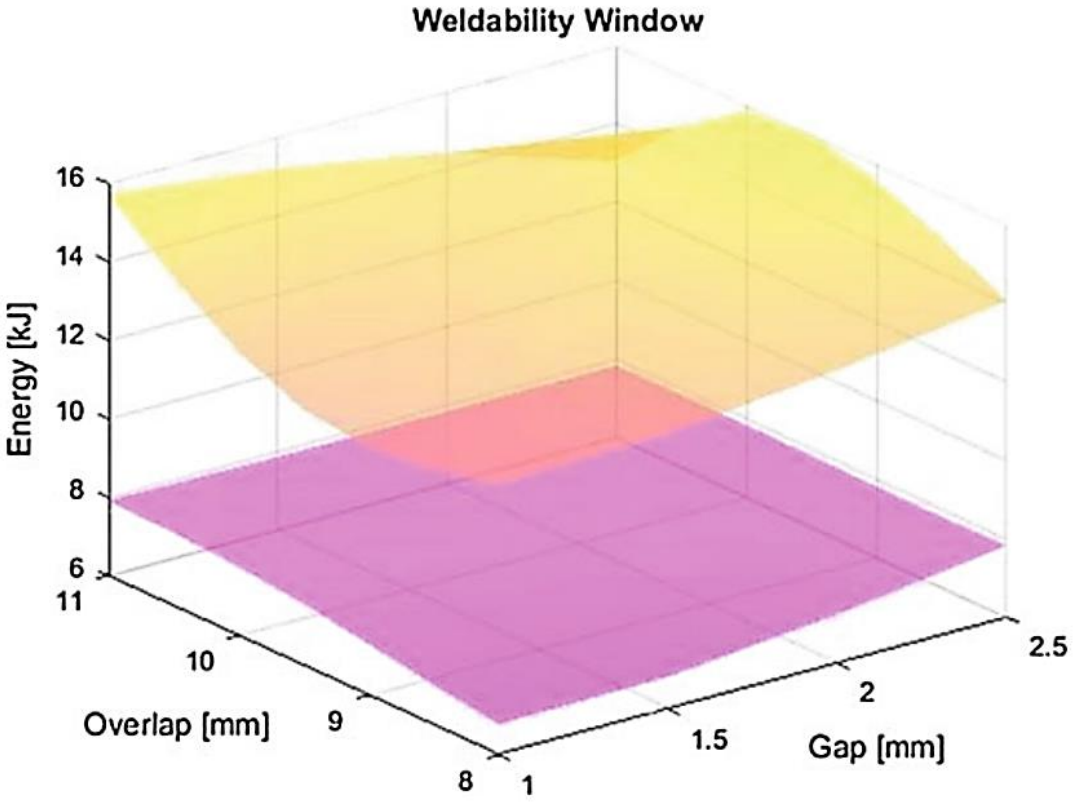

Fig. 2.34. Illustration of the weldability window with selected parameters [143].

2.6.3 Weldability window study based on numerical simulations

Compared to experimental method, numerical simulation provides an alternative approach to build a weldability window without large experiments. However, very limited researches were carried out on this topic. Psyk *et al.* [144] proposed a numerical model to build a weldability window for MPW of Cu-HDP and EN AW-1050. In their work, they first compared the experimental final shape with the one from numerical simulation. Subsequently, the authors correlated the local collision parameters to the positions of the welded zones, and finally provided process windows based a quantitative collision parameter, as presented in Fig. 2.35. The authors found that in case of copper flyers, the window indicated that higher impact angles necessitate higher velocities, whereas impact velocities of more than 450 m/s are hardly achievable for copper flyers because of its relatively high mechanical characteristics. Thus, the suitable impact angles are in between 5°-20° for this process. Regarding the case of aluminium flyers, higher velocities up to 650 m/s can

be obtained and angles up to 40° are possible. Nassiri *et al.* [145] performed ALE simulation method to predict a weldability window of Al6061-T6/Al6061-T6. The authors captured wavy patterns as a first estimation of parameters necessary to achieve a successful weld. After that, they linked the wavy morphology to the process parameters to build a window which can reduce trial and error experimental investigations. They developed a wavy pattern window based on the impact velocity and impact angle (Fig. 2.36a). The lower and upper limits for the impact velocity are 300 m/s and 500m/s, respectively. The authors also developed a wavy pattern window based on the collision velocity (Fig. 2.36b). The collision velocity is the key process parameters that determine the wavy pattern. The window was separated by four lines, in which line b-b at 1000 m/s represents the transitions from a straight to a wavy interface and line c-c shows the maximum collision velocity (~3500 m/s). Moreover, the lines d-d and e-e (upper angular value investigated) give the upper and lower limits for the impact angle. The curves f-f and g-g show the lower and the upper limits of collision velocities with respect to the impact angle. The authors claimed that above the curve g-g the temperature of the interface exceeds the melting point of the material.

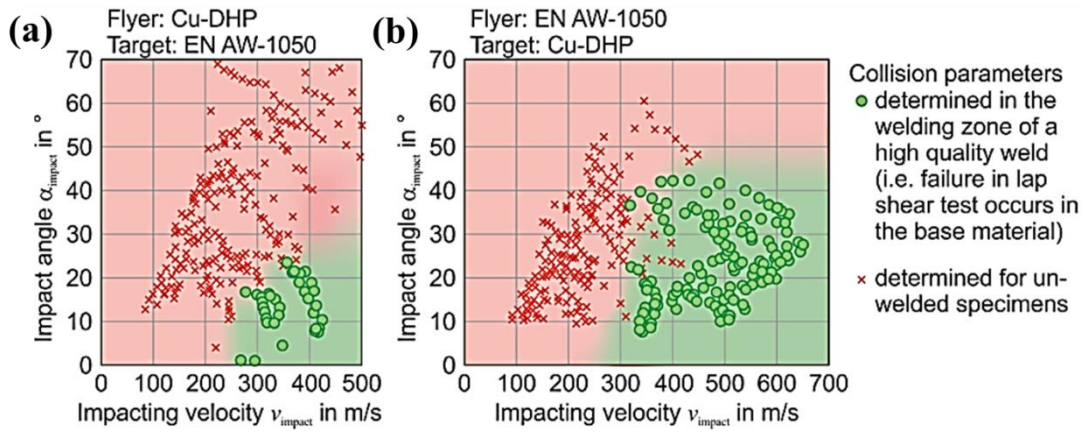

Fig. 2.35 Process window for welding (a) Cu-DHP flyers onto EN AW-1050 targets and (b) EN AW-1050 flyers onto Cu-DHP targets [144].

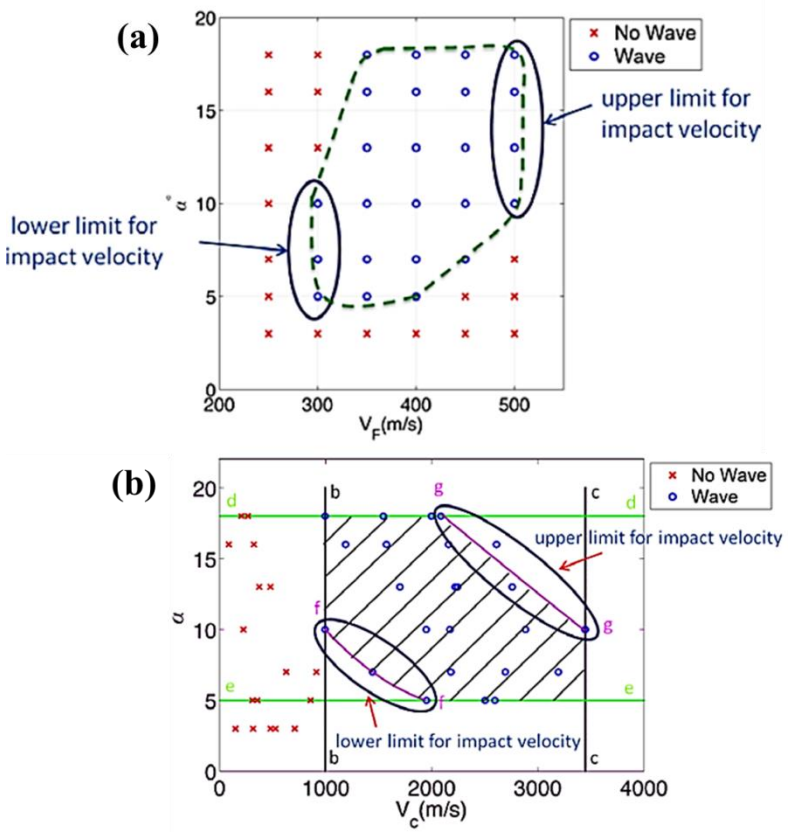

Fig. 2.36 Wavy pattern window for AL 6061-T6 with respect to (a) impact velocity and (b) collision velocity [145].

2.7 Conclusions

Based on this extensive literature review, the current research progress can be concluded simultaneously concerning the MPW process, wave formation mechanisms and interface dynamic phenomena.

MPW process is an environmental friendly and has the capability to weld dissimilar metals. It is clear that multiple parameters influence the impact-welded interface during this process. However, these parameters are linked to the impact angle and the impact velocity that deeply affect the weld interface morphologies. The impact angle and impact velocity are considered to determine the weld characteristics and properties. Therefore, it is necessary to measure the velocity and the angle along the interface and to correlate them with the interface structures.

In the literature, various mechanisms have been proposed to explain the formation of the wave interface that is considered as a precondition of good welding.

However, the wave interface formation has been the subject of many debates. Moreover, disagreements still subsist about the parameters than can influence the interface wavelength and wave amplitudes. Last but not least, there was no systematically investigation of the physical phenomena and kinematics of various types waves including irregular waves.

While it is foreseeable that the interface involves multi-physics and complex interface dynamic phenomena due to the extremely high strain rate and the transient MPW process. The work towards understanding and prediction of the interface dynamic phenomena increased a lot during the past few years and reported interesting results. There are different mechanisms of interface formation. Numerical simulations show complex interface morphologies, heat generation, plasticity, and phase formation during MPW process. However, we have seen in the literature that a great work is still needed to reach a unique comprehensive qualitative and quantitative theory able to explain and to predict the complex interface behaviours during MPW.

For all of the above mentioned reasons, this research attempted to investigate the complex interface dynamic phenomena for MPW Al/Cu combinations. It focused on interface mechanisms under the high strain rate collision and thermomechanical kinematics.

At the close of this chapter and in order to introduce the next one, it is well known that discharge voltage influences the interface phenomena during the MPW process. However, in our study, we do not have much choice to select large range of discharge voltages. Using various field-shaper materials is another choice to change the interface impact intensity as they have different electrical conductivities and can produce different velocities. Therefore, in the next Chapter, we will combine the discharge voltages and different field-shaper materials to obtain various impact conditions and investigate how the impact intensity influences the interface dynamic phenomena for MPW Al/Cu combinations.

Chapter 3

Assessing the influence of field-shaper material on magnetic pulse welded interface of Al/Cu joints

As field-shaper enables to increase the magnetic pressure applied on the workpieces and thus improves the welding efficiency. Therefore, in this chapter, the effects of field-shaper material on magnetic pulse welded interface of Al/Cu joints were first investigated. Then, we further extend our investigations to the microstructure evolution and mechanical behaviour of Al/Cu magnetic pulse welds. This chapter is partly from the paper "J.S. Li, R.N. Raoelison, T. Sapanathan, G. Racineux, M. Rachik. Assessing the influence of field-shaper material on magnetic pulse welded interface of Al/Cu joints. Procedia Manufacturing, Vol 29, pp. 337-344, 2019. https://doi.org/10.1016/j.promfg.2019.02.146".

3.1. Abstract

In this chapter, we compare the efficiency of four field-shapers made of Cuprofor, Siclanic, CuBe2 and Steel. The welding conditions with a discharge voltage of 6 kV (low impact intensity) and 8 kV (high impact intensity) were respectively used to weld a combination Al/Cu. The steel field-shaper used with 6kV cannot successfully produce a weld. Welding performed using CuBe2 and Siclanic field-shapers with 6kV produces similar features of the welded interfaces, which are: wavy zone, swirls, cracks, discontinuous intermediate (IM) layers, and a few IM pockets. Cuprofor field-shaper with 6kV also generates these features but the welded interface reveals significant large kinetic instabilities with a presence of large vortex, large holes within swirls and a porous structure. With a voltage of 8kV, the steel field-shaper generates welds that contain many IM pockets with small area. In case of (Cuprofor, 8kV), the welded interface reach to the highest instabilities among all the welded cases. It contains large amount of IM pockets with large area, cavities and

cracks. These results clearly show the importance of choosing the appropriate combination of field-shaper material and discharge voltage to produce successful welds with their specific interfacial feature. EDS analyses show that Cu fragments and Al_2Cu coexisted in an IM zone which is formed by mechanical mixing combined with melting under low impact intensity. TEM results reveal that an anomalous wave is formed with the IM zone and an 70 nm interdiffusion zone. Nanohardness tests show that compared to base metals, the IM layers exhibit higher hardness due to the presence of intermetallic compound. The heterogeneous nanohardness in the IM layers is due to the various porous densities across various indented positions. The nanohardness increases when the porous density is low. The IM layers with low porous density exhibit less “pop-in” events and smaller displacement shifts in the load-displacement curve. This phenomenon is much more obvious under high strain rate indentation tests compared to that under the low strain rate indentation tests.

3.2. Introduction

A field-shaper (FS) is widely used in MPW for an efficiency improvement. It enables to increase the magnetic pressure applied on the workpieces during welding. However, FSs are prone to have fatigue damage due to the use of high frequency impulse current and the subsequent cyclic loadings of the MPW process [67]. Various studies were focused on the improvement of FS longevity [67,146] and efficiency by introducing optimized shape designed to be suitable for specific applications [65,66]. However, FS effects on the weld features have not been considered in such investigations.

During MPW, the interface zones experience severe plastic deformation which produces complex and heterogeneous interface [147]. Meanwhile, the high impact intensity enables to produce large amounts of heat at the interface [71]. Nevertheless, there is insufficient time for the heat dissipation before a thermal softening. This situation probably results in heat accumulation at the interface that leads to partial melting and formation of IM layers at the interface. These IM layers are critically

affecting the quality of the welds. Therefore, the mechanical characterization of these IM layers is important for understanding the interface bonding mechanism and for improving the joint quality. In general, nanoindentation characterization technique is used to study the local mechanical properties and deformation behaviour [148]. Although many works dedicated to the nanoindentation properties of the welded interface, the results are mainly limited to the comparison of the nanohardness of the IM layers with the base metals [23–26]. Those findings generally identify that the nanohardness of the IM layer is higher than that of the base metals due to phase transformation, ultra-fine structure and localized plastic deformation [17,87,131,149]. The presence of porous zone has been identified within the IM layers of Al/Cu MPW joint [51] that could influence the hardness behaviour of the layers. However, no work has been reported so far on the mechanical properties influenced by the response of the porous structure under various strain rates.

3.3. Experimental procedure

3.3.1 Welding conditions

Al6060 T6 was chosen as flyer and pure copper was used as inner part in this study. The chemical compositions of both materials are reported in Table 3.1. Four FS materials (40CrMnMoS86 steel (DIN 1.2312), CuBe2, Siclanic and Cuprofor®) were used. Mechanical and electrical properties of those FS are given in Table 3.2. With different electrical conductivities, these four materials generate different impact intensities that produce different interfacial characteristics. The steel FS has excellent mechanical properties, good machinability and high-dimensional stability. The CuBe2 is a precipitation hardening copper alloys and also plays an important role as carrier materials for electrical contacts. The Siclanic is a Cu-Ni-Si alloy, hardened by the precipitation of Ni_2Si phase, which is a promising candidate in electromagnetic applications for good mechanical properties without compromising the electrical conductivity. The Cuprofor® is a Clal patented Cu alloy (with 0.28% Co and 0.08% P) which provides good mechanical properties along with the typical characteristics of

excellent thermal and electrical properties of Cu.

Table. 3.1 Standard chemical compositions of the Al6060 T6 and Copper.

Material	Mg	Si	Fe	Mn	Cr	Zn	Ti	Cu	Al
Al6060T6	0.8-1.2	0.4-0.8	0.7	0.15	0.04-0.35	0.25	0.15	0.15-0.4	Balance
Copper	-	-	-	-	-	-	-	99.9	-

Table. 3.2 Mechanical and electrical property of the FS used in the experiment.

Field-shaper	Steel	CuBe2	Siclanic	Cuprofor
Electrical Conductivity (10^7S/m)	0.58	1.45	2.67	5.16
Young's Modulus (GPa)	210	125	130	140
Poisson's Ratio	0.29	0.29	0.29	0.29
Density (g/cm^{-3})	7.9	8.2	8.9	8.9

The welding tests are performed on tubular assemblies using a single turn coil with the FS connected to a PULSAR® welding system equipped with 690 µF capacitor bank. The discharge pulse frequency is 22 kHz which was measured by a Rogowski probe inside the working station. A 3D schematic illustration of the assembly consisting of one turn coil with a FS is shown in Fig. 3.1a. The selected various FSs are presented in Fig. 3.1b. Cross section views of workpieces assembly before and during welding propagation are shown in Fig. 3c and d, respectively. The inner part with a diameter of 15.94 mm is inserted inside the flyer tube having an outer diameter of 22.22 mm and a thickness of 1.50 mm. The air gap and overlap distance between flyer tube and inner part are 1.64 mm and 10 mm, respectively. Welding was performed with input voltages of 6 kV (low impact intensity) and 8kV (high impact intensity), respectively.

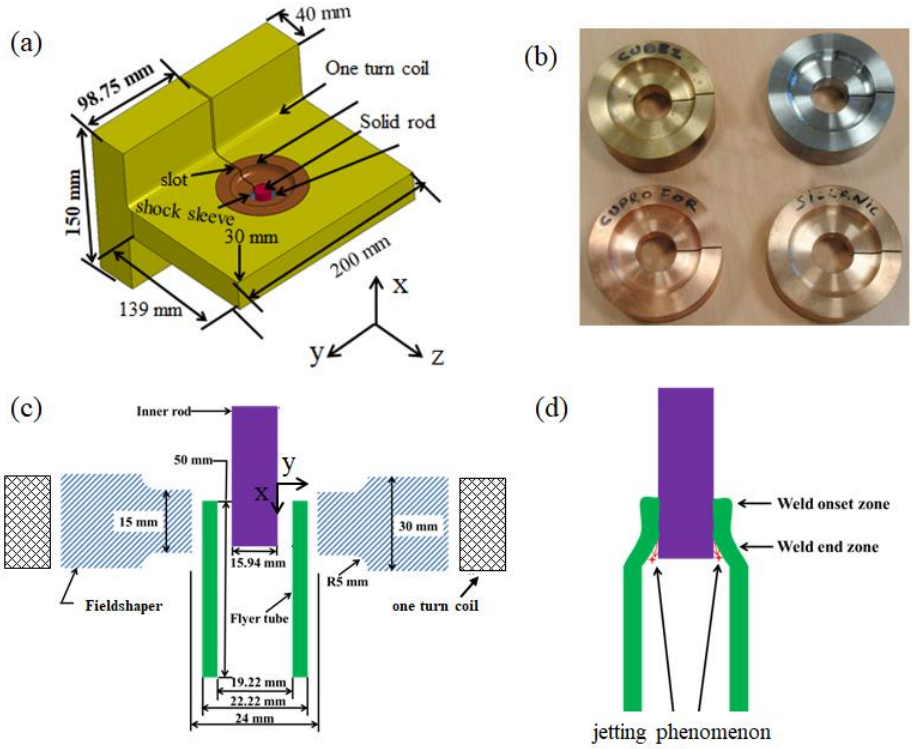

Fig. 3.1 Schematic illustrations of MPW process: (a) 3D isometric projection of the MPW assembly; (b) four different FS used for the MPW tests: CuBe2, Steel, Cuprofor, Siclanic; a cross-section view of workpieces assembly (c) prior to the welding and (d) during the collision propagation.

3.3.2 Metallurgical and mechanical characterization

After the welding process, the welded specimen was dissected along the longitudinal cross-section (parallel to the x axis in Fig. 3.1c) by a micro chain saw cutting machine to prepare samples for microstructural characterization under standard metallurgical sample preparation techniques. Interface morphology and microstructural observations were made using an optical microscope (OM) and ZEISS Ultra 55 Scanning electron microscope (SEM) at an accelerating voltage of 15kV in both Secondary Electron (SE) and Backscattered Electron (BSE) modes. Energy-dispersive X-ray spectroscopy (EDS) was conducted to characterize the chemical compositions of the interface. The microstructure at the interface was also examined by transmission electron microscopy (TEM, JEM-2100). The TEM samples (12 μm × 10 μm × 100 nm) were extracted by a focus ion beam machine. Nanoindentation experiments were performed using Agilent G200 Nanoindentor with

Berkovich diamond tip. Indentations were carried out with the maximum displacement of 1000 nm and a holding time of 10 seconds at peak load. To measure the strain rate sensitivity at the interface zone, the indentations were repeated with the strain rates of 0.05 s^{-1} and 0.3 s^{-1}, respectively.

3.4 Effects of FS material on Al/Cu welds under low impact intensity

3.4.1 Al/Cu interface in case of steel FS

Among those FSs, the steel FS fails to generate a welded interface under the welding conditions of low impact intensity (input voltage of 6kV). The interface is not bonded due to more electrical losses caused by the low electrical conductivity of steel. That is, the induced magnetic field is not sufficiently high to produce the required Lorentz force, thus the experiment does not enable to meet both requirements of pressure and impact velocity for welding. To obtain a weld using steel FS, more energy is required. Generally, increasing the charging voltage allows such achievement but impairs the FS's service life due to the subsequent increase in mechanical stresses [67]. For this reason, effective welding should also ensure a good service life of FS. Thus, the use of low conductive FS becomes tricky when large weldability window is required, whereas the other FSs lead to a successfully Al/Cu weld as detailed hereafter.

3.4.2 Al/Cu interface in case of CuBe2 FS

The electrical conductivity of the CuBe2 FS is twofold higher than that of steel FS (see Table 3.2). This difference is sufficient to create a welded joint under the tested conditions of 6kV. Fig. 3.2 shows a cross-sectional view of the whole interface and finer details from SEM observations. The aluminum flyer is effectively welded (interface without large amount of IM layers) on the Cu part over a distance of 3.6 mm approximately, from a region of about 4.1 mm away from the zone where flyer impact the fixed rod (Fig. 3.2a). A wavy nature of the weld starts at the zone b (Fig. 3.2b) that means an onset of excessive shearing causing such interfacial instability

[52]. There is a development of this wavy morphology along the welded interface before it collapses after certain distance 5.6 mm to give a straight welded interface, i.e., a zone where shear instability begins to disappear (after zone i). The waves amplitude does not exceed 30 µm and the wavelength varies in between 100-200µm from the zone b towards the zone i.

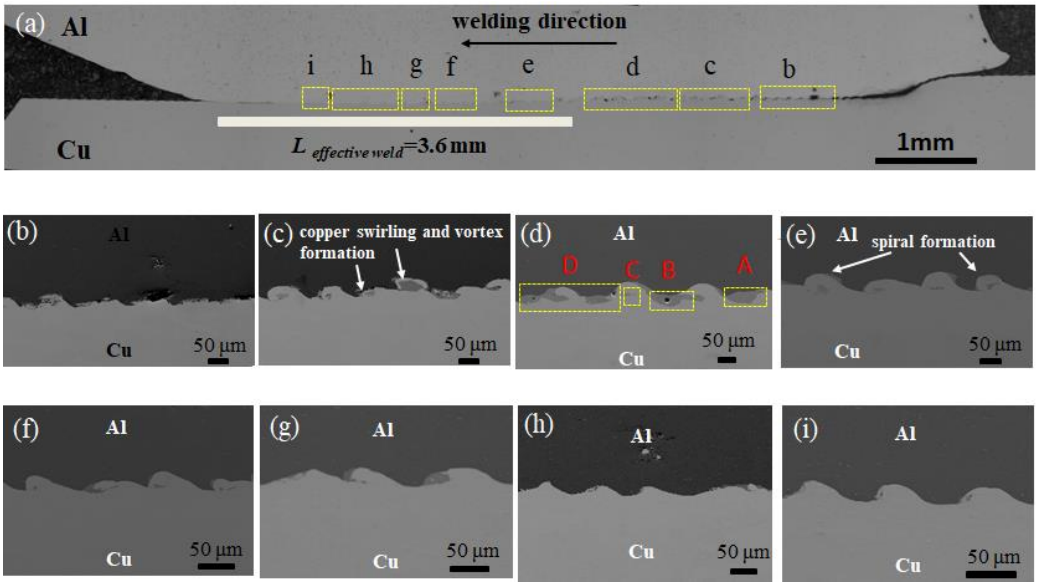

Fig 3.2. Typical cross-sectional view and interfacial characteristics of various zones along the interface produced with CuBe2 FS and input voltage of 6kV. (a) cross-sectional micrograph of the MPW weld where separate regions are marked by b-i, (b) unwelded zone at the onset of welding, (c) vortices; (d) continuous IM layers along the interface, (e) interface with spirals formation; (f) - (i) wavy interface. (b)-(i) corresponds to the magnified images of the areas marked by 'b-i' in (a), respectively.

The interface feature also includes the presence of IM phases (which could have trapped jetted materials, remaining surface oxide layer and intermetallic compounds) within the wavy zone (WZ). Caused by a confined melting and abrupt solidification [27], this IM phase characterizes a rather harmful nature of the welded joint due to cracking and fragmentation they create during solidification. Along the interface, the IM phase appears as discontinuous pockets (Fig. 3.2c and e) and continuous layers with heterogeneous thickness (Fig. 3.2d). Within some sites of the interface, the instability evolved towards advanced stages that are vortices and swirls due to

excessive shearing. The zone c (Fig. 3.2c) shows several vortices with some swirls containing IM phase. These features evidence that from steel FS to CuBe2 FS, the change in electrical conductivity strongly affects the weld formation and development. The complex interface morphologies are correlated with the dynamic impact parameters during MPW process, which will be further discussed in combination with simulation results in the section.5.3.1 in chapter 5.

3.4.3 Al/Cu interface in case of Siclanic FS

The interface characteristics produced during MPW with Siclanic FS and input voltage of 6kV are displayed on Fig.3.3. Basically, the macroscopic interface observations of both CuBe2 FS and Siclanic FS cases are similar. Onset of instabilities produced by the CuBe2 occurs also for the Siclanic case, viz the wavy shape at the onset of bonding surface (zone b as shown in Fig. 3.3b) and the progressive development of this instability along the welded joint until the collapse at the end zone. The wavelength and the amplitude of the waviness are about 100 μm, and 20 μm, respectively. The effective weld length is about 4.2 mm that starts about 2.7 mm away from the onset of the collision.

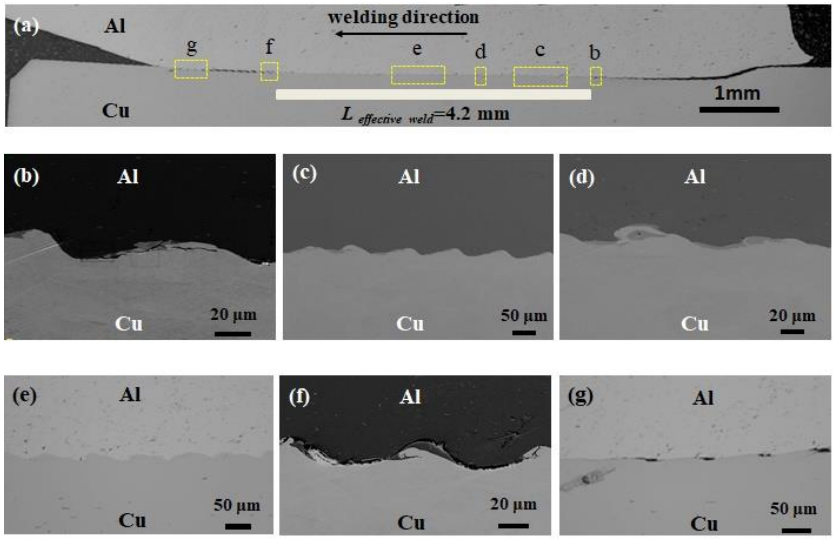

Fig. 3.3. Typical cross-sectional view and interfacial characteristics of various zones along the interface produced with the Siclanic FS and input voltage of 6kV during MPW. (b)-(g) correspond to the magnified images of the areas marked by ‘b-g’ in (a), respectively.

Onset of swirls exists with WZ as illustrated in zone d (Fig. 3.3d). There is less intermediate phase affected zone (IPAZ) compared to the CuBe2 FS case, but the intermediate (IM) zones (zone b, zone d) exhibit similar features in terms of morphology (discontinous layers and pockets) and defects (cracks). The Siclanic FS case generates thiner IM phase maximum of 9µm and mostly free of interface defects which indicates that the weld has strong mechanical strength compared to the weld produced with the CuBe2 FS.

3.4.4 Al/Cu interface in case of Cuprofor FS

The cross-sectional view and high magnification images of interface features in case of Cuprofor FS are presented in Fig 3.4. This FS induces higher velocity during MPW among those 4 FSs because of its higher electrical conductivity. The length of the effective weld joint is 3.2 mm (slightly shorter than the case of CuBe2 and Siclanic). The previous interfacial characteristics similar to the one observed with CuBe2 and Siclanic FSs were also observed here, but the interface response produces more kinetic instabilities that result in large vortices, large holes within swirls, cracks inside the intermediate layer and porous IM phase. The welded joint subjected to higher impact velocity and then higher interfacial shearing becomes defective, globally. More cracking and fragmentation occur along the interface due to the influence of IM media combined with the strong instabilities. The IM layers exhibit thicknesses of up to 37µm which can contain large holes with up to 7µm in diameter in zone c (Fig. 3.4c-1). The IPAZ becomes porous (Fig.3.4c and e) which is due to an ultra-high heating and cooling rates [89]. The location of the large hole at the centre of the IM pocket confirms the further development of the interfacial swirls into vortex. The formation of the hole is due to the centrifugal force in the IM pocket results from the swirling radially that breaks the melted IM prior to solidification. This intense instability well corresponds to a phenomenon involved by more intense collision due to the higher electrical conductivity of the Cuprofor FS. At the end of weld, the interfacial instability creates significantly large voids whose size can exceed 35µm (Fig. 3.4g). The formation of those very large voids can be explained as results of

jetting of molten fluid, solidification shrinkage, and/or local fragmentation combined with particulates jetting governed by shear stresses [61]. The intensity of the impact is also revealed by the wave's characteristics. The maximum wavelengths is 200μm with maximum amplitude of 35μm.

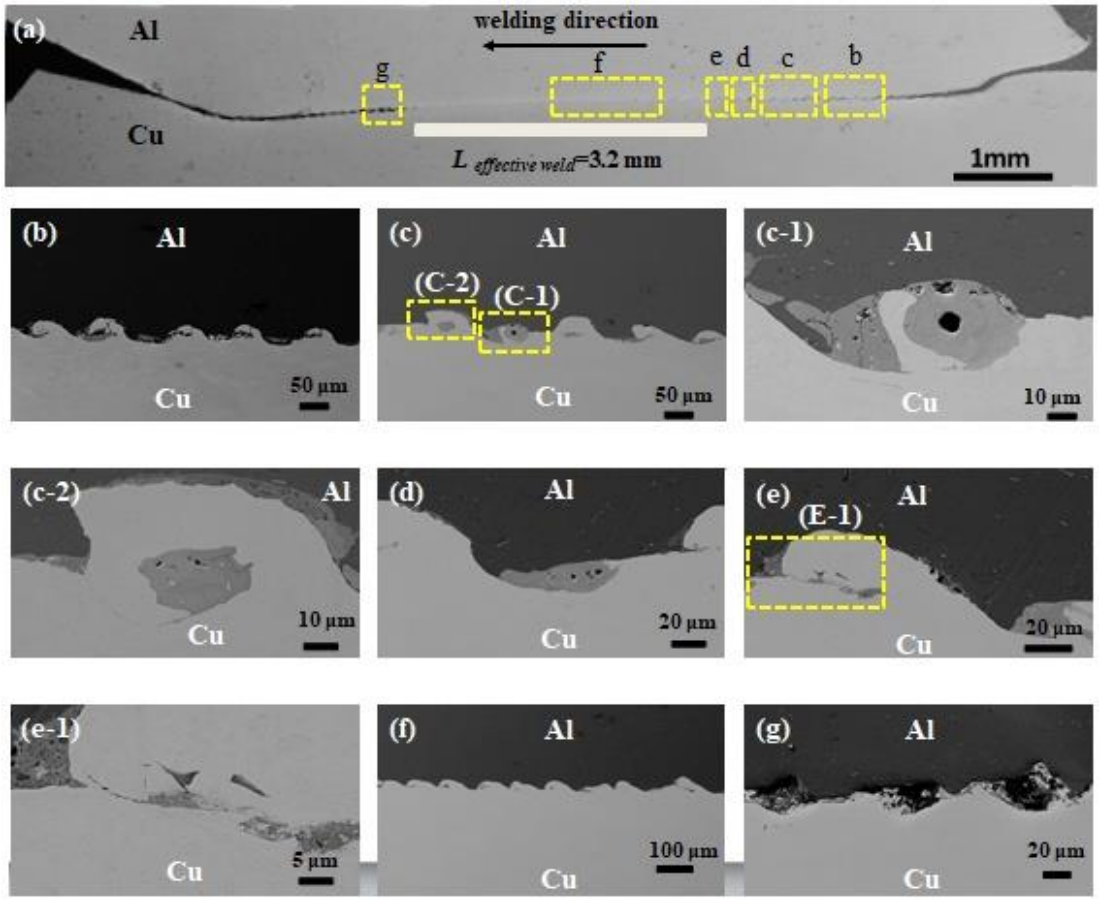

Fig 3.4. Typical cross-sectional view and interfacial phenomena of various zones along the interface produced with the Cuprofor FS and input voltage of 6kV during MPW. (b)-(g) correspond to the magnified images of the areas marked by 'b-g' in (a), respectively. (c-1), (c-2) are taken from the areas (C-1), (C-2) marked in Fig. 3.4c, respectively. (e-1) is taken from the area (E-1) marked in Fig. 3.4e.

3.5 Effects of FS material on Al/Cu welds under high impact intensity

3.5.1 Al/Cu interface in case of Steel FS

When compared with case of (Steel FS, 6kV), the steel FS successfully produced

a joint under the high impact intensity with input voltage of 8kV, as shown in Fig. 3.5a. This is due to the increasing of input voltage that enables to meet both requirements of pressure and impact velocity for welding. The effective weld length is about 5.4 mm under this welding condition. It is much longer than that in the previous weld cases under low impact intensity. With the comparison of the weld case of (CuBe2 FS, 6kV) and (Steel FS, 8kV) with the case of (Steel FS, 6kV), we can notice that the former increases about 2.5 times of the electrical conductivity and the latter increases about 1.3 times the input voltage. However, the interface produced with (Steel FS, 8kV) shows more kinetic instabilities compared with the joint produced with (CuBe2, 6kV), that evidenced large number of melt zones along the interface (marked by black arrows), as shown in Fig. 3.5a1. This suggests that increasing the input voltage is much easier to generate high impact intensity compared with the effect of increasing the electrical conductivity by changing the FS material.

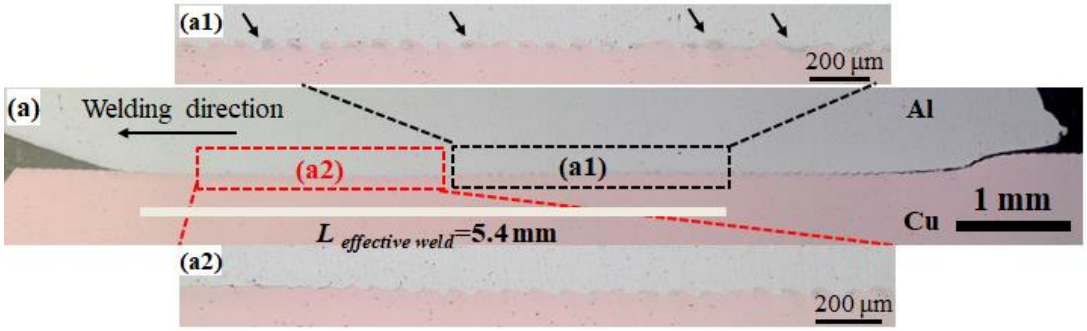

Fig. 3.5. Typical cross-sectional view and interfacial phenomena of various zones along the interface produced with Steel FS and input voltage of 8kV during MPW.

3.5.2 Al/Cu interface in case of Cuprofor FS

The interface of the case of (Cuprofor FS, 8kV) reaches highest instability among all the weld cases, due to the combination of highest electrical conductivity of the FS and highest input voltage. The effective weld length is about 2.0 mm. We can clearly see large amounts of melting pockets and cavities (marked by red arrows) at the interface, as shown in Fig. 3.6a1. The area of the pockets is much larger than that in the case of (Steel FS, 8kV). This is due to the difference of the heat accumulation at the interface that will be discussed in detail in Chapter 6. Moreover, ejected material

was also observed at the end of the interface, as shown in Fig. 3.6a2. During MPW, large localized pressure waves created at the collision point during the welding process travels the interface with high velocity. Oppositely, the collision point progresses forward at a slower rate, i.e. subsonic rate, as reported by [133]. Therefore, the created pressures at the interface are sufficient to produce a strong shearing which generated a jetting phenomenon (Fig. 3.1d) at the interface [108]. According to results in [141], this jetting phenomenon can remove the surface oxides and impurities from the impacting surface and promote sound bonding. The simulation results in [27] revealed that the temperature of this expulsed materials is very high, enough to melt the aluminium. The authors also explained the ejection material is significantly prominent in the case defective welded joints containing discontinuous cavities which are also observed in our case (Fig. 3.6a1).

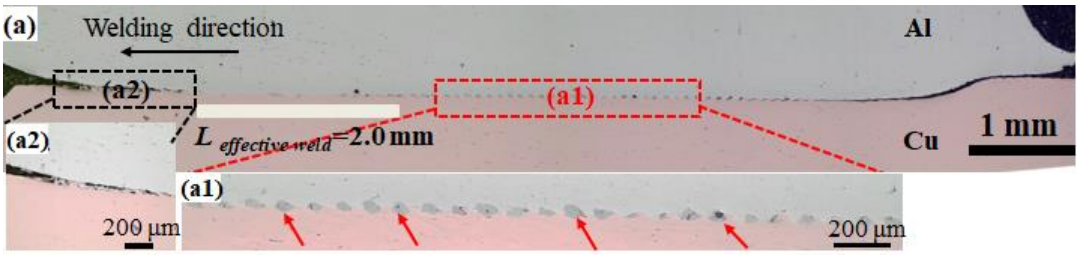

Fig. 3.6 Typical cross-sectional view and interfacial phenomena of various zones along the interface produced with Cuprofor FS and input voltage of 8kV.

3.6 Microstructural characterization

3.6.1 Microscopic characterization of intermediate layers

From the cross-sectional analysis in previous sections, we know that IM layers are inevitable along the interface during MPW. Therefore, more details are required to discuss these zones. Here, we selected a typical zone containing IM layers, as shown in Fig. 3.7, which are taken from the interfacial area (Fig. 3.2d) in case of (CuBe2 FS, 6kV). Fig. 3.7a-d shows the detailed SEM images revealing more complex morphologies within the IM layers. The thickness of the IM layers varies from 1.2 µm to 37.6 µm along the interface. Fig. 3.7a shows a clear mixing pattern of the eddy trajectories in the IM layers. As the collision point advances, a swirling of

the materials was induced at the interface due to the shear instability. Therefore, the interface materials twist and roll up like in a fluidic interface to form vortex. This phenomenon is usually explained as Kelvin-Helmholtz instability result caused by a shearing instability across the interface of two fluids. When the interface instability reaches advanced stages, the material within the vortex experiences large velocity gradient and form the motion trajectories of the swirling flow.

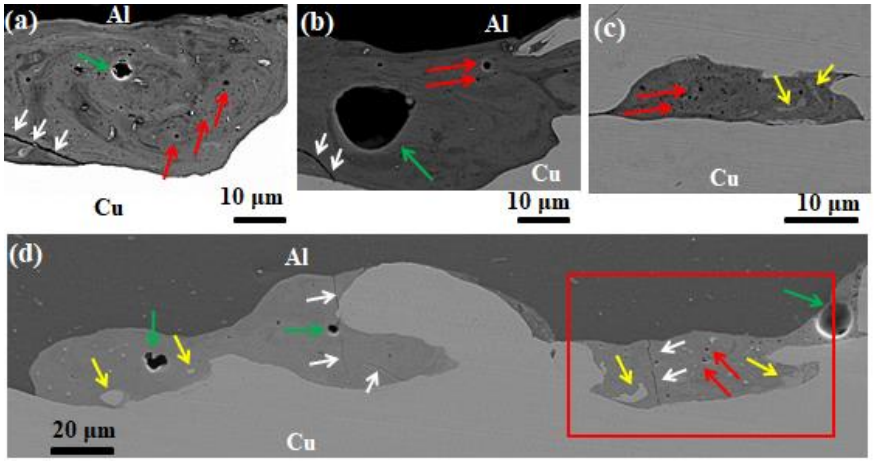

Fig. 3.7. Microstructures of the IM layers showing (a) swirling and porous structures; (b) mesoscale cavity; (c) adjacent intermixing zone with micro porous structures; (d) microcracks bounded in the IM layers; (a), (b), (c) and (d) are taken from the areas A, B, C and D marked in Fig. 3.2d, respectively. The mesoscale pores, microcracks and Cu fragments are highlighted by green, white and yellow arrows, respectively.

Pores with micron/submicron size also appear within the IM layers. When comparing their size, we can classify them into two types: pore diameters smaller than 1.0 μm (micron pores) (marked by red arrows) and mesoscale pores with their diameters between 2.8 μm and 15 μm (marked by green arrows). Moreover, the micron pores present a random distribution while the mesoscale cavities always appear in the middle of the IM layers. This indicates that their formations are governed by different physical mechanisms, which will be deeply discussed using simulations in chapter 6.

Some microcracks are also observed inside the thick zones of the solidified melted IM layers (indicated by white arrows in Figs. 3.7a, b and d), and they are

bounded within the IM layers and never propagate inside the Al or Cu. The microcracks are probably resulting from thermal residual stress induced by the temperature gradient between the solidified melted and the parent metals during the solidification shrinkage of the welded structure [150].

In Fig. 3.7c and d, some fragments (marked by the yellow arrows) were also found in IM layers. In order to understand the chemical compositions of the IM layers, EDS maps of Al and Cu are further analysed within a selected IM zone (marked by red rectangle in Fig. 3.7d). Fig. 3.8a and b show the EDS mapping for Al and Cu respectively, and Fig.3.8c shows both Al and Cu maps. Fig. 3.8d shows the quantitative analysis of weight fraction of Al and Cu in the regions A, B and C (marked in Fig. 3.8c). It confirms the fragments are Cu and the intermetallic compound is Al_2Cu in the IM layers according to the atomic percentage. The combined formation of the liquid/solid interface within the IM zone, the high pressure and high temperature could promote the fast reaction and diffusion kinetics of Cu in Al liquid, and results in the formation of Al_2Cu [151].

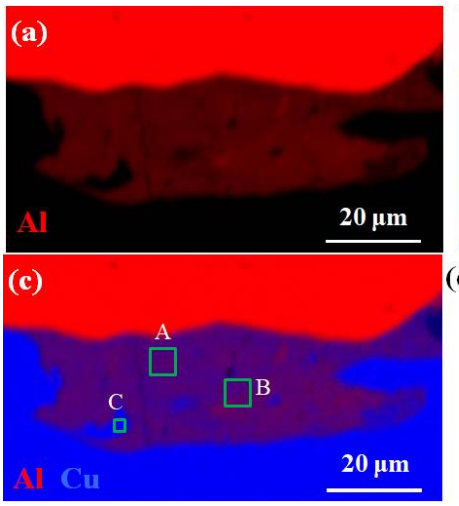

(d)

Region	Weight (%)		Corresponding phase
	Al	Cu	
A	49.29	50.71	Al_2Cu
B	49.33	50.67	Al_2Cu
C	0.37	99.63	Cu

Fig. 3.8 EDS analysis: (a) Elemental map of Al, (b) Elemental map of Cu, (c) Elemental map of Al and Cu, (d) EDS results for the square regions corresponding to A, B and C in Fig.3.7g.

3.6.2 Nano-scale characterization of wave formation

A SEM observation of the distinctive anomalous wave at the Al/Cu interface

reveals an irregular feature of the wavelength and amplitude (Fig. 3.9a). The wave propagation direction of the anomalous wave is consistent with the welding direction. Moreover, there exists some trapped intermediate zones (IMZs) along the interface, bounded within the front of wave zone or exposed at the bimetallic welded interface. The thickness of the IMZs varies in the range of [3 mm, 20 mm]. Fig. 3.9b shows the inner architecture of IMZs revealing nanoscale porous structures.

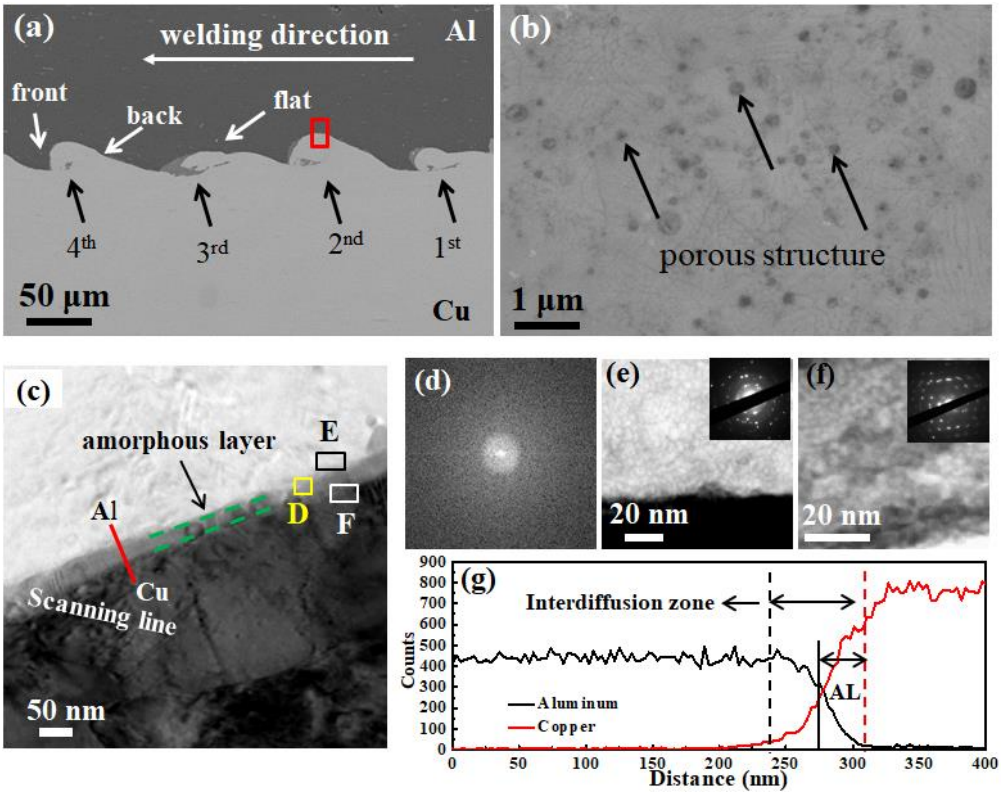

Fig. 3.9. (a) SEM observation showing an anomalous wave interface from Al/Cu weld with CuBe2 FS and input voltage of 6kV, (b) SEM image of inner porous architecture of IMZs, (c) TEM observation taken from the wave interface indicated by the red rectangle in (a); TEM images and selected area electron diffraction (SAED) patterns in (d), (e) and (f) correspond to regions D, E, F marked in (c); (g) EDS revealing the distribution of Al and Cu along the red line marked in (c).

TEM observations were further used to unravel the metallurgical changes and the bonding mechanism at the interface with the absence of IMZs along the anomalous wave SEM observation (marked by red rectangle in Fig. 3.9a), and the results are presented in Figs. 3.9c-g. A thin layer of third material with the width of 30 nm was

observed at the interface (Fig. 3.9c). The selected area observed by an electron diffraction (SAED) pattern (Fig. 3.9d) taken from this thin layer (region D in Fig. 3.9c) shows a diffuse halo and confirms that the third layer consists of amorphous phase (AP). The SAED patterns corresponding to the TEM observations from the aluminium and copper sides adjacent to the interface (regions E and F in Fig. 3.9c, respectively) exhibit the Debye ring diffraction that indicates nanocrystalline features (Figs. 3.9e and f). The EDS analysis in Fig. 3.9g presents an obvious gradual interdiffusion of Al and Cu elements across the interface. One should note that the interdiffusion zone having the width of ~70 nm (Fig. 3.9 g) is slightly broader than the width of the amorphous layer (i.e. ~30 nm) in the Cu-rich side. This observation suggests that there is a possible formation of supersaturated solid solution in the Al-rich side.

3.7 Summary and recommendations

Table 3.3 shows the similarity and dissimilarity of the interface features generated with different welding conditions during MPW. In the case of (CuBe2 FS, 6kV), lower velocity was obtained and there is no sufficient jetting that can involve the higher instabilities in the interface, but the thickest intermediate phases (40 μm) which may contain jetted materials and intermetallic compounds were found in the weld interface among the welded case. The weld produced using (Siclanic FS, 6kV) is highly promising and it indicates an accurate jetting and resulted in a regular feature. Interface produced under this case only has a maximum of 9μm IMP. For (Coprofor FS, 6kV), the welded region presents significant instabilities which may result from melting solidification, or from formation of thick intermediate phase likely composed of intermetallic compounds (relatively thick compare with the Siclanic result). Among those FSs with 6kV cases, the longest effective welded length 4.2 mm was found at Al/Cu interface produced with (Siclanic FS, 6kV). When increasing the voltage to 8kV, the interface instabilities increase and large amount of IM layers were found with both Steel and Cuprofor FS. The effective weld length increases to 5.4 mm for

(Steel, 8kV) whereas it decreases to 2.0 mm for (Cuprofor FS, 8kV). These results demonstrated that Siclanic FS can achieve the best welding interface compared with the other FSs under the discharge voltage of 6kV. Moreover, increasing the discharge voltage can somehow increase the weld length with the FS with low conductivity, but at the same time, the weld interface also appeared with much more instabilities.

Table 3.3. Similarity and dissimilarity of the interface produced with various welding conditions (WCs) during MPW.

		Interface features				
		Similarity	dissimilarity			
		-	effective welded length	Maximum thickness of IMP	Period waves	Other phenomena
WCs	(Steel FS, 6kV)		-	-	-	-
	(CuBe2 FS, 6kV)		3.6 mm	40μm	**Length:** 100-200 μm **Amplitude:** 0-30 μm	Fragmentation, IM layers
	(Siclanic FS, 6kV)		4.2 mm	9 μm	**Length:** about 100 μm **Amplitude:** about 20μm	a small amount of IM layers and cracks
	(Cuprofor FS, 6kV)	wavy zone, swirls, vortex, cracks, IM layers and pockets	3.2 mm	37 μm	**Length:** 100-200 μm **Amplitude**: about35μm	large vortex, large cavities, porous IMP, large voids with size exceeding 35μm
	(Steel FS, 8kV)		5.4 mm	45 μm	**Length:** 75-150μm **Amplitude:** about 37.5μm	Swirling, cavities
	(Cuprofor, 8kV)		2.0 mm	60 μm	**Length:** about100 μm **Amplitude:** about 20μm	jetting material, large amount of IM layers, cavities, cracks

From the above experiments, we know that an appropriate impact velocity is crucial to obtain a good welding. Various FSs have different electrical conductivities

and produce different velocities, and thus influence the quality of the interface. However, blindly selecting a FS with high conductivity material may cause excessive speed and damage the weld interface. Increasing the charging voltage is another method to improve the velocity when using low conductive FS materials, but it may also impair the FS's service. Therefore, further work should be performed on more welded joints influenced by different charging voltages and FS with various electrical conductivities. The service life of FS under different input voltages can help to identify and optimize the process conditions for effective applications. Numerical simulations can also be used to further investigate the interfacial instability and governing mechanisms under those welding conditions.

3.8 Mechanical properties of the IM layers

3.8.1 Hardness measurement of the welds

Nanohardness distribution across the Al/Cu welding interface was measured to further understand the mechanical properties of the IM layers. Here, we selected the weld case of (Cuprofor, 8kV) since it contains large amounts of IM pockets. Each test point was set with a distance of 30 μm to ensure at least one indentation positioned exactly on the IM layer. The nanoindentation tests are performed at strain rate of 0.05 s^{-1}. Fig. 3.10 presents the nanohardness distribution along the interface. The average hardness of the IM layers is almost four or five times that of the base metals. One may note that the variation in hardness of IM layers is much larger than that of other regions further from the interface. This can be possibly attributed to the various intermetallic compounds and/or various porous densities in the IM layers, which will be further discussed in section 3.8.3. Moreover, the nanohardness in the vicinity of the interface also increased compared with that of the base metals. This is due to the interface subjected to severe plastic deformation that induced grain refinement near the interface. SEM nanohardness mapping for the base metals and IM layers is given in Fig. 3.11. Substantial pile up was observed at the aluminium and copper indents while limited pile up was observed in the IM indent.

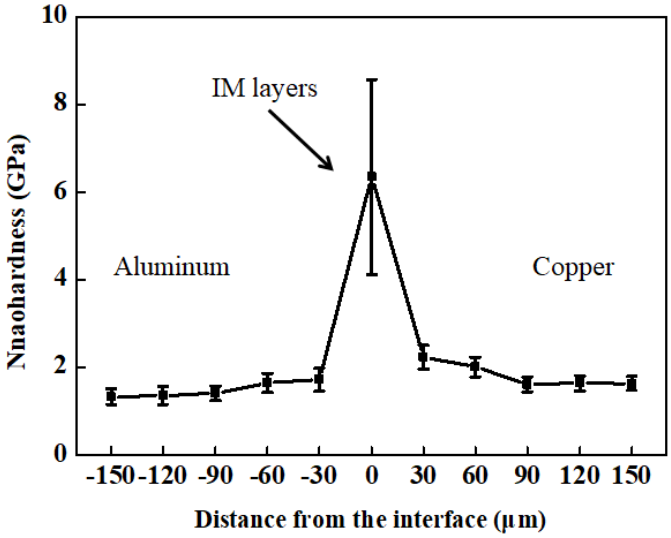

Fig. 3.10 Nanohardness distribution along the interface, error bars stand for standard deviation. Nanohardness tests performed at strain rates of 0.05 s^{-1}.

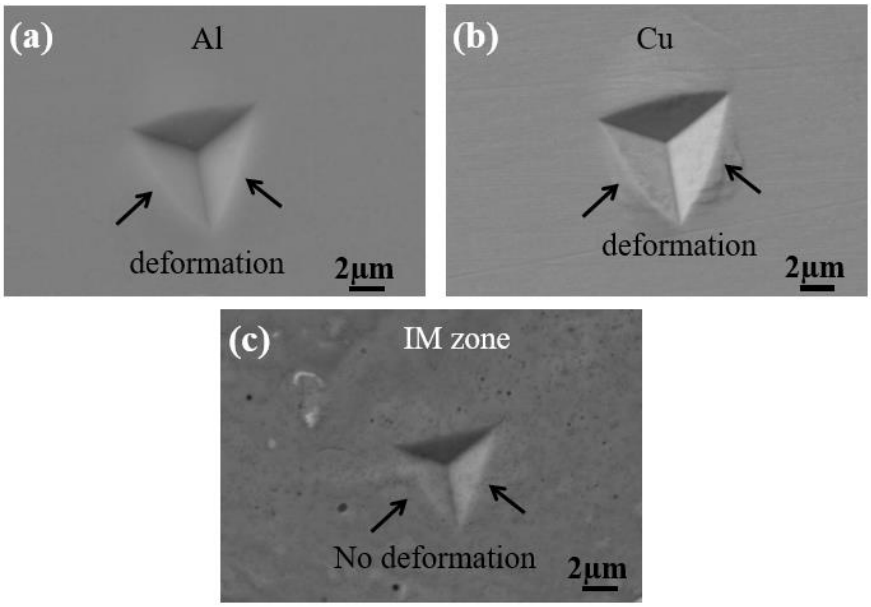

Fig. 3.11 SEM nano-hardness mapping at the interface (Cuprofor, 8kV): (a) Aluminium, (b) Copper, (c) IM zone.

3.8.2 Effects of the strain rates on the local mechanical behaviour

During the nanoindentation tests, force and displacement are recorded as the indenter tip is pressed into the test material's surface with a prescribed loading and unloading profile. The response of interest is the load-displacement curve (often called the P-H curve). Fig. 3.12 shows the P-h curves for nanoindentation on Al, Cu and the IM layers with two different points, at different strain rates. P-h curves in Fig.

3.12a are punctuated by frequent pop-in events of rapid displacement when the nanoindentation tests are performed on the IM layers at the strain rate of 0.05 s^{-1}. These discrete pop-in events are similar to the serrated flow found in the displacement controlled compression tests on the Al-Cu alloys [152]. Wherein, each serration corresponds to a single shear band to accommodate the applied strain and drop of the load. Notably, the pop-in events appear with different features for the case of the IM layers at different locations (point 1 and point 2). As the strain rate is increased to 0.3 s^{-1}, the nature of the pop-in events changes dramatically, from large number of pop-in events (Fig. 3.12a) to lower number of pop-in events (Fig. 3.12b), for the IM layers in both point 1 and point 2. It indicates that the displacement is strongly affected by the indentation strain rate. The plastic deformation becomes continuous as the strain rate increases due to the decreasing number of the pop-in events inducing shear bands [153,154]. Although the characteristics of the serrated flow are affected by the strain rate, the general shapes of the P-h curves are very similar at different strain rates for the IM layers at same location, revealing the strain rate does not significantly affect the hardness.

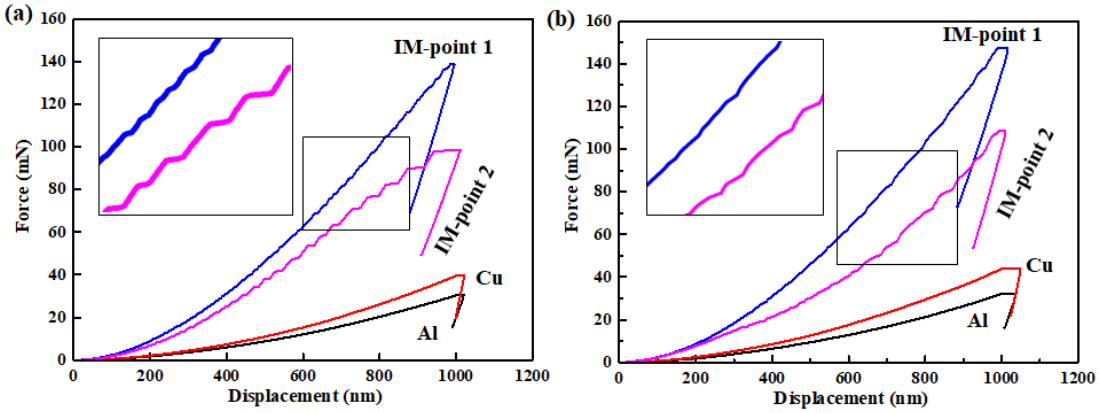

Fig. 3.12. P-h curves obtained from the nanoindentation experiments for Al, Cu and the IM layers at the strain rates of (a) 0.05 s^{-1}, (b) 0.3 s^{-1}.

3.8.3 Effects of the porous density on the local mechanical behaviour

The results in sections 3.8.1 and 3.8.2 reveal that IM layers have different nanohardness at different locations. Next, we further performed a high-resolution

nanoindentation test on IM layers to understand the influencing factors on this phenomenon. A strain rate of 0.05 s^{-1} was used to perform nanoindentation in an array fashion to obtain a map of hardness distribution across the interface, at an imposed maximum depth of 250 nm.

Fig.3.13a shows the SEM image of the array of indents. The array is consisted by 100 (10 × 10) indents with a distance between indents of 6.25 μm. The corresponding nanohardness map is shown in Fig. 3.13b. The results show that all the nanohardness data in the IM layer is higher than that of both parent metals. As discussed in section 3.8.1, the increase of the nanohardness in IM layers compared with base metals is due to the formation of intermetallic compound.

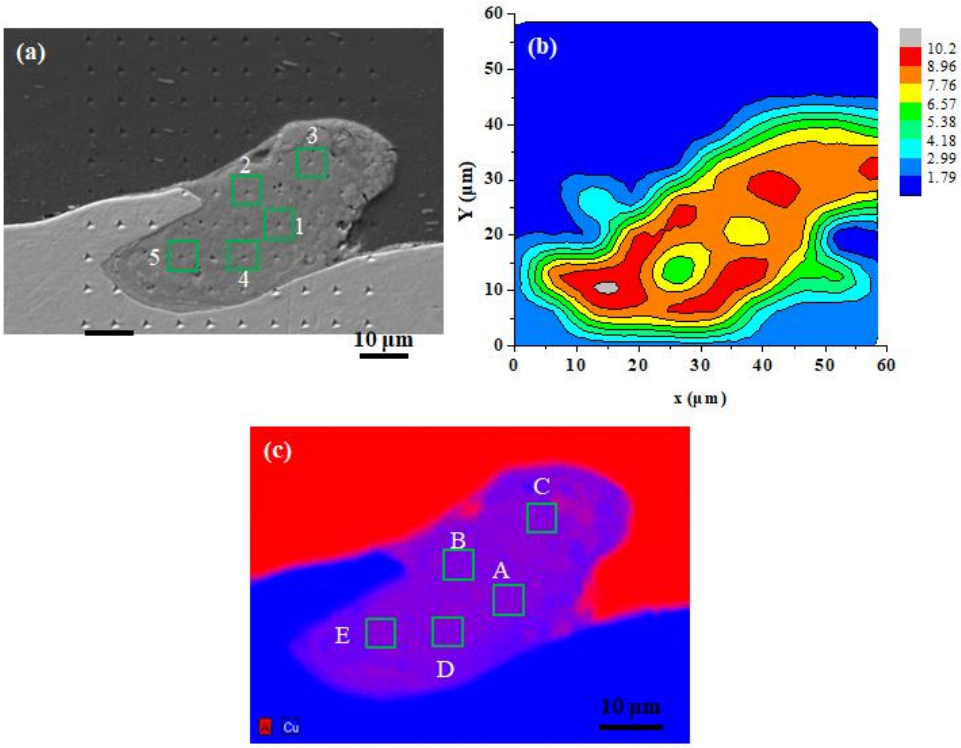

Fig. 3.13. (a) SEM image showing the arrays of indents in the test region (b) Nanohardness distribution maps (in GPa) across the array corresponding to the test regions in (a), (c) EDS map, regions A-E corresponding to indents 1-5 in (a), respectively.

It is worth noting that the values of the nanohardness in the IM layer are much heterogeneous which lie within the range of 4.79–10.14 GPa. Literatures [151,155] reported that the chemical compositions are not uniform in the melted zone in an

ultra-high impact welding interface. This suggests that the heterogeneous hardness in the IM layer maybe attribute to multiple kinds intermetallic compounds. Therefore, EDS chemical mapping was performed on the tested IM layer to verify if there are any changes in the chemical composition at the location of various indents, as shown in Fig. 3.13c. We further selected five regions (A-E marked in Fig. 3.13c) with different nanohardness to perform the EDS mapping. The EDS results of regions A-E and their corresponding nanohardness are listed in Table 3.4. The results reveal that all the selected regions in IM layers are composed with Al_2Cu. Therefore, we can conclude that the variation of nanohardness in IM layers is not due to the intermetallic compound.

Table 3.4 EDS results of region A-E (marked in Fig. 3.13c) and their corresponding nanohardness (indents 1-5 marked in Fig. 3.13a).

Region	Atomic (%)		Corresponding phase	Corresponding nanohardness (GPa)
	Al	Cu		
A	64.23	35.77	Al_2Cu	6.85
B	64.48	35.52	Al_2Cu	8.08
C	65.27	34.73	Al_2Cu	8.69
D	63.91	36.09	Al_2Cu	7.93
E	64.08	35.92	Al_2Cu	9.72

In the previous sections, we showed that the IM layers contain porous structure. Therefore, we assume that the difference of the porous density between various nanoindentation test regions maybe responsible for the variation of nanohardness. To assess this assumption, we further use the image analysis to distinguish the porous density of various test regions. The image analysis was conducted using the Image J software. Figs. 3.14 (a), (c) and (e) display the SEM observation corresponding to regions A, C and E, respectively. An image analysis post-processing was applied to these SEM images and gives in Figs. 3.14 (b), (d) and (f). The image analysis results

reveal that regions A, C and E have different porous density, i.e., 4.55%, 2.17%, and 0.88%, respectively. The combination of these values of porous density with the nanohardness values is shown in Table 3.4. We can conclude that the variations of the nanohardness are due to the different porous densities at different location in the IM layers, and nanohardness increases with decreased the porous density.

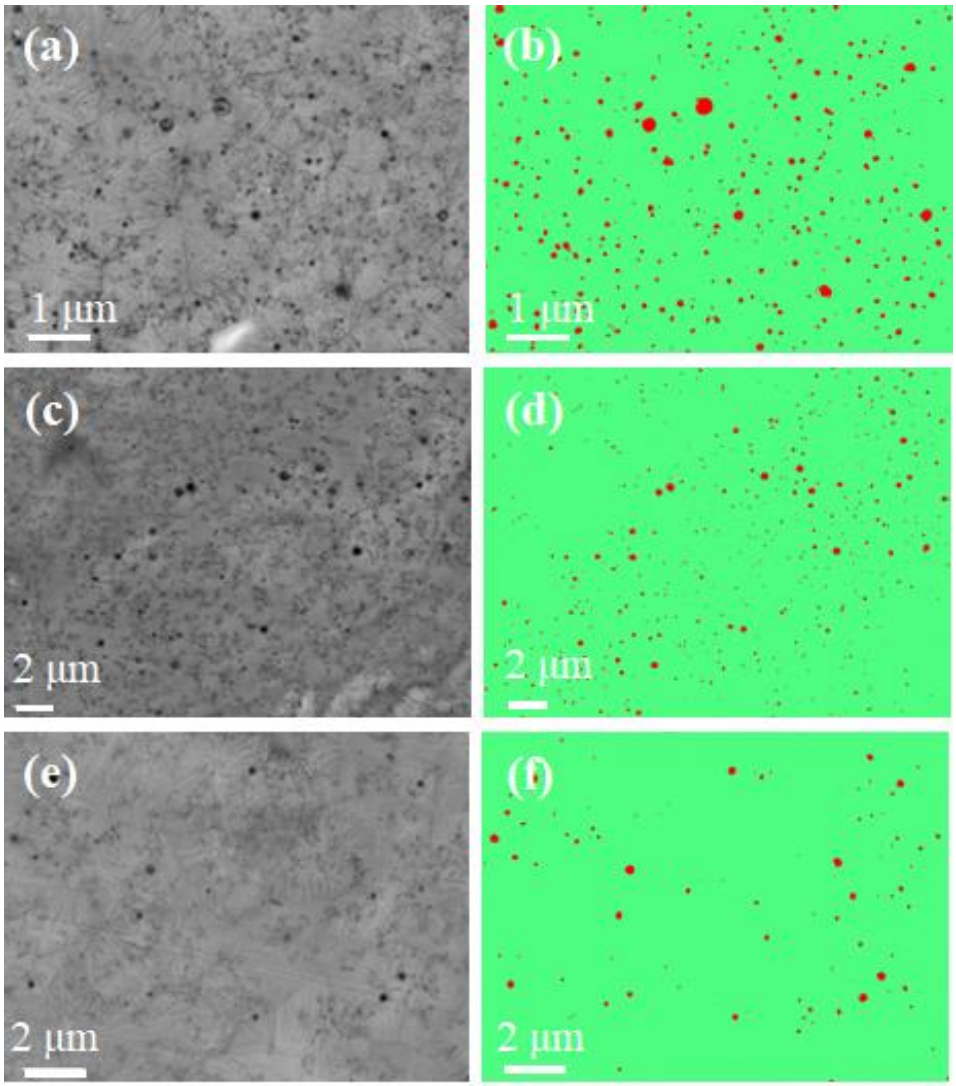

Fig. 3.14. Isolation of the porous from the IM layer by image analysis. (a), (c), (e) represent the original SEM observation, and their corresponding image analysis results in (b), (d), (f), respectively. Wherein, the red dots corresponding to pores and the green part corresponding to the IM layer matrix (i.e., Al_2Cu) in (b), (d) and (f).

Fig. 3.15 presents the P-h curves obtained from IM regions with different nanohardness. The offset of different P-h curves are 50nm from one another for the

clarity of presentation. The number and size of pop-in events in the curves decreases significantly with increased nanohardness. When the nanohardness equals 9.72 GPa, no pop-in events was observed in the P-h curve. As previously discussed, these discrete pop-in events are the serrated flow and each serration corresponds to a single shear band to accommodate the applied strain and drop of the load. Moreover, the IM layer with higher hardness exhibits larger displacement shifts. It is likely caused by the increased dislocation mobility for the most porous location [156,157]. Therefore, we can conclude that the serrated flow is more pronounced in the IM layers with high porous density.

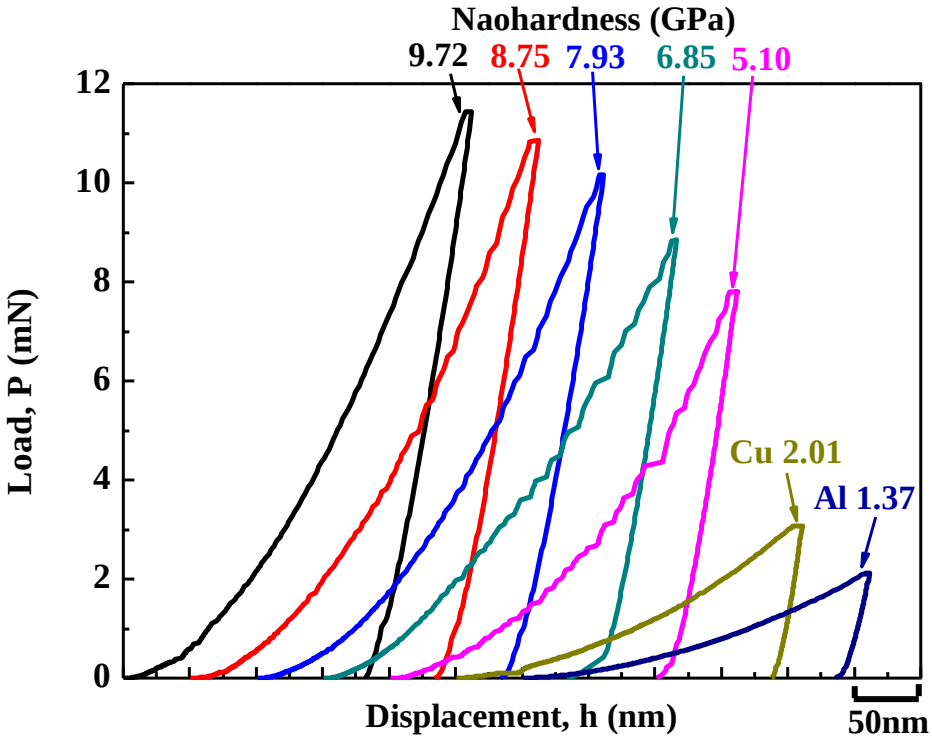

Fig. 3.15. Representative P-h curves within IM layer tested zones and base materials, offset from one another by 50nm for the clarity of presentation.

3.9 Conclusions

The effects of FS material with low (discharge voltage of 6 kV) and high (discharge voltage of 8 kV) impact intensities on the weld nature and microstructure of Al/Cu MPW welds were studied. The local mechanical behaviours at the interface were also investigated. The conclusions can be summarized as follows:

(1) FS made of steel cannot successfully produce a weld under the low impact intensity. FS made of Cuprofor, Siclanic, CuBe2 produces a successful welded joint. In the welded region, the effective welded length produced by CuBe2 FS, Siclanic FS and Cuprofor FS was 3.6 mm, 4.2 mm and 3.2 mm, respectively. When increasing the voltage to 8 kV, the weld length produced by both Steel FS and Cuprofor FS was 5.4 and 2.0 mm, respectively. For all the cases, the effective bonding always takes place few mm away from the zone where flyer impacts the fixed rod.

(2) Under low impact intensity, welding performed with CuBe2 FS and Siclanic FS produces similar features of the welded interfaces with wavy zone, swirls, cracks, discontinuous IM layers, and a few IM pockets. Cuprofor FS also generates these features, but the welded interface reveals significantly large interfacial instabilities resulting in the presence of large vortex, large holes within swirls and porous structure. Under the high impact intensity, the weld interfaces reveal much more instabilities for both Steel FS and Cuprofor FS.

(3) The efficiency of the FS under the low impact intensity increases from Cuprofor and CuBe2 to, Siclanic FS. Increasing the charging voltage is another method to obtain a good welding when using low conductive FS materials. The weld quality for the combination 8 kV and Steel FS is much better than that produced by the combination 8 kV and Cuprofor FS.

(4) IM layers are characterized by highly heterogeneous porous zone with a random size distribution. The intermetallic compound is Al_2Cu in the IM layers. An anomalous wave formation is formed with the combination of the intermediate zone and the interdiffusion zone.

(5) Nanohardness tests show that compared with base metals, the IM layers exhibited higher hardness due to the presence of intermetallic compound. The heterogeneous nanohardness in the IM layers is due to the variations of the porous density. The nanohardness decreases when the porous density increases.

(6) P-h curves results within the IM layers show “pop-in” events in the

load-displacement due to the operation of shear bands. Moreover, IM layers with high porous density exhibit larger displacement shifts due to the increased dislocation mobility. To avoid the formation of “pop-in” events which could induce residual stresses on IM layers during the nanoindentation tests, we suggest that a high strain rate test should be carried out on the IM layers.

Chapter 4

Computational modelling of MPW

4.1. Abstract

In this chapter, a coupled electromagnetic-mechanical simulation is proposed to calculate the impact velocity and impact angle along the whole interface since an in situ experimental measurement is impossible. Then, the results are used as input to thermomechanical models based on Eulerian simulation to predict the complex interface morphologies during the MPW of an Al/Cu combination. This chapter focuses on the description of the computational models including the governing equations, the test geometry, and the related mechanical behaviours.

4.2. Introduction

Impact velocity and impact angle are crucial parameters which determine the interface morphology and weld quality in impact welding [158]. To understand the physics behind MPW, Photon Doppler Velocimetry (PDV) or high-speed camera measurements are used to obtain the impact velocity. By this technique, Lueg-Althoff *et al.* [24] measured the impact velocity to analyse the radial flyer kinetics. They claimed that the welding can be achieved at low impact velocity with a low frequency pulse generator. Groche *et al.* [158] used a high-speed camera to record the collision process of aluminium assemblies with a special mechanical ring test. They identified the weldability window based on impact velocity and impact angle. However, these experimental techniques are not able to capture the complete impact velocity field and impact angle along the interface for tubular assemblies with a field-shaper.

As we discussed in Chapter 2, numerical simulations are powerful methods to investigate the complex interfacial kinematics during HSIW. The merits and limitations of existing impact welding simulations have also been extensively discussed in Chapter 2. Since the Eulerian simulation has been proven to be robust for

predicting the interfacial instabilities, this computational approach is enacted in our studies in order to investigate and compute the complex interface dynamic during the MPW of a dissimilar Al/Cu combination.

In this work, two different numerical models were used along with experimental validations and investigations of the welding tests. A flowchart given in Fig. 4.1 illustrates the modelling steps. A coupled electromagnetic mechanical (CEMM) model is put in place to determine the local impact conditions (impact angle and impact velocity) along the interface during the MPW process. Subsequently, the obtained local impact parameters are used as input data for the Eulerian (thermomechanical) computation to analyse the complex interface behaviours. This chapter provides the mathematical formulation of these coupled electromagnetic-mechanical simulations and Eulerian simulations.

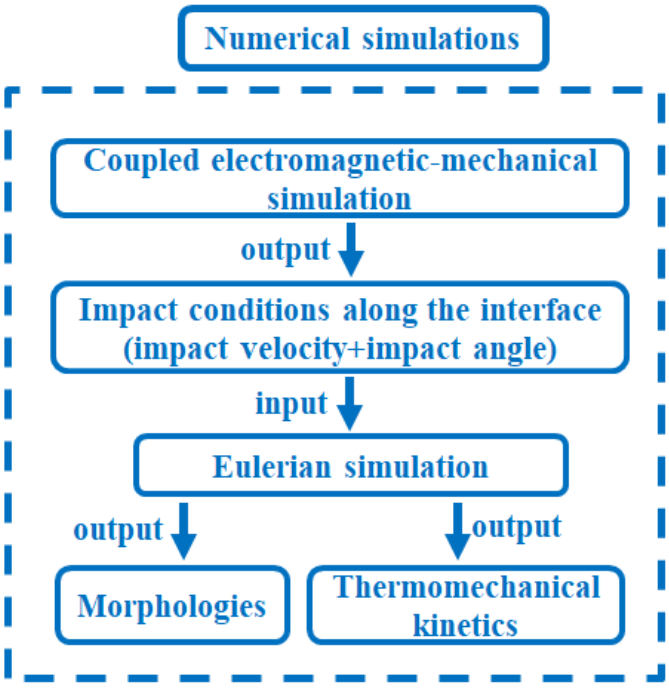

Fig. 4.1. Flowchart showing the numerical steps in this study.

4.3 Coupled electromagnetic-mechanical simulation

4.3.1 Governing equations

The electromagnetic process involves the calculation of magnetic field and eddy

current governed by the Maxwell's equations, electrical and magnetic constitutive relations, respectively given by Eqs (4.1-4.4), (4.5) and (4.6).

$$\vec{\nabla} \times \vec{E} = -\frac{\partial \vec{B}}{\partial \vec{t}} \quad (4.1)$$

$$\vec{\nabla} \times \vec{H} = \vec{J} + \varepsilon \frac{\partial \vec{E}}{\partial t} \quad (4.2)$$

$$\vec{\nabla} \cdot \vec{B} = 0 \quad (4.3)$$

$$\vec{\nabla} \cdot \vec{E} = \frac{\rho}{\varepsilon} \quad (4.4)$$

$$\vec{J} = \sigma \vec{E} + \vec{J_s} \quad (4.5)$$

$$\vec{B} = \mu \vec{H} \quad (4.6)$$

where $\vec{E}$ is the electric field, $\vec{B}$ is the magnetic field density, $\vec{H}$ is the magnetic fiel intensity, $\vec{J}$ is the total current density, ε is the electrical permittivity, ρ is the total charge density, σ is electrical conductivity, $\vec{J_s}$ is the source current density, and μ is the magnetic permeability.

During a MPW process, there is no charge accumulation and the temporal variation of the electric field is low enough to consider the following assumptions: $\rho = 0$ and $\varepsilon \frac{\partial \vec{E}}{\partial t} = 0$. Therefore, taking these two approximations into account Eqs (4.2) and (4.4), we can be rewritten as follows:

$$\vec{\nabla} \times \vec{H} = \vec{J} \quad (4.7)$$

$$\vec{\nabla} \times \vec{E} = 0 \quad (4.8)$$

On the basis of "the divergence of the curl is zero", we get the Eq (4.9) from Eq (4.7)

$$\vec{\nabla} \cdot \vec{J} = 0 \quad (4.9)$$

Thus, Eq. (4.1) and (4.3) provides the following correlations given by Eqs. (4.10)

and (4.11), respectively, due to their divergence condition.

$$\vec{E} = -\vec{\nabla}\emptyset - \frac{\partial \vec{A}}{\partial t} \qquad (4.10)$$

$$\vec{B} = \vec{\nabla} \times \vec{A} \qquad (4.11)$$

where, $\emptyset$ and $\vec{A}$ respectively represents the electric scalar potential and the magnetic vector potential. Thus, the electromagnetic problem can be solved by computing $\emptyset$ and $\vec{A}$.

As the mathematical degree of freedom is fulfilled with the magnetic vector potential $\vec{A}$, hence, a gauge equation is applicable. Then, combining the aforementioned co-relations (Eqs 4.5, 4.7 and 4.9-4.11) and the generalized Coulomb gauge condition, $\nabla(\sigma\vec{A}) = 0$, the vector and scalar potentials can be separately described by Eq. (4.12) and (4.13), respectively. By solving Eqs. (4.12) and (4.13), we can obtain the two unknowns $\vec{A}$ and $\emptyset$ in the electromagnetic system.

$$\nabla(\sigma\vec{\nabla}\emptyset) = 0 \qquad (4.12)$$

$$\sigma\frac{\partial \vec{A}}{\partial t} + \vec{\nabla} \times \left(\frac{1}{\mu}\vec{\nabla}\vec{A}\right) + \sigma\vec{\nabla}\emptyset = \vec{J_s} \qquad (4.13)$$

The Lorentz force can be directly computed by Eq. (4.14) according to the basic theory.

$$\vec{f}_{Lorentz} = \vec{B} \times \vec{J}_{eddy} \qquad (4.14)$$

where, $\vec{f}_{Lorentz}$ and $\vec{J}_{eddy}$ respectively denote Lorentz force density and eddy current density. However, this formula is not suitable for calculating Lorentz force during a MPW process since the eddy current is difficult to calculate. In our coupled electromagnetic-mechanical simulation, the Lorentz force can be estimated based on magnetic pressure calculations according to the following steps.

First, from Eqs (4.6), (4.7) and (4.14), we can describe the Lorentz force density

by Eq (4.15). Then, Eq (4.16) is obtained using vector calculus identities. Wherein, the terms $\frac{1}{\mu}(\vec{B}\cdot\vec{\nabla})\vec{B}$ and $-\frac{1}{2\mu}\vec{\nabla}(\vec{B}\cdot\vec{B})$ represents the magnetic tensile force and magnetic force, respectively. The magnetic tensile force can be ignored for the long tubes or sheet metals in the region relatively far away from the edges and the magnetic fields are always parallel to the flyer surface. Thus, magnetic pressure *P* can be simplified to Eq. (4.17).

$$\vec{f}_{Lorentz} = \frac{1}{\mu}(\vec{\nabla}\times\vec{B})\times\vec{B} \qquad (4.15)$$

$$\vec{f}_{Lorentz} = \frac{1}{\mu}(\vec{B}\cdot\vec{\nabla})\vec{B} - \frac{1}{2\mu}\vec{\nabla}(\vec{B}\cdot\vec{B}) \quad (4.16)$$

$$P = \oint_0^d -\frac{1}{2\mu}\vec{\nabla}(\vec{B}\cdot\vec{B})dx = \frac{1}{2\mu}[{B_{surf}}^2(t) - B^2(t,d)] \qquad (4.17)$$

where, d is the thickness of the flyer, B_{surf} is the surface B-field. $B(t,d)$ is considered as zero due to the extremely short duration of the MPW. Therefore, the magnetic force can be estimated using the magnetic strength between the coil and workpiece.

4.3.2 The coupled FEM/BEM procedure

The boundary element method (BEM) and finite element method (FEM) simulation were carried out using LS-DYNA version R8. The eddy current and mechanical solvers were used. In the magnetic field computing, LS-DYNA uses a coupled FEM and BEM method. The BEM method is used to calculate induced current and magnetic vector potential on the surface elements and FEM method is used for the calculation of magnetic field and induced current in the solid elements. This theory was introduced in details in [159]. LS-DYNA uses backward Euler method for the solution advancement at each electromagnetic time step. The electromagnetic and mechanical computations are thus coupled. For a good compromise between computational effort and prediction accuracy, the electromagnetic time step was set to 0.5μs with the eddy current solver. The mechanical time step was set to 1μs due to the high-speed nature of the EM process

while the thermal solver time step was set to 0.1μs. The BEM solver computes thereby the surface current and electromagnetic field instead of a complex computing of a magnetic field in the air between the coil and the flyer that requires to regenerate and remesh an air domain as the flyer tube moves due to the Lorentz force action. The BEM solver uses the Biot-Savart law to calculate the magnetic field on the surface of the workpiece, which allows ignoring the magnetic field in the air. Thus, there is no longer a need for air meshing.

In order to solve the coupled electromagnetic/mechanical problem, the material properties required by all these two modules should be defined. Physical qualities required by those fields are listed below:

1. In the electromagnetism module: electrical conductivity
2. In the mechanical module: Young's modulus, density, Poisson's ratio

The solvers are controlled automatically and follow the predefined individual time steps, boundary conditions and properties during the solution procedure. Each solver has an independent time step but the result from each solution step is coupled at each electromagnetic time step as we previously specified. The computation was performed on a parallel computer network using multiple processors (16 Xeon X7542 six-core @ 2.67 Ghz with 96 cores, 1 TB RAM) by a Shared Memory Parallel method [160,161].

4.3.3 Model description

A coupled electromagnetic-mechanical (CEMM) model was used to compute the spatial distribution of the impact velocity (V_{impact}) and the impact angle (α) along the interface during the welding process. The CEMM model uses a 3D geometry as in the experiments (as shown in Fig. 3.1a in chapter 3). The model consists of 206910 8-nodeed solid elements. The boundary conditions are described in Fig. 4.2a , where one corner point 'P' was fixed in all directions and the surface marked with ⊗ was fixed in *x* direction (direction normal to the plane) for the field-shaper. A thin polymer shock sleeve (see Fig. 4.2a) was added in the model between the field-shaper and the

coil, which can effectively avoid electrical contact and maintain the concentricity of the field-shaper. The top side of the rod and the bottom side of the tube were completely fixed in all directions. The time evolution of the input current used in the CEMM model is illustrated in Fig. 4.2b.

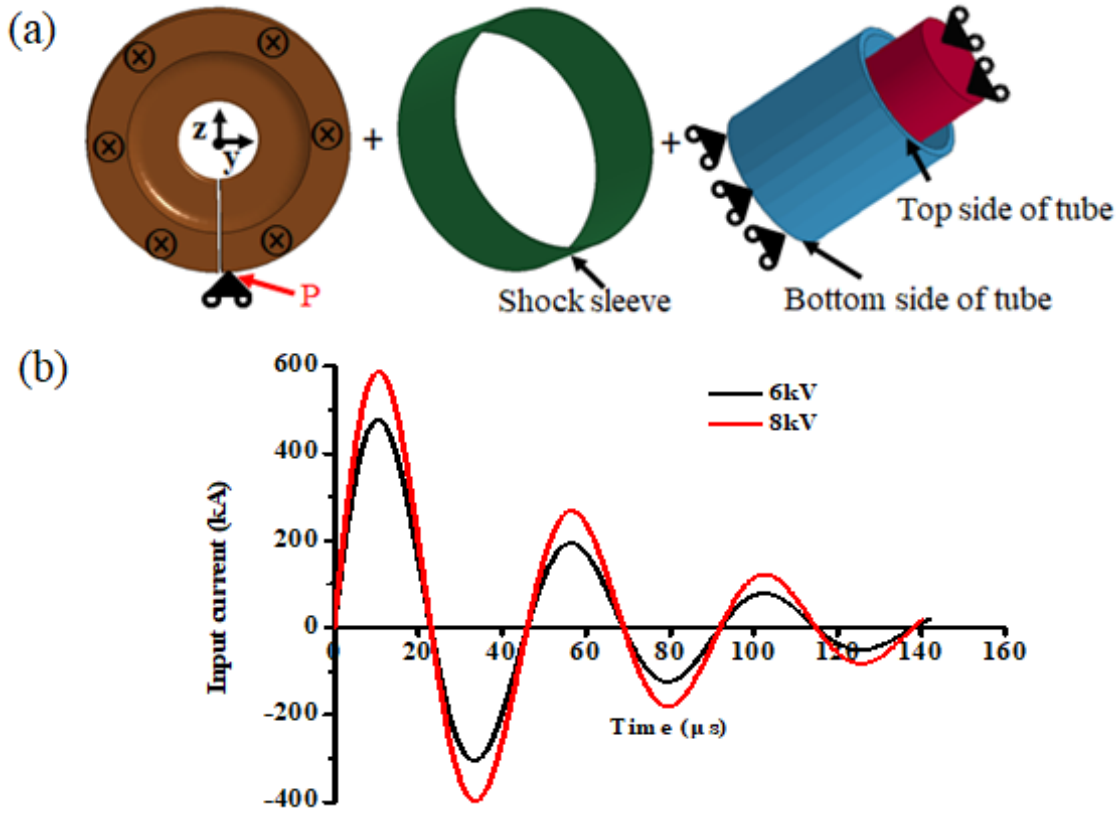

Fig. 4.2 (a) The boundary conditions, (b) input current used in the coupled electromagnetic-mechanical simulation.

The simplified Johnson-Cook model (Eq. 4.18) was used in the electromagnetic-mechanical model to describe for the strain rate dependent plasticity of the workpieces (Flyer and rod). The input data for Johnson-Cook model is given in the Table 4.1. The other parts were considered as elastic solids. Mechanical and electromagnetic properties for all the materials used in the electromagnetic simulation are summarized in Table 3.2 in chapter 3 and below in Table 4.2.

$$\sigma_y = \left[A + B\left(\varepsilon_p\right)^n\right]\left(1 + Cln\left(\frac{\dot{\varepsilon}_p}{\dot{\varepsilon}_{p0}}\right)\right) \quad (4.18)$$

where, σ_y is the yielding stress, ε_p is the effective plastic strain, $\dot{\varepsilon}_p$ is the effective

plastic strain rate, $\dot{\varepsilon}_{p0}$ is the reference strain rate. *A*, *B*, *C*, *n* and *m* are material parameters.

Table 4.1 Johnson-Cook parameters used for workpieces [162,163]

Material property	Description	Unit	Al6060-T6	Copper
A	Initial yield strength	MPa	148	89
B	Hardening coefficient	MPa	345	291
C	Strain rate constant	-	0.001	0.025
n	Strain hardening exponent	-	0.183	0.31
m	Softening exponent	-	0.895	1.09

Table 4.2: Mechanical and electromagnetic properties of materials used in the electromagnetic-mechanical simulation model

Material	Part	Density (kg/m^3)	Young's modulus (GPa)	Poisson's ratio	Electrical conductivity ($10^7 S/m$)
Al6060-T6	Flyer	2700	68	0.33	3.13
Copper	Rod	8900	124	0.33	3.48
Siclanic®	Coil	8900	130	0.29	2.67
Polymer	Sleeve	2700	13	0.29	Non

4.3.4 Impact velocity and impact angle computation

Once the accelerating hits the rod, its velocity suddenly drops (see Fig. 4.3a). Thus, V_{impact} is defined as the velocity just prior to the sudden drop, as marked by black arrows in Fig. 4.3a. V_{impact} was captured along the inside nodes of the tube and along the welding direction. α was obtained by $\tan^{-1}(V_x / V_{impact})$ at the corresponding onset time from the CEMM simulation, as illustrated in Fig. 4.3b. The position where V_{impact} and α are extracted in the CEMM model exactly corresponds to the region where the specimen was taken for the experimental observations. In this work, in order to avoid the uneven distribution of Lorentz force at the slot side (marked in Fig.3.1a in chapter 3) and its opposite side (180° to the slot), the position with a homogenous Lorentz force distribution (90° to the slot) was selected for the analysis. The detailed investigation of V_{impact} and α along the welding interface will be given in section 5.3.1 of Chapter 5.

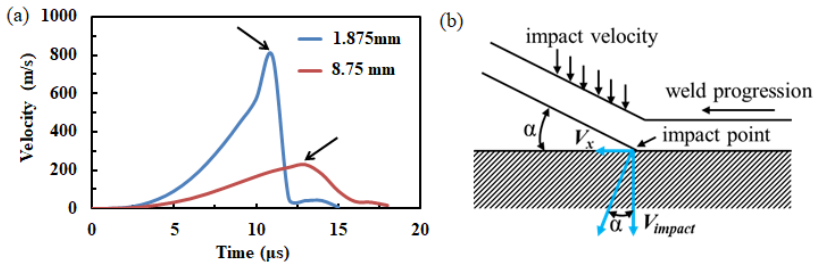

Fig. 4.3 (a) The velocity-time curves obtained from CEMM model at different locations, (b) Illustration of the angle measurement convention used in this study, where *Vx* is the collision velocity and V_{impact} is the impact velocity.

4.4. Thermomechanical models

4.4.1 Governing equations

Eulerian method describes the temporal evolution of the state variables at any point of a spatial domain with a fixed computational grid that avoids the problems of mesh distortion during the high strain-rate deformation process. The mass, momentum and energy equations are solved respectively as follows.

$$\frac{\partial \rho_0}{\partial t} + \vec{\mu} \cdot \overrightarrow{grad(\rho_0)} = -\rho div\,(\vec{\mu}) \qquad (4.19)$$

$$\frac{\partial \vec{\mu}}{\partial t} + \vec{\mu} \cdot \underline{\underline{grad\,(\vec{\mu})}} = \frac{1}{\rho_0}\overrightarrow{div\,(\underline{\sigma})} + \frac{1}{\rho_0}\vec{F_v} \qquad (4.20)$$

$$\frac{\partial e}{\partial t} + \vec{\mu} \cdot \overrightarrow{grad(e)} = \underline{\sigma} : \underline{D} \qquad (4.21)$$

where, ρ_0 is the mass density $\vec{\mu}$ is the velocity vector, $\underline{\sigma}$ is the Cauchy stress tensor, $\vec{F_v}$ is the body force, $\underline{D}$ is the strain rate tensor and e is the internal energy density which is considered to be an enthalpy to compute the dissipation of heat caused by the plastic work.

However, a pure Eulerian computation is not suitable for non-linear solid mechanics due to the high strain rate interrelated stress control the mechanical behaviour. Therefore, our thermomechanical model is based on a split Eulerian formulation which contains Lagrangian step and Eulerian step. Using the generic

formation in Eq. (4.22), each conservation equation is divided into Eqs. (4.23) and (4.24).

$$\frac{\partial \emptyset}{\partial t} + \vec{\mu} \cdot \overrightarrow{grad(\emptyset)} = f \qquad (4.22)$$

$$\frac{\partial \emptyset}{\partial t} = f \qquad (4.23)$$

$$\frac{\partial \emptyset}{\partial t} + \vec{\mu} \cdot \overrightarrow{grad(\emptyset)} = 0 \qquad (4.24)$$

The Eq. (4.16) represent the Lagrangian step, it computes the material response based on the constitutive law. The computation results are then transferred to a spatially fixed new mesh of the Eulerian step (Eq. (4.24)) based on the advection scheme and then computes the interfacial complex kinematics of the high-speed impact welding processes. The solution of Eq. (4.24) Van Leer advection scheme described as follows:

$$\emptyset_{i+1/2}^{n+1} = \overline{\emptyset_{i+1/2}^{n}} + \frac{\Delta t}{\Delta x}\left(\Phi_i - \Phi_{i+1/2}\right)$$

$$\text{with } \Phi_i = \frac{\mu_{xi}}{2}\left(\emptyset_{i-1/2}^{n+1} + \overline{\emptyset_{i+1/2}^{n}}\right) + \frac{|\mu_{xi}|}{2}\left(\emptyset_{i-1/2}^{n+1} - \overline{\emptyset_{i+1/2}^{n}}\right)$$

$$\text{and } \overline{\emptyset_{i+1/2}^{n}} = \int_{x_i}^{x_{i+1}} \emptyset_{i+1/2}^{n}(x)\, dx \qquad (4.25)$$

where, the subscript *i* represent the spatial location of the element (i.e. the ith node). *i+1/2* and *i−1/2* respectively denote the middle of the current element and upwind adjacent element. The superscripts *n* and *n+1* respectively refer the old and new values corresponding to the transport step.

4.4.2 Model description

4.4.2.1 A high-fidelity thermomechanical model for the welded zone

A high-fidelity thermomechanical model based on Eulerian formulation was constructed using ABAQUS® FE package. The Eulerian model used a 2D equivalent geometry without activating the out-of-plane degree of freedom (DOF) and has the same size as the welding tests, see Fig. 4.4a. The model consists of three sub-domains: Al flyer, Cu rod and the air gap. Appropriate boundary conditions are

prescribed for both Al flyer and Cu rod as described in Fig. 4.4b. The impact velocity obtained from the CEMM simulation was prescribed to the flyer for the Eulerian simulation.

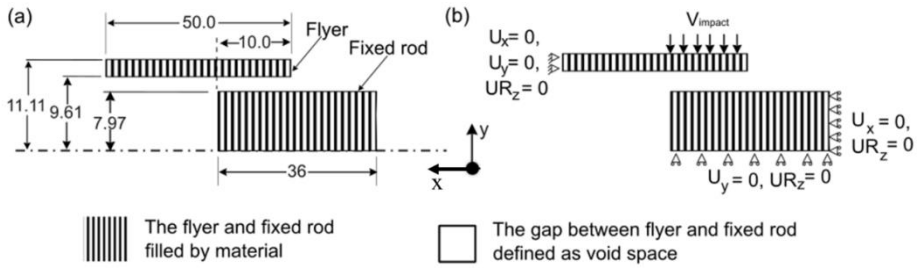

Fig. 4.4 (a) Schematic illustration showing geometrical details and (b) boundary conditions of the FE Eulerian model.

The Eulerian model was meshed with linear hexahedron, 8-noded, EC3D8R elements, and it consists of 152613 elements with 305406 nodes. To improve the simulation accuracy and to reduce the computational time, a finer mesh of 10 μm was used at the interfacial zone, while a coarser mesh was used at the zone away from the interface. The Jonson-Cook constitutive law that holds for large changes in strain, strains rate and temperature was used to capture the high strain-rate plastic behaviour during the welding [163] (given in Eq. (4.19)).

$$\sigma_y = \left[A + B\left(\varepsilon_p\right)^n\right]\left(1 + Cln\left(\frac{\dot{\varepsilon}_p}{\dot{\varepsilon}_{p0}}\right)\right)(1 - T^{*m}) \qquad (4.19)$$

where, σ_y is the yielding stress, ε_p is the effective plastic strain, $\dot{\varepsilon}_p$ is the effective plastic strain rate, $\dot{\varepsilon}_{p0}$ is the reference strain rate, and $T^* = \frac{T-T_0}{T_m-T_0}$ is the dimensionless temperature. *A, B* and *C* are material parameters, *n* is the strain hardening exponent and *m* is the softening exponent.

The Mie-Grüneisen's equation of state was used to compute the thermodynamic and pressure evolution during progressive collision. The temperature model used the energy equation considering the heat dissipation due to plastic work. Due to the extremely short period of impact process (less than 50 μs), the convective heat transfer may be neglected, and adiabatic boundary conditions were prescribed in the thermomechanical model.

The material input parameters used in the thermomechanical model were obtained from literature [162,163]. They are provided in Table 4.3. In these literature papers, the authors obtained the values of modulus of elasticity, Poisson's ratio and yield stress using uniaxial tensile test at a fixed strain rate. The true stain and stress were obtained by the Eqs. (4.20) and (4.21), respectively. Then, the stress-stain curve was used to compute the hardening coefficient *B* and strain hardening exponent *n* by using the least-squares method. The constant *C* and *m* are determined from Split-Hopkinson bar tests [164].

$$\bar{\varepsilon}^{pl} = 2\ln(\frac{d_0}{d}) \qquad (4.20)$$

$$\frac{\bar{\sigma}_x}{\bar{\sigma}} = \left(1 + \frac{2R}{a}\right)\ln(1 + \frac{a}{2R}) \qquad (4.21)$$

Table 4.3: Material properties used in the thermo-mechanical model [162,163]

Material property	Description	Unit	Al6060-T6	Copper
A	Initial yield strength	MPa	148	89
B	Hardening coefficient	MPa	345	291
C	Strain rate constant	-	0.001	0.025
n	Strain hardening exponent	-	0.183	0.31
m	Softening exponent	-	0.895	1.09
T_o	Reference temperature	K	298	298
T_m	Melting temperature	K	916	1356
s	Slope of linear Rankine–Hugoniot's law	-	1.37	1.49
γ0	Mie-Grüneisen's coefficient	-	2.14	2.02
G	Shear modulus	GPa	26.2	46.3
ρ_1	Reference mass density	Kg/m^3	2700	8900
Cp	Specific heat capacity	J/(Kg K)	900	385
λ	Thermal conductivity	W/(m K)	237	387

This model is able to predict the evolution of the various types wave at the interface, as shown in Fig. 4.5. Moreover, it can compute the effective plastic strain, the history of thermomechanical kinetics, shear instability, collision pressure and collision velocity during wave formation. These phenomena can help to understand the fundamental mechanism and thermomechanical kinetics during the wave formation. Detailed information will be given in Chapter 5.

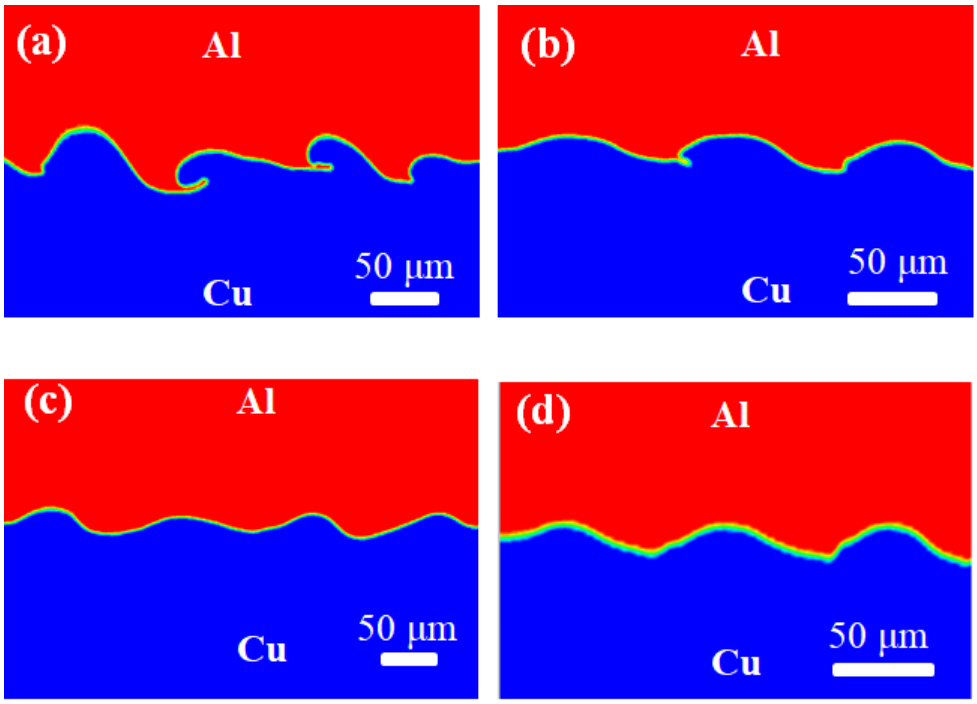

Fig. 4.5 Various wave morphologies obtained from the numerical simulations

4.4.2.2 Local thermomechanical model for the impact zone

To capture the collision details, a local thermomechanical model using 2D equivalent geometries (without activating the out-of-plane degree of freedom) and the appropriate boundary conditions, illustrated in Fig. 4.6 is used. The flyer thickness is set to *1.5 mm*. The Eulerian domain is meshed with 8-nodeed, multi-material, thermally coupled EC3D8RT (hexahedral) elements. The interfacial zone is meshed using structured mesh with the mesh size of 1 μm along the interface. A total of 254513 elements were used. The predicted characteristic variations of the interface obtained from thermomechanical model are further analysed to understand the

fundamental mechanism and transient thermomechanical behaviour of the interface during the development of complex kinematics under the high-strain rate collision.

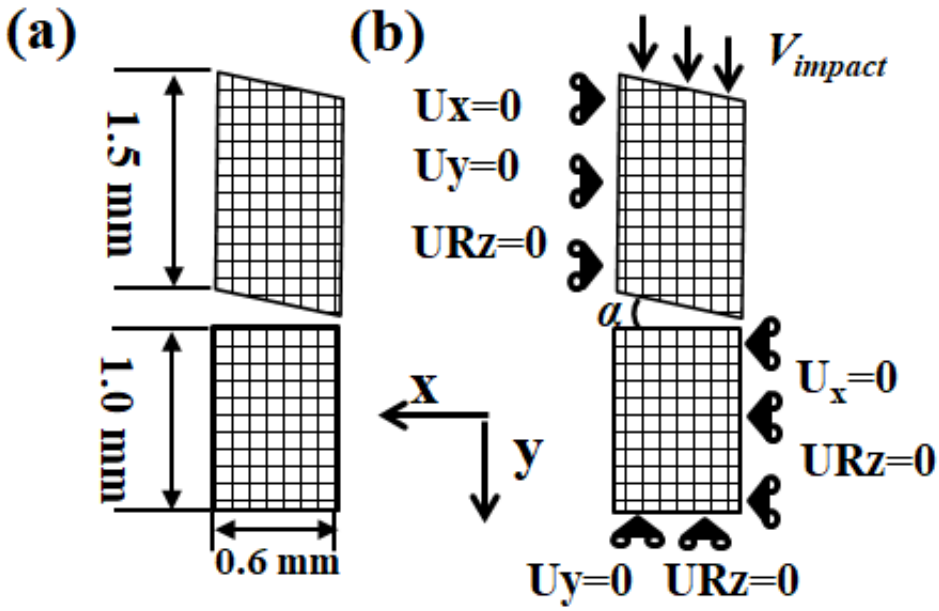

Fig. 4.6 (a) model geometry and (b) boundary conditions.

This model allows computing the experimentally observed complex interface morphologies, such as wake, vortex, swirl and mesoscale cavities, as shown in Fig. 4.7. History of temperature, pressure and velocity can also be plotted during these complex morphologies formation. These will be further studied in Chapter 6. Moreover, it allows us to build a weldability which will be discussed in Chapter 7.

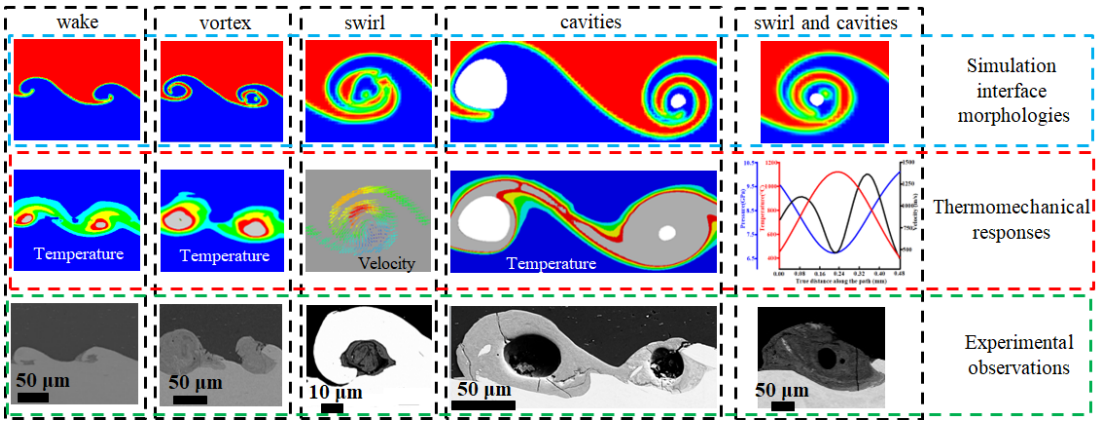

Fig. 4.7 Complex interface morphologies and thermomechanical responses obtained from the numerical simulations, and the experimental observations of the interface morphologies.

4.5. Conclusions

This chapter is mainly focused on the three computational models of MPW. The theoretical background, the geometry and the boundary conditions of the three models are described. The links and interrelations between the three models are summarized as follows:

(1): A coupled electromagnetic-mechanical model (CEMM): As discussed in Chapter 2 and Chapter 3, impact velocity and impact angle significantly influence the interface morphologies. However, these parameters are difficult to capture using experimental methods especially for the MPW tubular assemblies with a field-shaper. Moreover, with in-situ method it is impossible to obtain the complete impact velocity field and impact angle along the interface. Therefore, a CEMM is proposed to predict the local impact conditions at the macroscopic scale. The obtained impact parameters are used to understand the physics behind the formation of various interface characteristics. This will be discussed in Chapter 5.

The CEMM model can somehow analyse the impact kinematics and impact conditions at microscope scale. However, this model cannot predict the interface morphologies. Based on our study of the literature in Chapter 2, Eulerian simulations are very suitable to investigate the interface material responses of MPW. Therefore, two thermomechanical models based on Eulerian formulation are further proposed to investigate the multi-physics and transient response of the interface at microscopic scale. They are summarized below:

(2) A high-fidelity thermomechanical model for the welded zone: This model uses the obtained impact velocity from CEMM model as input parameters. It is used to investigate the welded zone, i.e., various types of wave formation. Their formation mechanisms will be reported in Chapter 5. The complex interface morphologies, such as wake, vortex and cavities, required finer mesh size in the simulation. Therefore, taking computational effort and prediction accuracy into consideration, a local thermomechanical model for the impact zone is further proposed.

(3) Local thermomechanical model for the impact zone: This model considers the specific location impact conditions (impact velocity and impact angle) extracted from the CEMM model. It is used to investigate the complex interface dynamic phenomena that will be discussed in Chapter 6. It will also be used to build a weldability window described in Chapter 7.

Chapter 5

Computational investigation of various welds formation during the MPW of Al to Cu

This chapter has been drawn up by recasting two peer reviewed papers:

1. J.S. Li, R.N. Raoelison, T. Sapanathan, Z. Zhang, X. G. Chen, D. Marceau, Y.L. Hou, M.Rachik, An anomalous wave formation at the Al/Cu interface during magnetic pulse welding. Applied Physics letters, 116 (2020), 161601. https://doi.org/10.1063/5.0005299

2. J.S. Li, T. Sapanathan, R.N. Raoelison, Y.L. Hou, A. Simar, M. Rachik, On the complete interface development for Al/Cu magnetic pulse welding via experimental characterizations and multiphysics numerical simulations, Journal of Materials Processing Technlogy. 296 (2021), 117185. https://doi.org/10.1016/j.jmatprotec.2021.117185 "

5.1. Abstract

This chapter investigates the formation of four types of waves (case of (CuBe2, 6kV) Al/Cu MPW interface presented in chapter 3) using numerical simulations to elucidate the experimental interface morphologies, i.e., the unwelded zone, the vortex + intermediate (IM) layers and the wavy interface. The CEMM model provides the dynamic impact angle and velocity we considered for the Eulerian simulation of interfacial phenomena. The wave is formed with repeated deformation of the interface material. Particularly, the interface kinematics of an anomalous wave formation is investigated. The intermediate zone is caused by a local melting due to the high shear instability. The multiphysics simulation has put in evidence the link between jetting kinematics, non-uniform distribution of shear strains during high-speed collision and the formation of the anomalous wave. A statistical analysis show that the wave

amplitude increases with the jetting angle and the wavelength increases with the collision velocity. The ratio between collision velocity and impact velocity is found to be the most suitable parameter for explaining the influence of the collision on the wavelength.

5.2. Introduction

In MPW, the wavy morphology of welded interfaces is a distinctive feature which is believed to create a permanent bonding promote with an improved joint strength [80,82]. Over the past few decades, numerous research studies were carried out to better understand the wave formation mechanism in terms of morphology, microstructure and formation kinematics during impact welding. Both Geng *et al.* [74] and Yu *et al.* [73] observed an amorphous layer within the wavy interface using transmission electron microscopy (TEM) observations. This thin layer is due to a melting [74] or a solid-state formation [73]. Cui *et al.* [101] used an analytical model to predict the wave formation. A wave with the peak height equals to the width of the transition zone is generated by the shear instability with an impact angle of 4°.

Recently, numerical simulations were massively used to explain the wave formation kinematics. The data provided by numerical simulation may not be obtained by in-situ experimental methods due to the high speed impact process. Bataev *et al.* [103] pointed out that the wave formation is due to the sequential indentation of protrusions formed on opposite sides of the welding workpieces. However, Lee *et al.* [109] stated that the wave morphology results from internal stresses during collision. Effects on wavy morphologies (i.e., wavelength and amplitude) with respect to the collision parameters have also been reported in previous works. Wang *et al.* [115] claimed that the wavelength increases with decreased collision velocity, and the amplitude increases with increased jetting velocity. However, the analytical formula combined with the experimental work of Watanabe and Kumai [60] showed that wavelength increases with the collision velocity. Moreover, Lee *et al.* [109] suggested that the impact velocity should dictate

the wave amplitude.

In [27], regular type wave formation for an Al/Al similar welding interface was predicted using an Eulerian simulation with a uniform impact velocity. For MPW of dissimilar materials, the interface behaviours are more complex due to the mismatch of strain hardening and coefficients of thermal expansion, which is prone to produce complex interface morphologies.

Some fundamental aspects of the wave formation steps for dissimilar interface need further investigation since there was no attention given to the physical phenomena and kinematics of various types of waves including irregular waves. Understanding the conditions required to produce various types of waves are essential. In this chapter, we firstly use the CEMM model (see section 4.3 in chapter 4) to determine the impact angle (α) and the impact velocity (V_{impact}) along the interface during the MPW process. Based on the CEMM model, various welding zones will be identified and correlated to various interface characteristics. Subsequently, the obtained local impact parameters were prescribed as input parameters of the thermomechanical Eulerian model (see section 4.4.2.1 in chapter 4). The analysis of results makes it possible to understand the fundamental mechanism and transient thermomechanical behaviours of the various types of waves.

5.3. Results and discussion

5.3.1 Impact kinematics along the interface

The changes of the impact velocities during the welding progression can create various interface features for a given weld. Thus, the investigation of V_{impact} and α along the welding interface is required to understand the physics behind the formation of various interface characteristics during MPW.

Fig. 5.1a presents velocity and angle along the interface obtained from the CEMM simulation. The distance (8.1 mm) finishing the black solid line in Fig. 5.1a indicates the regions where the Al flyer collided with the Cu rod during the

simulation. The maximum velocity (V_{max}) and the simultaneously reached angle (β) given by the extended blue dashed line does not produce an impact of the flyer with the inner rod. From the CEMM simulation, we can clearly distinguish the non-impacted zone which does not have either a change in velocity direction or sharp drop in velocity magnitude. To differentiate them from V_{impact}, this velocity (without an impact of the flyer with the inner rod) is called V_{max}. The corresponding β angle, for the non-impacted part of the weld is defined by $\tan^{-1}(V_x / V_{max})$ in chapter 4 (the definition of V_x see Fig. 4.3b in chapter 4).

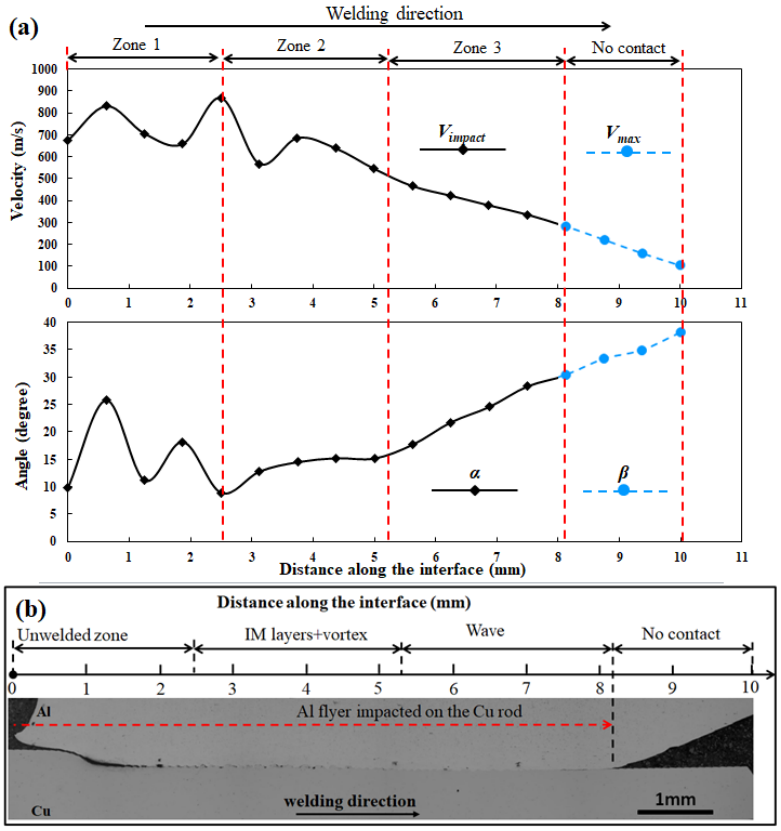

Fig. 5.1. (a) velocity and angle along the interface obtained from the coupled electromagnetic-mechanical simulation. The solid black lines portions of the curves (distance ≤ 8.1 mm) correspond to the impact velocity of the flyer, which impacted the inner rod. Beyond the distance 8.1 mm, the curves are extended by blue dashed lines to indicate that the flyer did not come in contact with the inner rod. (b) cross-sectional micrograph of MPW weld of the case of (CuBe2, 6kV), wherein, unwelded zone at the onset of welding, IM layers+vortex zone, wavy interface corresponding to Zone 1, Zone 2, and Zone 3 in Fig. 5.1a, respectively.

The curves indicate that V_{impact} and α significantly fluctuate during the MPW process as the welding proceeds. This fluctuation occurs due to the heterogeneous distribution of the Lorentz force and other mechanical constrains (e.g. relative location of a particular collision point). It is worth noting that the highest velocity appears below the top side of the flyer tube and slightly above the horizontal mid-plane of the field-shaper (see Figs. 3.1a and c in chapter 3). The impact region can be further classified into Zone 1, Zone 2 and Zone 3, based on the characteristics of the combination of V_{impact} and α, as marked in Fig. 5.1a. At the onset of Zone 1, V_{impact} and α fluctuate significantly that may not be favourable for a welding. After that, in Zone 2, V_{impact} starts to slightly decrease while α is rather stable, that is expected to produce a higher shearing instability at the interface. In Zone 3, V_{impact} gradually decreases in conjunction with the gradual increase of α, that is expected to produce a less chaotic behaviour of the interface instability. The variations in V_{impact} and α are expected to produce different interface features. Therefore, the corresponding classified interface zones of the experimental sample are further characterized to understand the consequence of the impact parameters on the interface behaviours observed in Fig.5.1b.

Fig. 5.1b shows the cross section of MPW weld of the case of (CuBe2, 6kV), revealing different interface morphologies along the welding direction (from left to right) corresponding to the different impact conditions (in Fig. 5.1a). They include (1) unwelded zone at the onset of the weld; (2) formation of vortices + IM layers along the interface; and (3) various wave morphologies (with different amplitudes and wavelengths). The detailed features in each zone were already discussed in Chapter 3. At the onset of welding, the impact conditions correspond to Zone 1 in Fig. 5.1a. The higher V_{impact} with large fluctuation leads to a shock-like behaviour, and thus the interface does not form a jet immediately. Cuq-Lelandais *et al.* [165] showed that the reflected wave produces a tensile state at the collision point, enabling to peel off the interface and to form unwelded zone, even though the impact conditions meet the welding criterion. Psyk *et al.* [144] confirmed this effect by numerical simulation of a

sheet welding process. The flyer edge hits the target and is subsequently lifted.

As welding proceeds (impact conditions corresponding to Zone 2 in Fig.5.1a), jetting phenomenon initiates due to a severe interface shearing. This subsequently generates a strongly confined heating which enables to melt the metals at the interface and to form the IM layers. Then, the interface instability decreases (Fig.5.1a). In Zone 3, the impact energy is insufficient to melt the base metals; and thus, it forms the wavy interface with a discontinuous thin IM layer or may even result in a complete absence of IM layer. One may note that at the end of our welding, no contact zone is observed at the interface of the experimental test (see Fig.5.1b). This no contact zone is well predicted by the numerical simulation as shown in Fig.5.1a (indicated by the blue dashed line).

5.3.2 Numerical predictions of the wave formation

The impact velocity from the CEMM model is used to investigate the wave formation with the help of an Eulerian simulation. The investigation is limited to Zone 3. For convenience, the spatial evolution of impact velocity in this zone is interpolated using a linear function:

$$\left|V_{impact}\right| = -300 - 70000x; \qquad \forall x \in [0, 0.0026] \tag{5.1}$$

where, V_{impact} is the impact velocity (Unit: m/s), and x is the distance from the end to the onset of the wave formation (Unit: m).

Before discussing the results from the Eulerian simulations, it should be noticed that the results in such simulation can be calculated for each individual material and it can also averaged over the each finite element. The averaged values are weighted by each material volume fraction. As we focus on the investigation of the interface dynamic phenomena, the presented results are averaged quantities unless otherwise specified.

The images in Figs. 5.2a-d show various wave morphologies obtained from the Eulerian simulation limited to Zone 3 of Fig. 5.1a and b. The simulation results

corroborate the experimental observations in the case of (CuBe2, 6kV) as shown in Figs. 5.2i-l, in terms of shape, size and sequential development of wave morphologies. Analogously, the flat interface of an anomalous wave (Fig. 5.2i) which spreads over a length of approximately 87 µm, is well predicted by the simulation (3rd wave marked in Fig. 5.2a). This proves that the thermomechanical model is a reliable tool to further analyse the mechanisms formation of the wave.

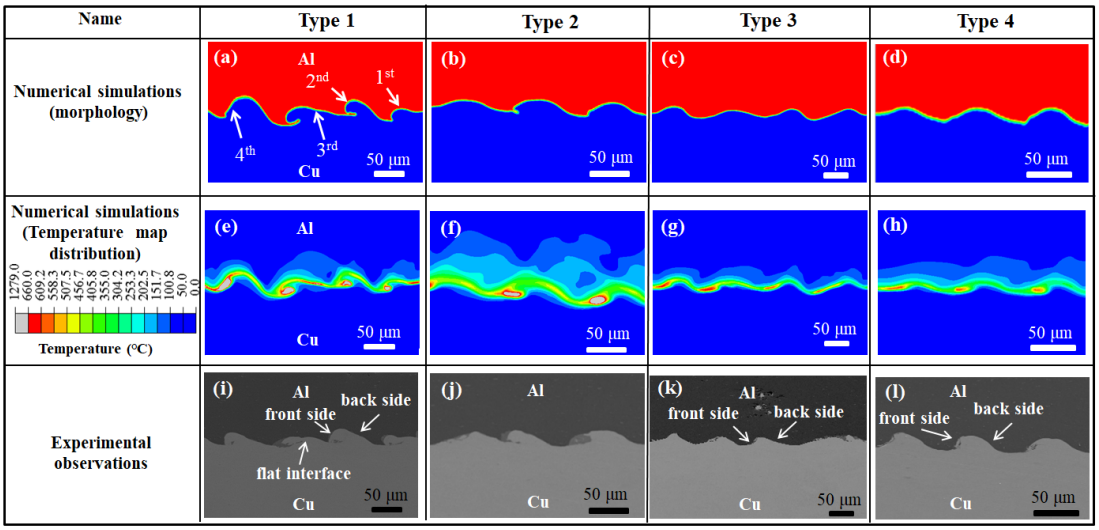

Fig. 5.2. Various wave morphologies obtained from the numerical simulations (a-d), corresponding temperature distributions (e-h) and the experimental observations of the waves (i-l).

The simulation also enables to investigate the temperature distribution along the wave interface (Figs. 5.2e-h) which is impossible to measure by *insitu* methods due to the high-speed transient welding process. The melting point of Al (~660 °C) is set to the limit temperature for the contours. The temperature distribution maps show a narrow band with a significant excessive heating along the wavy pattern at all locations due to the confined plastic deformation. The localized grey pockets shown in (Figs. 5.2e and f) indicate that the temperature is higher than 660 °C, and even up to 1279 °C, that exceeds the melting point of Cu (~ 1085 °C). Those thermally affected zones are in good agreement with the IM phases revealed by the experimental observation (in terms of shape and site occurrence), and it indicates that a possible local melting facilitates the formation of IM phases (Figs. 5.2i and j). In contrast, the predicted distributions of temperature corresponding to the Type 3 and 4

waves shown in (Figs. 5.2g and h), are below the melting point of both Al and Cu. It also concurs with the experimentally observed waves without IM phases at the interface. Based on these observations, we could conclude that the wavy interfaces experience two bonding mechanisms, (i) a mixture of local melting and solid-state bonding (for Type 1 and 2) and (ii) a solid-state bonding alone (for Type 3 and 4). These bonding mechanisms have also been reported in a recent work [166] for dissimilar MPW of sheet metals using experimental observations.

5.3.3 Averaged equivalent plastic strain at the interface

The contour plot of averaged equivalent plastic strain obtained from the Eulerian simulation is shown in Fig.5.3. They are computed as a volume average of equivalent plastic strain over all materials present in the element. The result reveals a confined plastic deformation along the interface in all types of waves. It corroborates the temperature rise of the interface (Figs. 5.2e-h). The plastic strain distribution clearly indicates the higher plastic values at the vicinity of the interface, while the plastic strain rapidly decreases to zero within the region near the base metals. Moreover, the regions corresponding to higher strain values are also in good agreement with the IM phase formation (see Fig. 5.2i and j).

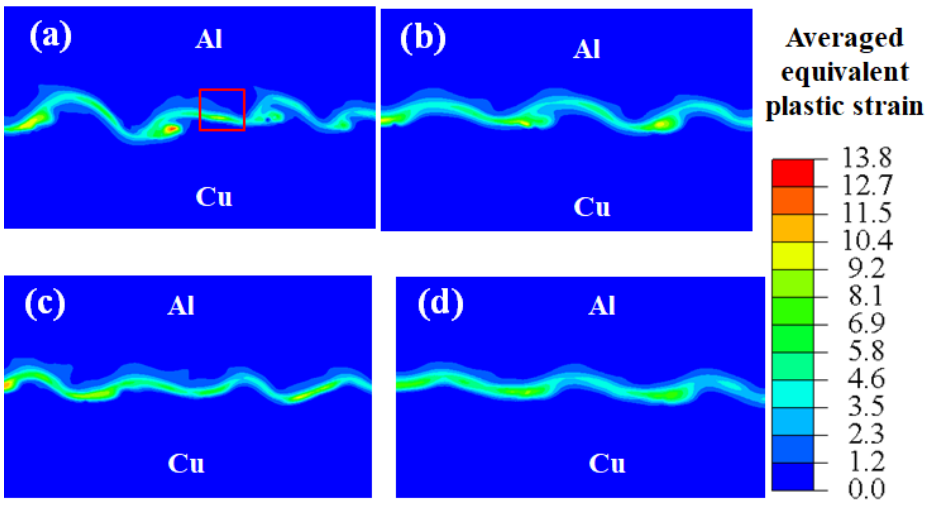

Fig. 5.3. (a), (b), (c) and (d) represent the simulation results of the averaged equivalent plastic strain distribution at the wavy interface for the wave Type 1, 2, 3 and 4, respectively.

Based on these findings, the averaged equivalent plastic strain could also be a criterion for predicting the formation of wavy interface with or without the IM phase. For specific material combinations, the plastic strain can be used to inversely predict the impact conditions which further enable to identify the process parameters. To establish a welding window based on the plastic strain criterion, it requires multiple simulations and inverse analysis of the local strain to identify the corresponding process parameter.

A magnified plastic strain image of wave Type 1 (marked by red rectangle in Fig. 5.3a) illustrates the position of points 1-4 corresponding to the Al flyer, and the positions of points 5-8 corresponding to the Cu rod near the interface (Fig. 5.4a). These points were chosen to plot the temporal evolution of the averaged equivalent plastic strain, as shown in (Figs. 5.4b and c) for Al and Cu sides, respectively. t=0 denotes the beginning of the flyer impact onto the inner rod. As the weld propagates to the selected regions, the plastic strain starts to substantially increase. The point of initial plastic strain rise occurs at t=3.4 μs (Figs. 5.4b and c). Then, the plastic strain evolves until the impact passes the selected region. Therefore, a region marked by the shaded orange color in (Figs. 5.4b and c) has been added to highlight the temporal plastic strain evolution during the wave formation. The results show that all the points on the flyer side (points 1-4) experience a rise in plastic strain, and then the strain levels drop to specific values which remain at the interface (Fig. 5.4b). However, all the plastic strain curves on the Cu rod (points 5-8) show that the strain values increase to the maximum (Fig. 5.4c). At the end of the plastic strain curves, the strain value did not drop down to zero, it means some residual plastic strain still remains inside the material after the wave formation. To further examine this difference, we also investigate the averaged equivalent plastic strain for a reference Al/Al interface as shown in (Fig. 5.4 d). A similar trend is also observed for the strain curves of the Al/Cu interface (Fig. 5.4e and Fig. 5.4f corresponding to the Al flyer and Al rod, respectively). This result confirms that the “peak” values in the strain curves on the flyer side (Fig. 5.4b) are not due to the different flow behaviors between Al and Cu.

Instead, it is attributed to the formation of waves resulting from the repeated deformation instead of immediately being formed after the first onset of impact.

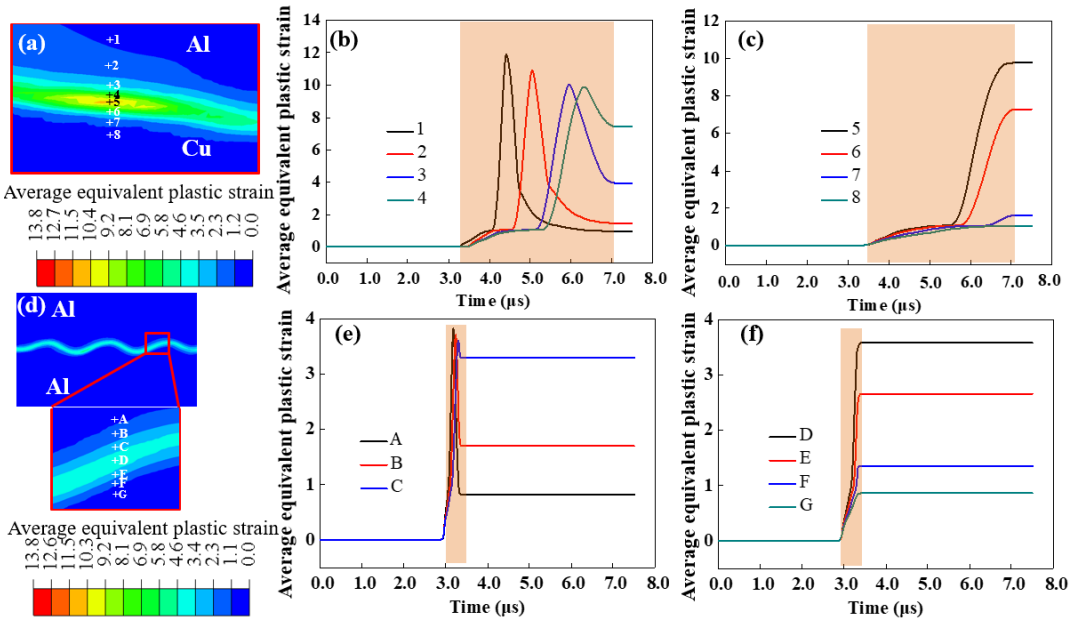

Fig.5.4 (a) A magnified averaged equivalent plastic strain map of the area marked by red rectangle in wave Type 1 in Fig. 5.3a; changes of averaged equivalent plastic strain over time at points on the (b) flyer side and (c) rod side near the interface marked in (a); (d) averaged equivalent plastic strain map obtained from an Al/Al interface with the same impact conditions; changes of averaged equivalent plastic strain over time at points for (e) the Al flyer and (f) the Al rod at an Al/Al interface marked in (d). The regions highlighted by orange color in Figs. 5.4b, c, e and f represent the plastic strain evolution during the wave formation.

5.3.4 History of thermomechanical kinetics during wave formation

The predicted temperature and deformation histories of the interface are depicted in Fig. 5.5a to further understand the thermo-mechanical conditions that facilitate the interface diffusion and the AP formation (see Fig. 3.9 in chapter 3) in wave type 1. Temperature and pressure curves shown in Fig. 5.5a are obtained from the point ① indicated in (Fig. 5.5c) corresponds to the TEM sample location (marked by red rectangle in Fig. 3.9 in chapter 3). Upon the collision process, the wave interface experiences a rapid temperature rise with an ultrahigh heating rate of ~10^{14} °Cs^{-1}. Then, the temperature continues to increase up to 643 °C while the pressure reaches a

maximum value of 6.5 GPa. The temperature of point ① does not exceed the melting point of Al and it indicates that the amorphization process observed in (Fig. 3.9) is a solid-state transformation. The rise of the impact pressure induces the increase of the plastic strain at the interface and it experiences an accommodation with the help of structural defects, resulting from the relatively high free surface energy. That is, as the strain exceeds a critical value, the crystal structure could collapse and transform to a crystalline-amorphous interface to reduce the surface free energy [73]. The propagation of the crystalline-amorphous interface requires atomic mobility, which is promoted by the heat generation combined with the severe plastic deformation during the high-pressure impact. The cooling rate obtained from the Eulerian simulation (Fig. 5.5d) also indicates that the cooling rate (~10^{13} °C s^{-1}) provided the favourable condition for the formation of amorphous layer. Although the temperature prediction point is chosen to match with the TEM sample location, there is a high probability for small deviations as the TEM samples are taken from a very small region. However, the surrounding zone of point ① reveals cooling rates higher than the critical cooling rate of amorphization for aluminium liquid (10^9 Ks^{-1}) reported in literature (see for e.g. [74]). Based on these observations, the anomalous wave interface is mainly formed due to two bonding mechanisms, i.e., local melting of Al at those locations with the temperature above 660 °C and solid-state bonding elsewhere.

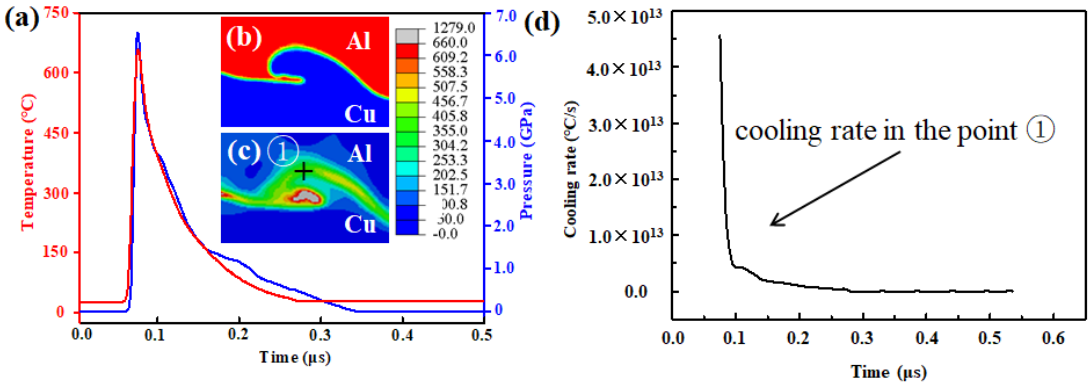

Fig. 5.5. (a) The time-dependent temperature and pressure obtained from point ① (marked in inset c) in the wave morphology, (b) and (c) the temperature field map and the colour legend corresponding to the temperature in °C. (d) The cooing rate obtained from point ① in (e).

5.3.5 Development of kinematics of the wavy interface

From a thermodynamic point of view, the metallurgical changes occurring at the interface reveal non-equilibrium conditions, thus a complex kinematics would have happened as the wave propagates. Therefore, we selected an anomalous wave (type 1) to investigate its detailed formation process illustrated in Fig. 5.6. During the oblique collision, the strong interfacial shear instability arises from a tangential velocity, which produces the upward jetting (Figs. 5.6a and b). Then, the upward jetting interacts with an earlier protrusion emerging from the inner rod. Moreover, the flyer subjected to the impact velocity impinges onto the inner rod. The above two phenomena result in the downward jetting (Figs. 5.6c and d). These upward and downward jetting produce the sequence of inverted curves along the interface and form a regular wavy pattern at the onset of collision (Figs. 5.6a-d).

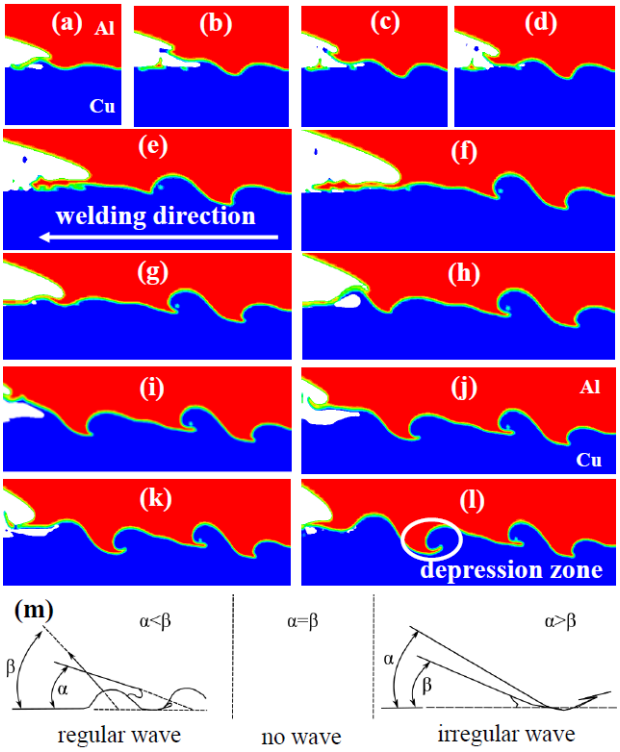

Fig. 5.6. Sequential development of anomalous wave (type 1) obtained from the Eulerian simulation: (a-d) onset of regular wave and (e-f) propagation of the flat wave and the first two waves; (g-l) development of subsequent waves, (m) schematic illustration showing the interaction angles α and β during the interface wave development.

The simulation also provides an excellent description of the development of the flat interface morphology (Figs. 5.6e-f). In this case, the interaction angles of α and β (see Fig. 5.6m) are equal, thus the condition results in an unfavourable plastic deformation for the wave formation [167], and jetting always propagates parallel to the interface. Synchronously, the former regular waves continue to grow due to the increase of shear instability at their front and back sides, and eventually form the first two anomalous waves with the irregular morphology. As the collision progresses along with the increase of both deformation of materials and shear instability, the depression zone becomes larger and squeezed. In comparison with the former waves, the impact condition makes α higher than β, and it promotes the irregular shape formation (Figs. 5.6i-l). These flat and irregular waves together constitute the anomalous waves (type 1) as shown in (Figs. 5.2a and i).

5.3.6 Shear instability of the wave formation

The wave development kinematics is highly related to the shear instability of the interface. Hence, the temporal and spatial variations of the interfacial shear strain development during the collision are further investigated to understand their contribution to the formation of the Type 1 wave. A contour plot of the shear strain around the Type 1 wave is shown in (Fig. 5.7a). It reveals that the shear strain direction is changing on short distance at the front side and back side of each wave. The alternating positive and negative shear strain patterns are influenced by the inversion of the jetting from upward to downward directions (Figs. 5.6a-l). Fig. 5.7b presents the time-dependent variations of the positive and negative shear strains at the 2^{nd} wave. The positive and negative shear strains have the same increasing trend, while the maximum negative shear strain (~2.05) is much higher than that of positive shear strain (~1.60). This indicates that Al side (i.e. compressive strain side) experiences much higher plastic deformation than Cu side.

The maximum positive and negative shear strains of each wave are examined to clearly explore the relationship between the shear strain and wave pattern, plotted in

(Fig. 5.7c). The negative shear strains of the 1st and 3rd waves are relatively smaller than their positive shear strains, and it also explains the appearance of the flat interface in the back side of these waves (Figs. 5.2a and i). Large positive shear strain is also observed in the front side of the 3rd wave providing the interpretation of the emergence of IM zone at the bimetallic interface.

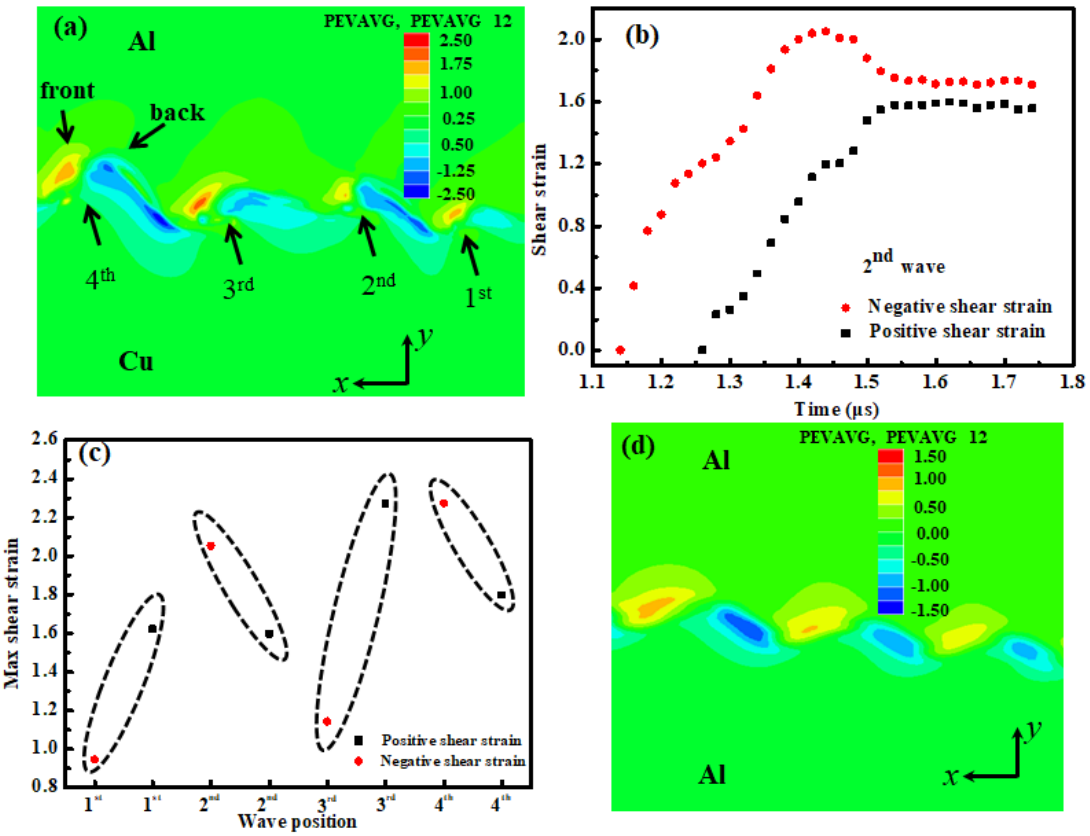

Fig. 5.7. (a) The predicted shear strain distribution along the Al/Cu interface obtained for the anomalous wave type 1; (b) time-dependent variations of shear strain for the 2nd wave; (c) the maximum positive and negative shear strains of each wave; (d) predicted shear strain distribution along an Al/Al interface with the same welding parameters, which resulting to form regular wave.

To further understand the influence of the shear strain on the wave formation, the same input velocity was used to simulate the welding process of an Al/Al interface. A regular wave morphology was obtained. The corresponding shear strain map of the Al/Al interface is depicted in (Fig. 5.7d). It can be noticed that the negative shear strains exhibit a higher value and are distributed across a larger area compared with

the positive shear strains for the 2nd and 4th anomalous waves (Fig. 5.7a). The regular waves in Al/Al interface (Fig. 5.7d) show lower negative shear strains (maximum of 0.82) within a larger area and higher positive shear strains (maximum of 1.36) within a relatively smaller area. Therefore, the deformation of the Al/Cu pair and the flow behaviour of front and back sides of the waves are not symmetrical compared to the Al/Al case under the same welding parameters. Thus, the condition of dissimilar interface promotes the anomalous wave type1.

5.3.7 Wave morphology and jetting kinematics

To further study the kinematics of the wave formation, three typical wave morphologies are chosen, i.e. cases where (i) the wavelength on the front side is longer than that on the back side (Type 1), (ii) the wavelength on the front side is shorter than that on the back side (Type 3) and (iii) the wavelength on both front and back side is similar Type 4) (front side and back side are marked in Figs. 5.2i, k and l). Since it is difficult to distinguish the original surface of both Al and Cu after the welding process, the middle of the highest and lowest vertical displacement of each wave type is considered as the original location of welding surface. The vertical displacements obtained for waves Type 1, 3 and 4 are depicted in (Figs. 5.8a, b and c) respectively. For Type 3 and 4 waves, their vertical displacements (Figs. 5.8b and c) increase with increased impact angle. Watanabe and Kumai [60] studied dissimilar Al-Cu welds and showed that along the welding direction, the welding interface presents highly non-uniform wavelength and amplitude compared with the gradual variation within the Al/Al and Cu/Cu welds. It indicates that more complex interfacial kinematics are develop during the wave propagation at the Al/Cu interface.

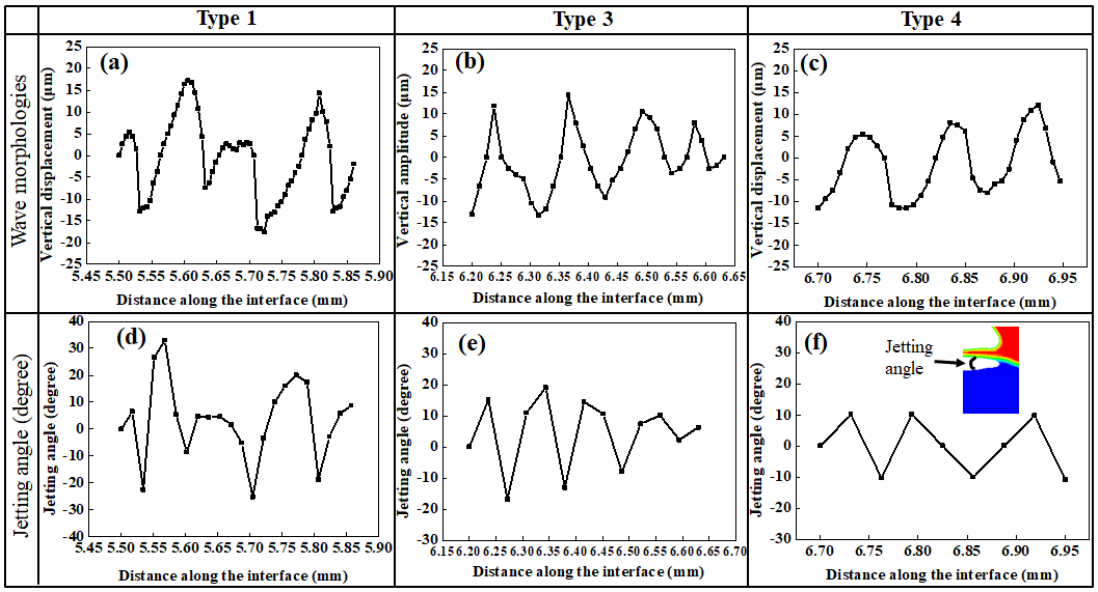

Fig. 5.8. (a), (b) and (c) present wave morphologies of Type 1, 3 and 4, respectively, which are obtained by image analysis using micrographs; (d), (e) and (f) are the predicted jetting angle from Eulerian simulation corresponding to wave Type 1, 3 and 4, respectively.

As discussed in section 5.3.5, the upward and downward jetting contribute to the wave morphologies. (Figs. 5.8d, e and f) shows the corresponding jetting angles along the waves Type 1, 3 and 4, respectively. The inset in Fig. 5.8(f) illustrates the jetting angle calculation from the simulation. The results show good agreement between the wave morphologies obtained by image analysis using micrographs (Figs. 5.8a-c) and the jetting angle obtained from the Eulerian simulation (Figs. 5.8d-f). The flat interface shown in wave Type 1 (between the distance along the interface of 5.65 mm and 5.70 mm in Figs. 5.8a and d, marked in Fig. 5.2i), is due to the approximately zero jetting angle during the wave development. It should be noticed that the wave Type 1 is more irregular compared to the waves Type 3 and 4 in terms of wavelength and amplitude. This could be explained by the values of the jetting angles (Fig. 5.8d) which is sometimes higher than the impact angle.

In (Fig. 5.8), we find a very good correlation between the jetting angle and corresponding displacement at a given instant; i.e. large jetting angle produces large vertical displacement. This effect is further illustrated in (Fig. 5.9) which

demonstrates that the absolute values of jetting angle and the vertical displacement exhibit an approximately linear relationship. Since a high shear instability and large pressure can produce high jetting angle, we can expect that a large shear instability could produce waves with large amplitude which is also associated with high probability of IM phases formation.

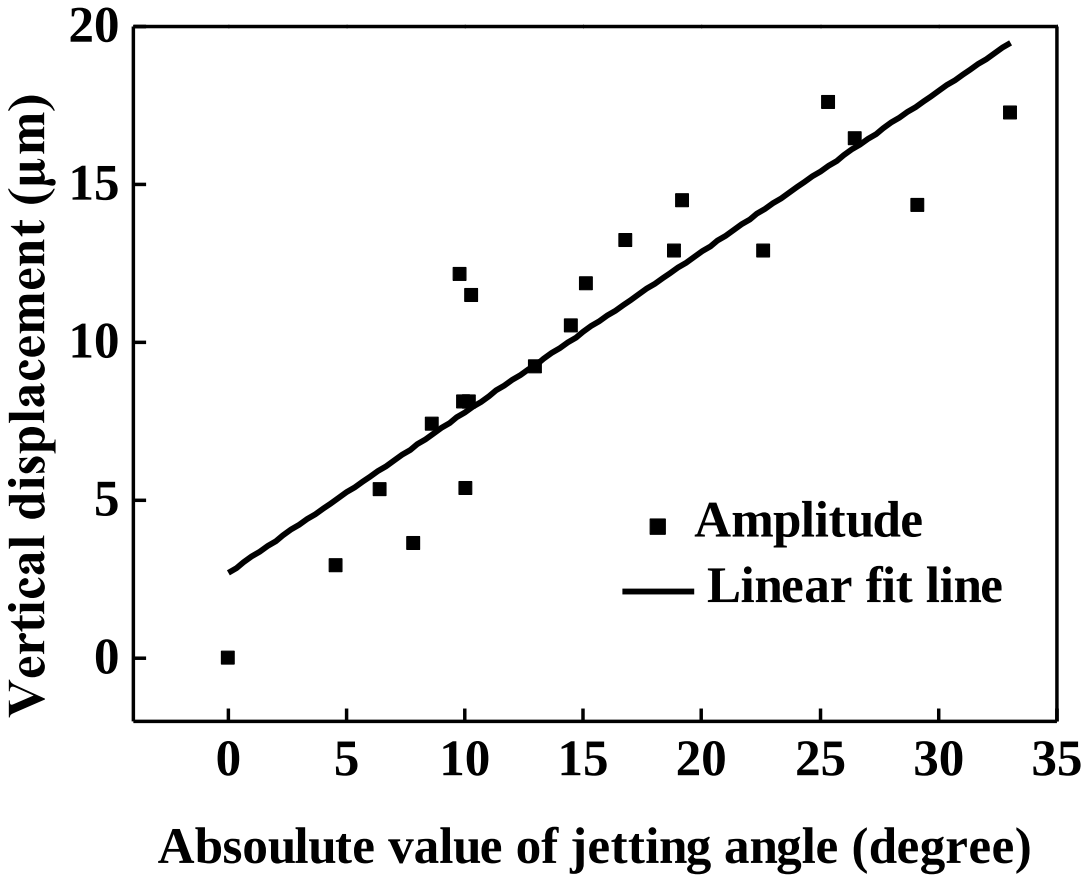

Fig. 5.9. Correlation between the jetting angle and the amplitude obtained from the waves.

5.3.8 Collision pressure and collision velocity

The pressure at the collision zone is an important parameter during the wave formation. It must be high enough to exceed the dynamic yield strength of the base metal to produce a jet. Since the collision zone reveals rapid variation, the average pressure at the collision zone is plotted in (Fig. 5.10a). It can be observed that the pressure generally decreases from the onset to the end for each wave while having

some random spikes. Compared with the pressure, the collision velocity experiences more fluctuations, as shown in (Fig. 5.10b). However, the collision velocity exhibits the same trend as the collision pressure.

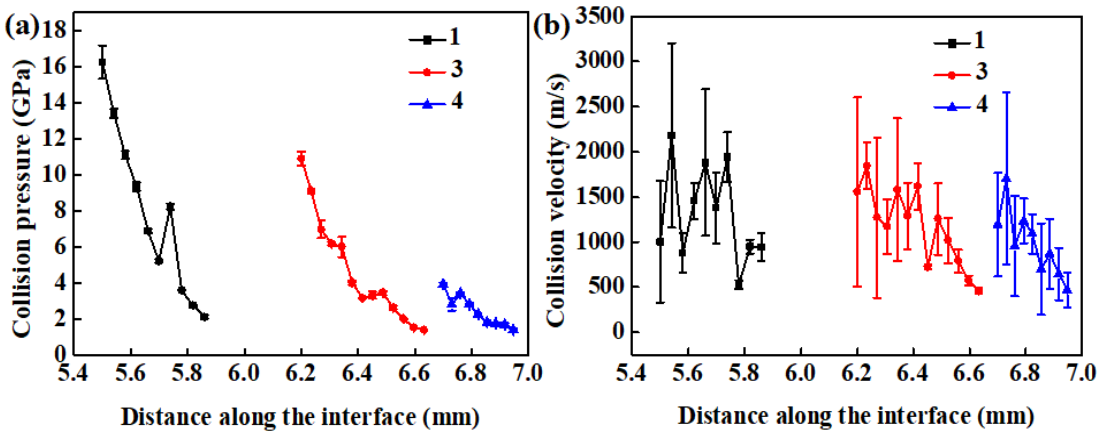

Fig. 5.10. Collision pressure and collision velocity along the wave interface obtained from Eulerian simulation for type 1, 3 and 4 waves (Fig. 5.8). Error bars represent the standard deviation, where the average and standard deviation of the pressure and velocity are calculated using 9 points from the simulation (the point with maximum pressure and the surrounding 8 nodes in a quadrilateral mesh).

Since the collision velocity is almost parallel to the interface, it could predominantly affect the wavelength according to the literature [115]. In this study, the half wavelength of each wave was measured in order to get more reliable data since the waves are not symmetrical. The half wavelength increases with increased collision velocity (Fig. 5.11a). However, the impact velocity also affects the wave propagation which may reciprocally affect the wavelength. The relationship between the ratio of "collision velocity/impact velocity" and the half wavelength is depicted in (Fig. 5.11b). Although (Fig. 5.11b) reveals a similar trend as in (Fig. 5.11a), the curve fitting confidence is higher in the case of (Fig. 5.11b): the ratio "collision velocity/impact velocity" is more suitable as an influencing factor for evaluating the wavelength during the MPW process.

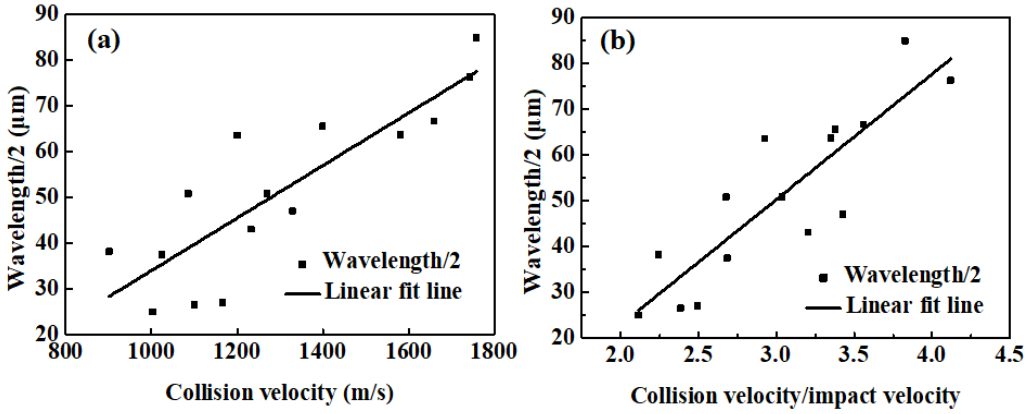

Fig. 5.11. Half wavelength evolution with (a) the collision velocity and (b) with the ratio of “collision velocity/impact velocity”.

5.4. Conclusions

In this chapter, various types of wave morphologies obtained from Al/Cu and Al/Al magnetic pulse welds were systematically investigated using experimental characterizations and numerical simulations. The important findings can be summarized as follows:

(1) Coupled electromagnetic mechanical (CEMM) simulations are used to predict the impact velocity and the impact angle during the MPW. Various welding zones were classified based on the above-mentioned predictions. Those classified welding zones correlate well with the experimentally observed morphology. Therefore, the predictive model can capture unwelded zone, vortex, IM zone, wavy interface and no contact zone along the welding direction.

(2) CEMM simulation demonstrates that the various morphologies are due to the highly dynamic impact velocity and impact angle along the interface. The impact velocity and impact angle exhibit significant fluctuations at the onset of welding. Then, the impact velocity gradually decreases while the impact angle increases during the propagation of welding.

(3) A thermo-mechanical model based on Eulerian method is used to successfully predict the various experimentally observed waves in terms of morphology, shape and

site occurrence. The temperature distribution and averaged equivalent plastic strain along the interface well correlate with the experimentally observed IM phases. The actual kinematics during the wave formation demonstrates that the wave morphology is formed with repeated deformations of the interface rather than with a single-step deformation. The intermediate zone is formed due to the melting resulting from the high shear instability, while the interdiffusion zone observed in the wave morphology is caused by the mechanical lattice instability due to the high-pressure impact combined with ultrahigh rate heating and cooling of over 10^{13} °C s^{-1}.

(4) Thermo-mechanical simulations can capture the complex interfacial kinematics due to the shear instability, including the jetting kinematics and non-uniform distribution of the positive and negative shear strains at the front and back sides of each wave.

(5) A large jetting angle enables to increase the vertical displacement of the waves and produces large wave amplitudes. Although both collision velocity and the ratio between collision velocity and impact velocity exhibit strong influence on the wavelength, the latest ratio is the most suitable for evaluating the wavelength.

Chapter 6

Interface evolution during magnetic pulse welding under extremely high strain rate collision: mechanisms, thermomechanical kinetics and consequences

Jishuai Li[a, 1], R.N. Raoelison [b], T. Sapanathan [c], Y.L. Hou[d], M. Rachik[a]

[a] Laboratoire Roberval, FRE UTC-CNRS 2012, Alliance Sorbonne université, Université de Technologie de Compiègne, Centre de recherche Royallieu, CS 60319, 60203 Compiègne cedex, France

[b] Université de Bourgogne Franche-Comté - UTBM, Laboratoire Interdisciplinaire Carnot de Bourgogne, UMR 6303 CNRS, 90100 Belfort, France

[c] UCLouvain, Institute of Mechanics, Materials and Civil Engineering, 1348 Louvain-la-Neuve, Belgium

[d] School of Mechanical and Power Engineering, Zhengzhou University, Science Road 100, 450001 Zhengzhou, China

6.1. Abstract

A local thermomechanical model (see details in section 4.4.2.2 in chapter 4) is used in this chapter to investigate the formation mechanism of the wake, vortex, swirling and mesoscale cavities with the increase of the impact intensity at the interface. Our studies identify the governing mechanisms and the associated thermomechanical kinetics, of these interfacial features. Numerical predictions of wake and vortex resulting from the re-entrant jetting in-conjunction with the complex interfacial mixing are in good agreement with the experimental observations. The computational analysis reveals multiple heating stages of the interface due to the

1. This paper has been published in Acta Materialia.

contact of ejecta particulates, adiabatic shearing during the onset of the collision, and the swirling motion of the materials at the interface zone. This repeated heating of the materials and the advent of rapid solidification produce the vortex zones. The high-speed kinematics of the vortex associated with the local heating at the vicinity of the interface lead to the formation of swirling structure and mesoscale cavities in the centre of the swirls. The shape and the size of these predicted cavities are in good agreement with experimental observations.

6.2. Introduction

In the previous chapters, experimental characterization of the Al/Cu MPW welds with various interface morphologies, such as wavy, wake and vortex, were observed. These features are develop due to the excessive shearing at the interface which behaves like a fluid during the high strain rate collision [27]. It was observed that the impact velocities in the range of [300, 600] m/s produce the flat and wavy interfaces, which has been investigated in Chapter 5. However, there is no systematic analysis of the physical phenomena and kinematics of the complex interfacial evolution, i.e., the wake, vortex, swirl and cavities, during the MPW process.

The wave is generated along with the intermittent upward and downward jetting that has the possibility to evolve towards a vortex structure due to a swirling at the wave crest with the increase of impact intensity. These phenomena lead to an intermixed zone which causes a mechanical interlocking that is capable of improving the joint strength [168]. Some studies further investigated microscale characterizations of the vortex that result in identifying various microstructures, intermediate phases [40,49,88,169], nanoscale amorphous and metastable phase [58,73,170] and recrystallized or nanostructures grains [171–174]. However, due to the extreme difficulty of carrying out *in-situ* observations, the complete formation mechanisms of the evolution of wake, vortex and swirls at the interface remain unclear.

With the recent progresses in computational modelling techniques over the last two decades, physical realistic simulation of interfacial waves [123,163,175] and vortices [103,104] at various interfaces of Al/Steel, Ti/Cu, Al/Fe and Steel/Steel reveal good agreement between the predictions and the experimental observations and provide some understanding of the interface morphologies produced during HSIW. However, the formation of vortices was explained by the swirling of the melt [103] which is in contradiction with another possible mechanism due to the trapping of a re-entrant jet [104]. Therefore, the vortex formation mechanism at the HSIW interfaces remains a subject of open discussions. The formation of mesoscale cavities at the interface zone in HSIW is an undesirable feature, which result from unsuitable welding conditions and reduce the weld integrity. However, their fundamental evolution mechanism and the thermomechanical kinematics are rarely investigated. Some specific types of porous structures formed during the high-speed collision have recently been investigated using microstructural observations showing various length scales from submicron to micron sizes [76,89,143]. The porous structures reveal a hierarchical porosity including randomly distributed submicron/micron pores with an ultrathin membrane of wall thickness of 50 nm [44]. Mesoscale spherical cavities of up to hundreds of micrometers have also been observed along the welded interface [52,176,177]. However, there is a lack of understanding on the formation of the mesoscale spherical cavities at the centre of the swirls at the interface during HSIW.

6.3. Impact velocity and impact angle along the interface

The position where V_{impact} and α are extracted from the CEMM model corresponds to the same region where the specimen was taken for the experimental observations (90° to the slot). The evolution of V_{impact} and α with the distance from the top side of the tube is illustrated in (Fig. 6.1). The distance corresponds to 8.7 mm marked by blue line in (Fig. 6.1a and b), and shows the contact between flyer and rod during the simulation that agrees with the experimental observations. The highly rapid fluctuations of V_{impact} and α explain the various local features, i.e., flat interface, wave

interface, wake, vortex, swirl and cavities.

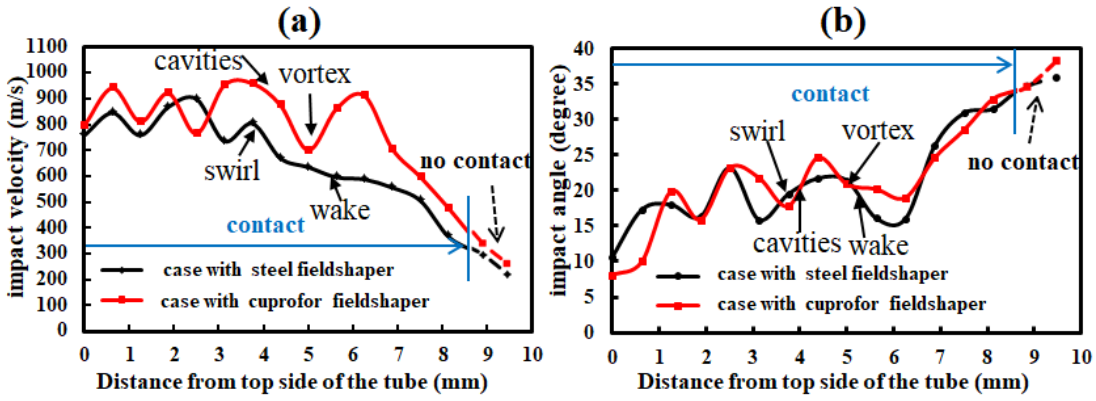

Fig. 6.1. Velocity and angle along the interface obtained from CEMM simulation. (a) velocity and (b) angle. The solid black and red lines portions of the curves in (a) (distance ≤ 8.7 mm) correspond to the impact velocity of the flyer, which impacted the inner rod. Beyond the distance 8.7 mm, the curves are extended by dashed lines which simultaneously correspond to the process flyer without contact to the inner rod.

In our physical tests, the wake and swirl appeared at the distance of 3.8 mm and 5.4 mm from the top surface at the tube, in the case of Steel FS with 8kV. In the case of Cuprofor® FS with 8kV, the cavities and vortex were found at the distance of 4.0 mm and 5.0 mm from the top surface at the tube. Therefore, we used the location of specific impact velocity and impact angle from the corresponding positions marked in (Fig. 6.1a and b). The results show that the impact angle is about 20° for wake, vortex, swirl and cavities formation. However, the impact velocities are different for each future to appear (~600 m/s for wake, ~700 m/s for vortex, ~800 m/s for swirl and ~900 m/s for cavities). Therefore, we use (1) low impact velocity [20°, 600m/s], (2) medium impact velocity [20°, 700m/s], (3) high impact velocity [20°, 800m/s] and (4) higher impact velocity [20°, 900m/s], as the input data for the thermomechanical model (see section 4.4.2.2 in chapter 4 for more details) to further study the physical phenomena and kinematics of these features.

6.4 Results and discussion

Due to the high-strain rate at the interface, the materials have a high viscosity

fluid like behaviour leading to various interface instabilities. Among which the wave formation at the interface has been systematically investigated in Chapter 5. However, other complex interface instabilities are barely investigated because of the requirement of a sophisticated model and difficulty to capture the real time instabilities from a phenomenological point of view. The proposed Eulerian model proves its capability to predict: (1) wake, (2) sequential vortex formation, (3) subsequent swirling and (4) large cavitations. These interface phenomena, their mechanisms and thermomechanical kinetic changes during their formations are discussed in sections 6.4.1 – 6.4.6, using both numerical predictions and experimental observations.

6.4.1 Wake formation

The kinematic changes during the development of a wake corresponding to a low impact velocity [20°, 600 m/s] are depicted in Fig. 6.2. The welding propagation direction is from the right to left. At the beginning, some ejecta produced by a jetting from the interface fall on the surface of the inner rod and they enable thermal softening at the local contact zones (Fig. 6.2a). Then, the upward jet interacts with an earlier protrusion emerging on the inner rod (Fig. 6.2b). At this stage, the inner rod experiences large plastic deformation slightly in front of the collision point. After that, the deflected downward jet traps the previously ejected particle within the interface morphology (Fig. 6.2c-d). The interface continues to evolve while the shear instability behind the collision point along with the forward jetting facilitates the formation of a depression zone (Fig. 6.2e). As the collision progresses with the increase of both deformation of materials and shear instability, the depression zone becomes larger and squeezed compared to the previous instant (from Fig. 6.2f to Fig. 6.2g). The interface along the depression zone concurrently flows further and evolves into a wake (Fig. 6.2h and 6.2i). Thus, the mechanism of wake formation can be described as a result of the successive material jetting along with the intense shear instability at the interface during the progressive collision.

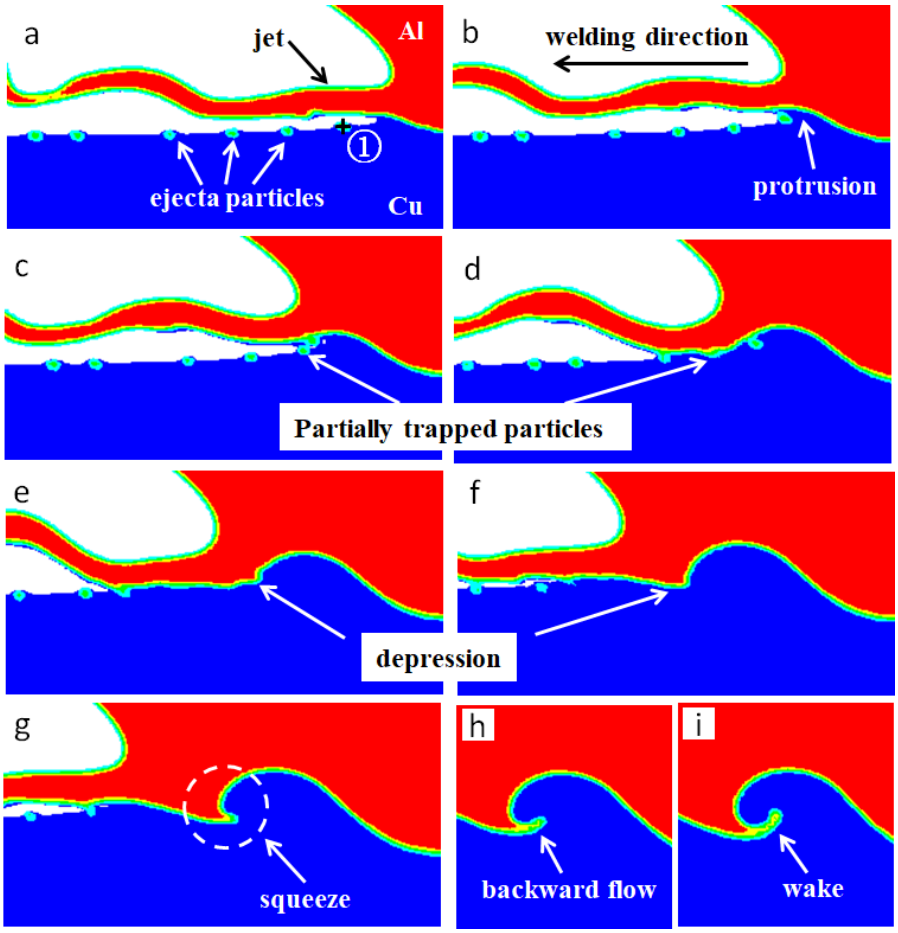

Fig. 6.2. Sequence of wake development steps obtained for a low impact intensity [20°, 600m/s] during MPW. Presence of fallen ejecta particles from the jet onto the inner rod (a), initiation of protrusion (b), deflected downward jetting and the trapped ejecta particles (c-d), depression zone formation (e-f), squeezing (g), backward flow of material (h), and final stage of wake formation (i).

The consecutive and recurrent wake predicted using the Eulerian simulation concurs with the experimental observations in terms of intermittent interface pattern as shown in (Fig. 6.3). The numerical computation is able to capture the irregular wake with the increase of the wave amplitude along with the progression of the weld (from right to left in Fig. 6.3a and b). A computed temperature field of the wake is mapped for the last time step (after completion of 4th wake) in (Fig. 6.3c), that shows the local heating due to the plastic dissipation. The experimentally observed intermediate discontinuous pockets along the interface are well predicted by the simulation corresponding to the temperature values above 440 °C within the wakes

(Fig. 6.3c). Their site occurrences (marked by white arrows in Fig. 6.3c) concur with the intermediate zones of the experimental observation (Fig. 6.3b). It should be noted that the temperature map obtained at the time step after the formation of the 4th wake, at the moment of the first wake has already been cooled down slightly. The temperature rise at the 3rd and 4th wakes still indicates that the Al part is melted (~ 660 °C) at the standard atmospheric conditions. Thus, a local rapid melting followed by a sudden cooling could leads to the formation of intermediate pockets (Fig. 6.3b). Additional investigation on the thermomechanical kinetics during the wake formation is reported in section 6.4.3.

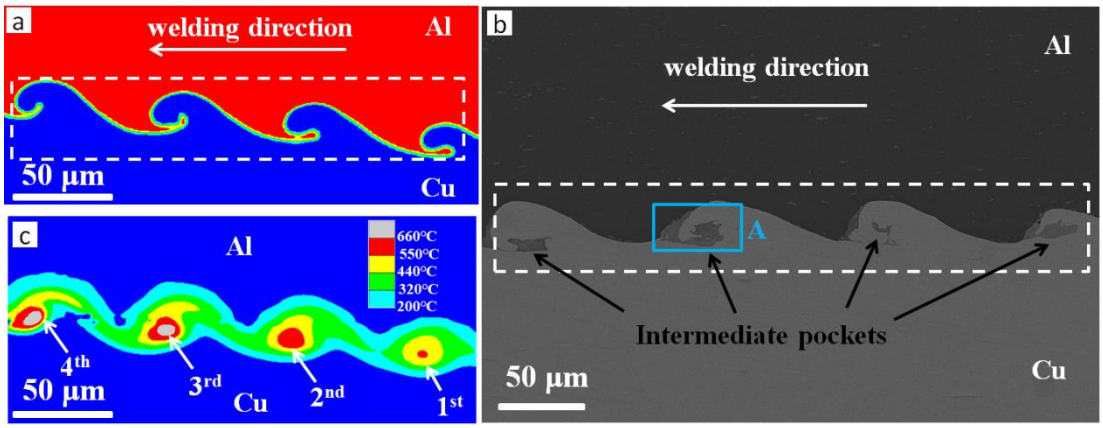

Fig. 6.3. (a) Numerical prediction of recurrent wakes from Eulerian simulation where the wakes are highlighted within the white dashed rectangular box, (b) a secondary electron image of the interface obtained from the longitudinal cross section of Al/Cu weld joint produced with 8 kV input voltage using steel field-shaper, showing the wake (within the white dashed box) and the intermediate pockets and (c) local temperature map obtained at the time step of the 4th wake formation.

6.4.2 Sequential vortex formation

With the increase of impact intensity, the wake evolves towards a vortex due to the increase of shearing and interface instability. The increasing impact intensity was experimentally obtained using a high conductive field-shaper made of Cuprofor® that enables to increase the Lorentz force and thus the acceleration of the flyer compared with the less conductive steel field-shaper. The simulation results obtained from the

corresponding medium impact velocity case [20°, 700m/s] are compared with the experimental observation as shown in (Fig. 6.4).

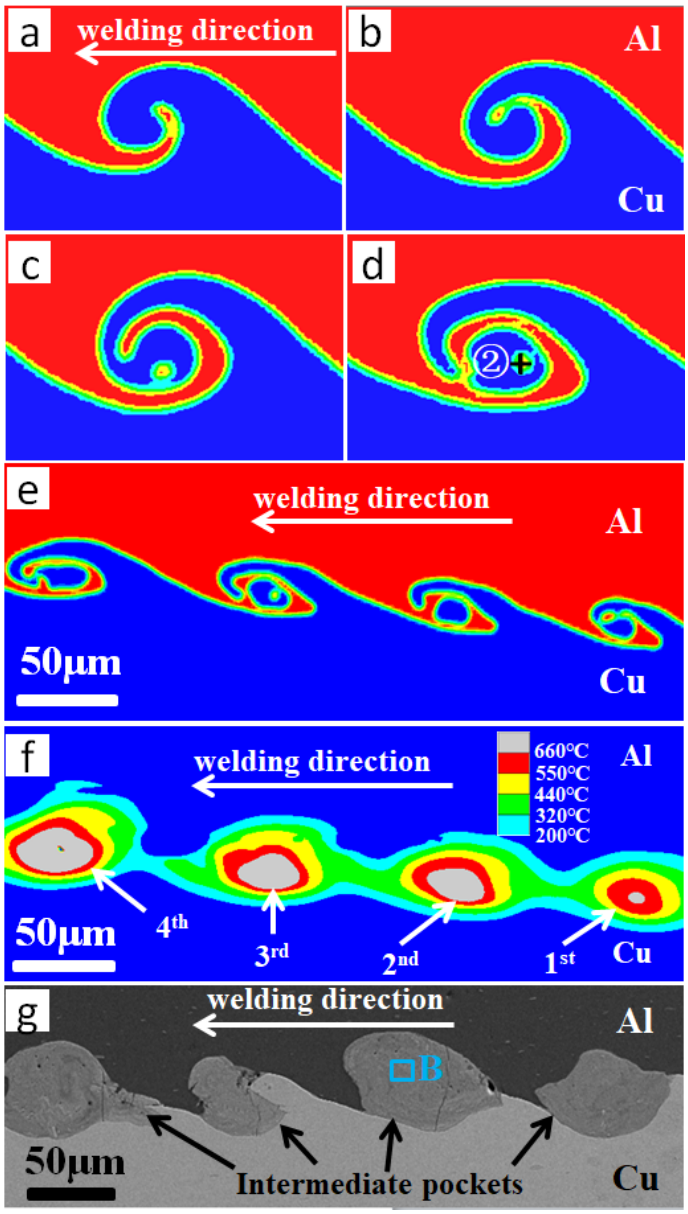

Fig. 6.4. The sequential steps of vortex formation revealing the twisting and rolling up mechanism at the Al/Cu interface in (a-d), serious of vortices in (e), computed temperature field with confined local heating in (f), in agreement with the SEM observations of the corresponding intermediate pockets due to the intermixing of materials in (g).

Similar behaviour occurs during the collision of the Al flyer with the stationary Cu rod. Along with the progressive collision, a relative tangential velocity at the interface occurs and induces a swirling kinematics of the materials at the interface.

The materials at the interface twist and roll up to form vortex like in a fluidic interface which is generally attributed to Kelvin-Helmholtz phenomena due to a shearing across the interface of two fluids (Fig. 6.4a-d) [27]. The repetition of the vortex formation along the interface creates a series of vortices with the progression of the collision (Fig. 6.4e). Thus, both Cu and Al tend to intermix at this local zone (Fig. 6.4b-e). The plastic work accompanied with the swirling kinematics also significantly increases the local temperature (Fig. 6.4f). The temperature field obtained at the time step of fourth consecutive vortex reveals that all the local vortex zones experience an elevated temperature above the melting temperature of Al (~ 660 °C). Besides, the temperature at the first vortex is slightly lower due to the dissipation of heat during the progressive collision. However, the overall zone affected by the increase of temperature is larger than that observed in the earlier wakes (Fig. 6.3). In terms of shape and site occurrence, this computed heat confinement at the vortex corroborates the experimentally observed intermediate pockets formed in the corresponding welding case of 8 kV input voltage using the Cuprofor® field-shaper (Fig. 6.4g).

6.4.3 History of thermomechanical kinetics during wake and vortex formation

The temperature and local forces at the interface significantly affect the interfacial morphology during MPW. Thus, the temporal evolutions of the interfacial heating and local pressure are investigated to understand the peculiar behaviour of the interface during the high-speed collision. The typical variations of temperature and pressure obtained from the wake are depicted in (Fig. 6.5). The temperature and pressure curves are probed at point ① (Fig. 6.2a) and corresponds to the site of first ejecta from the left. Initially, during the progressive collision, the probed zone ① increases its local temperature due to the contact of a high temperature ejecta at the local zone (from stage I to stage II in Fig. 6.5). Meanwhile, the local pressure does not show any change as the collision does not reach this local point ①. Before the onset of collision at this point, a cooling process (from stage II to III) occurs due to the heat flow from the probed zone to the surrounding material. Subsequently, the collision arrives to the point, and it induces the second major heating (from stage III to IV) and

a significant increase of pressure (7.6 GPa at stage IV). The interface temperature increases up to approximately 900 °C (stage IV) during the second heating, which enables to locally melt the Al. After that, both pressure and temperature of the local zone decrease simultaneously. During the early stage of cooling (stage IV), the cooling occurs at a rate of ~10^{10} °Cs^{-1} and after a few hundred ns, the cooling rates drops to 10^{9} °Cs^{-1} – 10^{8} °Cs^{-1}. The heating and cooling rates predicted by the numerical simulation are in good agreement with the analytical estimations of the literature [170]. The molten area solidifies during the cooling (stage IV to V) while the interface is bonded to form the wake. Therefore, the wake structure finally appears due to the combination of the double heating, i.e., the contact of ejecta and adiabatic shearing action during the onset of the collision, and the advent of rapid cooling.

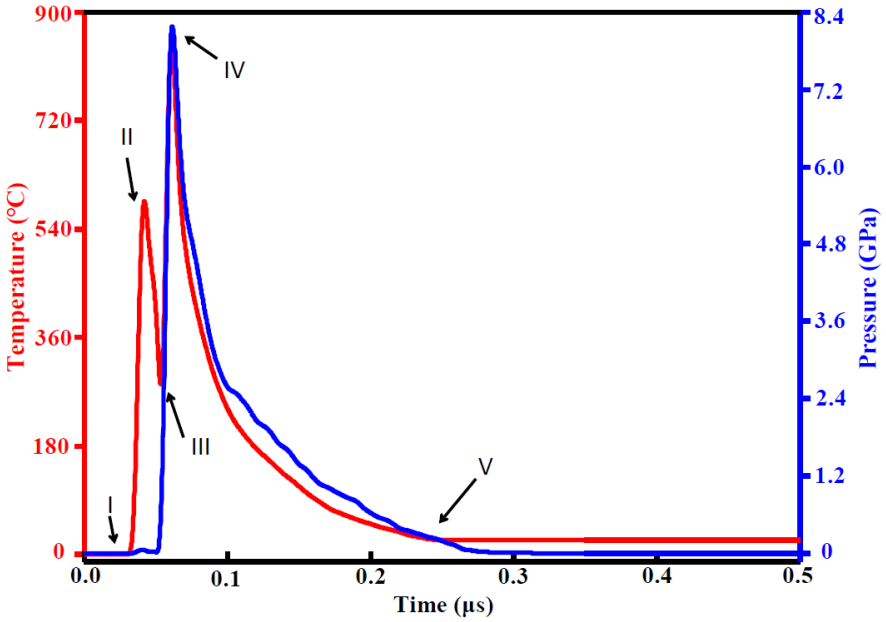

Fig. 6.5. The time-dependent temperature and pressure curves obtained from the wake corresponding to point ① indicated in (Fig. 6.2a), when performing the simulation with the welding case of [20°, 600m/s].

The temperature and pressure history curves for the vortex zone are depicted in (Fig. 6.6) which is obtained from the corresponding point ② indicated in (Fig. 6.4d). Similar to the wake, the first heating and cooling (stages A, B and C in Fig. 6.6) result from the heating due to the ejecta at the interface. Then, the advent of impact with increasing intensity causes the second heating (from stage C to D). The temperature

rises to 1200 °C (stage D) due to the sufficiently high impact intensity with the pressure of ~10.0 GPa, revealing that the interface undergoes larger plastic deformation than that in the wake. As the interface pressure and temperature start to drop, the interface is continually affected by the swirling vortex which results in a third heating (from stage E to F). In comparison with the wake, the increase of intensity in the vortex produces relatively high temperature and pressure that facilitate the formation of large zones with elevated temperature (see Fig. 6.3c and 6.4f). Thus, these repeated heating stages due to jetted particle contact with the interface, the onset of the impact followed by the swirling motion and the final cooling (from stage F to G) lead to the formation of the vortex.

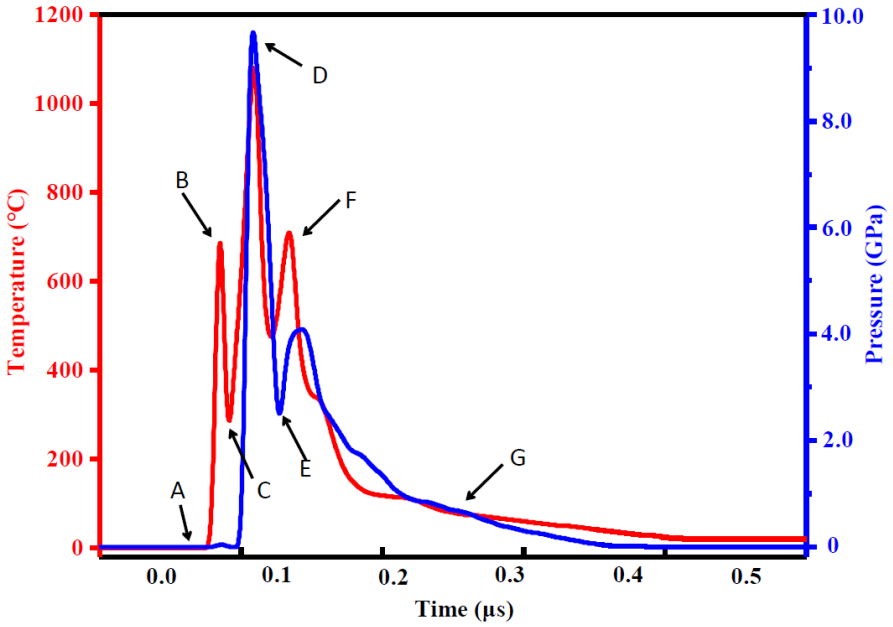

Fig. 6.6. The temperature and pressure curves obtained from the vortex zone marked by point ② in (Fig. 6.4d) corresponding to the simulation case of [20°, 700m/s].

6.4.4 Microstructural characteristics of the wake and vortex zones

The experimentally observed wake and vortex zones (Fig. 6.3b and Fig. 6.4g) are investigated to elucidate the mixing of the two base metals and the resulting microstructural features of corresponding interfaces. SEM image of the wake zone, from the area 'A' marked in Fig. 6.3b, is shown in Fig. 6.7a. It reveals the Cu fragments (marked by white arrows in Fig.6.7a) inside the corresponding wake zone. This phenomenon attributed to the high shear deformation of the interface zone (both

Al and Cu) with a mechanical mixing during this low impact intensity [20°, 600m/s]. The wake zone form liquid/solid interface combined with the high pressure and temperature (max 7.6 GPa and 900 °C, see Fig. 6.5) promote the fast reaction and diffusion of Cu in Al liquid, and the formation of Al/Cu intermetallic (Al_2Cu based on our Energy-dispersive X-ray spectroscopy (EDS) analysis) [178].

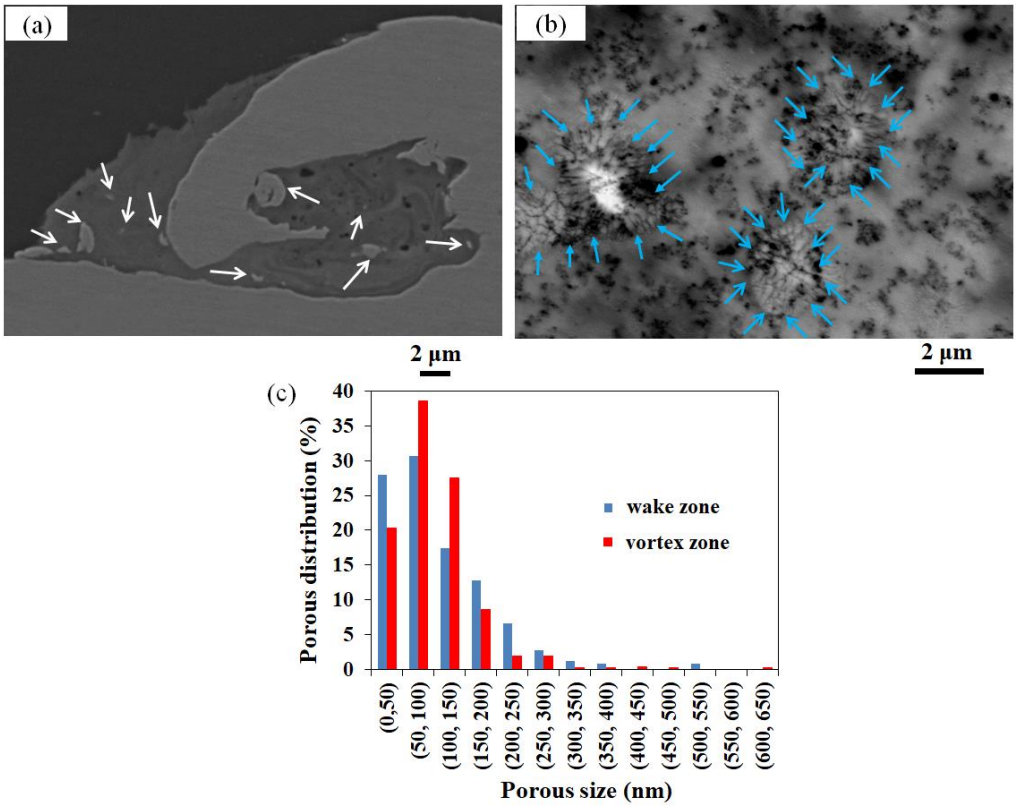

Fig. 6.7. (a) Microstructure image of the wake zone under SE mode revealing the mechanical mixing and porous architecture; (b) BSE images of the porous zone within a vortex revealing the traces of rapid solidification (random epitaxial and columnar cells); (c) pore size distribution of both wake and vortex zones.

Fig. 6.7b presents the BSE image of the vortex zone which is obtained from the area ‘B’ marked in (Fig. 6.4g). This image clearly shows the fine structure of random allocation epitaxial growth and columnar cells (marked by the blue arrows). This microstructure could be attributed to the rapid solidification in the vortex zone because of the insufficient time for solidification (Fig. 6.6). Simultaneously, there are randomly dispersed black spots that correspond to the nano-size pores within the

vortex zone. In this increased impact intensity condition (compared to the wake formation), the temperature reaches the melting point of the Al and Cu, that enables a complete mixing of both material with absence of Cu fragments. This phenomenon is also in agreement with the numerically predicted high pressures (8 GPa<P<14 GPa) and high temperature (T>1098 °C) of these zones that can increase the diffusion between Al and Cu, and form multiple Al/Cu intermetallics [151]. Based on our EDS results, the vortex zones are identified as a Al_2Cu component.

In the SEM observations, the porous architectures reveal a random allocation of pores with heterogeneous spatial distribution (Fig. 6.7a and b). A qualitative image analysis using multiple SEM images obtained from the wake and vortex zones are used to compare the pore size distribution between the wake and vortex zones (Fig. 6.7c). In both cases, the dispersed sizes vary from few to hundred nanometres. Meanwhile, one can notice an increasing number of pores greater than 50 nm in the vortex zone compared to the wake zone. This could be due to the increase of heating duration at the elevated temperature, to produce more time for the pores to growth in the vortex zone than in the wake zone, prior to the solidification (see Fig. 6.5 and 6.6).

The thermomechanical model predicts that the interface experiences a rapid melting-solidification, the volume of the material is subjected to a sudden increase of temperature followed by a rapid cooling under isochoric condition. This condition is favourable for the formation and growth of nano-sized pores where the pores are formed to maintain the conservation of the total volume in the material [179]. Concurrently, the pressure gradient in the local zone facilitates the depressurization necessary for cavitation. It is suggested that the local pressure decreases below the saturated vapor pressure of Al liquid and generates spherical vapor bubbles. Then, the fluid rupture that occurs due to the change in surface tension via this depressurization [180] within the molten liquid zone provides the necessary condition for the nucleation of fine pores. At the same time, the growth and coalescence of pores within the confined volume could also be facilitated by the contraction/shrinkage that occurs during the cooling.

6.4.5 Swirling at the vortex zone

When the interface instability reaches further advanced stages, we can clearly acquire the mixing pattern of the swirling whirlpool traces within the vortex zone from a BSE image. To clearly capture the mixing path, the image is taken with high contrast as shown in (Fig. 6.8a). High magnification of the specific vortex zone (Fig. 6.8b) reveals the details of the intermixing zone with the presence of a micro porous structure. The porous structure is also found in this zone with random and heterogeneous spatial distribution and dispersed sizes, due to the same mechanism as discussed in section 6.4.4. The prediction of the swirling zone is depicted in (Fig. 6.8c) and it well concurs with the experimentally observed whirlpool (Fig. 6.8a and b).

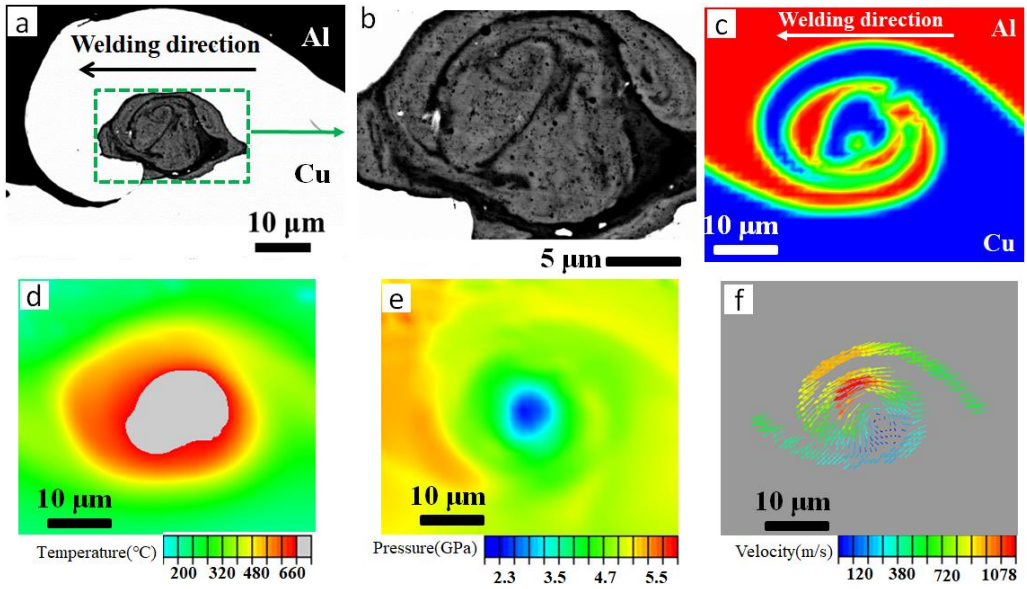

Fig. 6.8. Experimental observation from the longitudinal cross section of Al/Cu weld joint produced by the 8 kV input voltage using the steel field-shaper and numerical predictions of swirling phenomenon with increased impact intensity corresponding to the simulation case of [20°, 800m/s]. BSE image showing the swirling phenomenon obtained from MPW interface while using steel field-shaper (a); high magnification image showing porous zone within a swirling vortex (b); predicted swirling morphology from Eulerian computation (c); the map of temperature (d), pressure (e) and visualized velocity field vectors corresponding to the individual elements along the swirling path (f). For illustration purpose velocity only along the vortex path is depicted to clearly show the vortex phenomena in (f).

The computed temperature, pressure and velocity maps within the swirling vortex zone are shown in (Fig. 6.8d-f). The temperature gradually decreases from the centre towards the periphery of the vortex, and it reveals a localized temperature considerably higher than the melting temperature of Al (> 660 °C, Fig. 6.8d). Moreover, the interface experiences an ultrafast heating + cooling that enables the local zone to undergo a rapid melting and solidification under isochoric condition (see section 6.4.3). The field map of velocity shows that the material within the swirl experiences large gradient of speeds between 120 m/s and 1078 m/s (Fig. 6.8f). For illustration purpose, velocity along the vortex path is depicted to clearly show the vortex phenomena (Fig. 6.8f) while other surrounding velocity field is not visualized in this image. Moreover, the varying directions of velocity field observed along the swirling path clearly indicate the motion trajectories of the swirling flow. Therefore, the combination of the temperature, pressure and velocity predicted from the thermomechanical simulation well describes the whirl trajectories and the porous structure formation at the Al/Cu interface.

6.4.6 Consequence of the swirling under extreme instability

The highest impact intensity condition [20°, 900m/s] produces the swirling material flow while having some chaotic behaviours. Furthermore, the experimental observations from the same welding condition highlight mesoscale cavities (Fig. 6.9a). The mesoscale cavities have a maximum average diameter of 44.5 μm while the corresponding intermediate zone has an average diameter of 95.0 μm. These experimentally identified cavities concur well with the central zone (the empty space corresponding to the white color) of the swirls predicted by the Eulerian simulation (Fig. 6.9b). In addition, these cavities are spherical, so that they are considered as a result of physical kinematic evaluation rather than purely based on the high impact pressure that would shrink or distort such cavity. Nevertheless, the literatures on HSIW report such cavity in some experimental welding cases, but the actual mechanism of the cavitation has not been investigated, despite the existence of some suggestions crediting the local melting and solidification of the materials at the

interface [49,143].

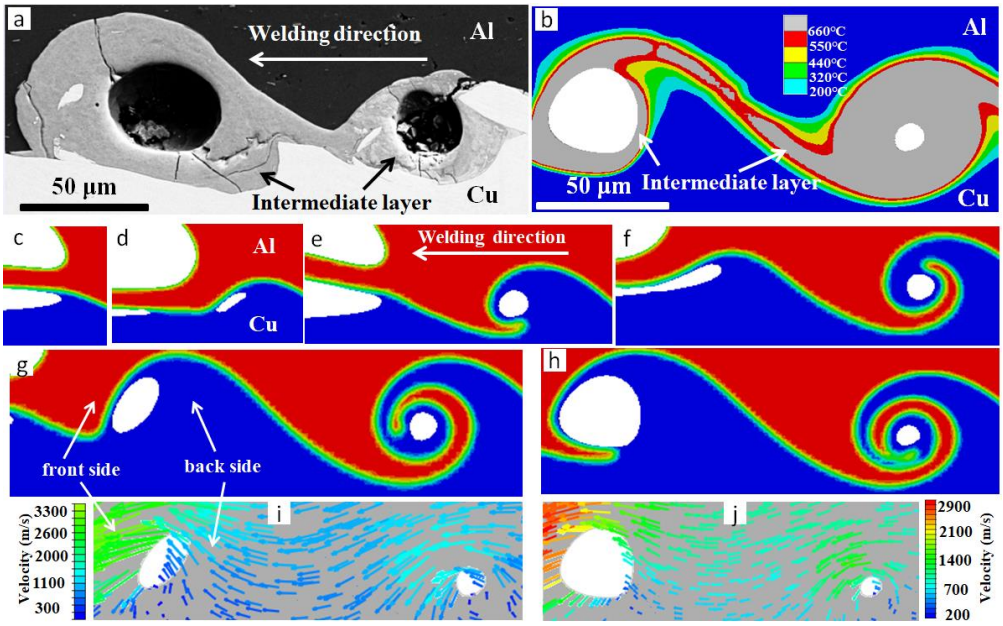

Fig. 6.9. Experimental result obtained from MPW using 8kV input voltage and Cuprofor® field-shaper and kinematic instability obtained from the highest impact intensity [20°, 900m/s] revealing the development of mesoscale cavities: (a) SEM image of the mesoscale cavities; (b) temperature field obtained during the formation of corresponding mesoscale cavities; (c-h) the sequence of mesoscale cavity formation; (i and j) velocity field maps corresponding to the instances of g and h, respectively.

The temperature distribution illustrated in (Fig. 6.9b) shows the complete morphology of the intermediate zone at the high intense vortex region. In this area, the missing materials (i.e. the empty space corresponding to the white color) also well predict the shape, size and occurrence sites of these cavities. Along with the progressive collision (from right to left), the size of the mesoscale cavity increases as the result of the increase in impact kinematics (i.e. the second cavity is larger than the first one on the right in Figs. 6.9a and 6.9b). The temperature predictions also reveal relatively large high–temperature-zones with temperature above 660 °C and even some points where the temperature is higher than that of the melting point of Cu at the vicinity of the large cavity (Fig. 6.9b). Therefore, this confined local melting and thermomechanical softening, followed by an ultra-high cooling provide a favourable

condition for the surrounding regions of the large cavities to form a continuous intermediate layer. Moreover, several cracks in radical direction are observed at these regions and this could be due to high thermal residual stresses during the solidification and the presence of multiple material at the interface (Fig. 6.9a) [181, 182].

The sequential kinematics of the mesoscale cavity formation during MPW along the interface are depicted in (Fig. 6.9c-j). The sequence of insets provides an excellent description of the interface morphology resulting from the irregular shape due to a trapped empty space. The shearing action at the front of the trapped empty space is higher than the back side due to the increasing velocity at the front of the cavity compared to the back side (Fig. 6.9i and j). Therefore, a very fast circular motion occurs in the liquid phase at the vicinity of trapped empty space which enables the irregular shape of the trapped empty space to become circular.

As mentioned before, the mesoscale cavities are form due to a strong swirling inside the vortex. The BSE image (Fig. 6.10a) clearly illustrates the traces of swirling at the vicinity of the mesoscale cavity. Moreover, an unaffected surface (during the standard metallurgical sample preparation) obtained from the inside of the cavity is shown in (Fig. 6.10b). The unaffected surface clearly confirms the 3D nature of the cavity, while it characterizes the solidification structure by random location of grains with a slightly rough surface (i.e. bright and dark grey zones corresponding to small humps and valleys, respectively). The simulation well reproduces the mesoscale cavity within the intermixing material corresponding to the intermediate zone from the experimental observation (Fig. 6.10c). Fig. 6.10d presents the characteristic variations of temperature, pressure and velocity along the interfacial path (marked by the black dash line, from A to E, in Fig. 6.10c) inside the vortex. The temperature profile evidences the vicinity of the mesoscale cavity having a high temperature with a strong transient response (temperature peak in curve at point ii corresponding to position C in Fig. 6.10c) that exceeds the melting point of Cu along the path. Simultaneously, a lowest velocity (velocity peak at iii) is identified in the same

position surrounded by the high velocities (velocity peaks in curves at points i and iv, respectively corresponding to positions B and D in Fig. 6.10c). Therefore, the molten zone mixes with an intense rotating motion due to the extreme instability of the interface which results in the mesoscale cavity within the vortex zone. When noticing this mesoscale cavity formation at the interface, it is clearly comparable to extremely large scale events happening in nature, such as the formation of a cyclone [183]. Thus, the simulation provides further clue to predict the extremely chaotic interface characteristics at the HSIW interface, while the consequences may possibly be linked to the nature events due to the similarity in the kinematic principles. Based on the investigation of experimental observations and numerical simulation, it was found that the mesoscale cavity formation within the swirling vortex requires the following conditions: (1) sufficient heat, (2) drastic swirling and (3) ultra-high cooling.

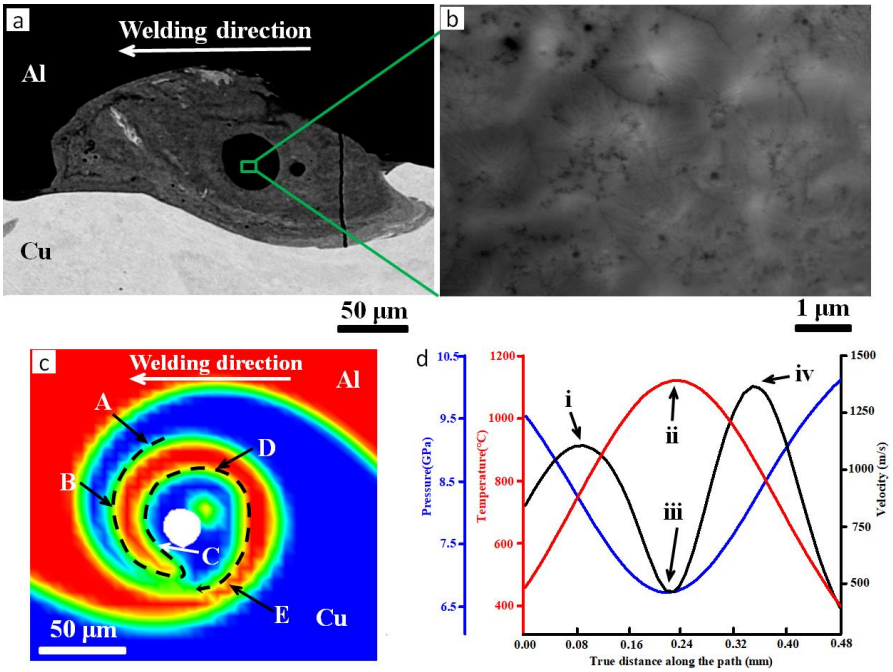

Fig. 6.10. Mesoscale cavity obtained from experimental observation from MPW with 8 kV input voltage and Cuprofor® field-shaper and Eulerian computation using [20°, 900m/s]:(a) BSE observation of a cavity formation within the intermediate zone surrounded by a vortex; (b) the unaffected surface within the cavity; (c) the mesoscale cavity and swirling predicted by the simulation; (d) temperature, pressure and velocity changes with the distance along the specific path marked in (c) and the peak i, ii, iii corresponding to the position B, C, and D marked in (c), respectively.

6.5 Conclusions

In this chapter, we leverage numerical simulations and experiments to systematically investigate the mechanisms, thermomechanical kinetics and consequences of the interface evolution under extremely high-strain rate collision during magnetic pulse welding. The predictions help to understand the fundamental process behaviour during the interface evaluation. Different heating mechanisms are identified in the wake and vortex zones and reported here. The conclusions:

(1) The wake, vortex, swirling structures and mesoscale cavities are successively formed at the interface with the increase of the impact intensity under extreme impact conditions.

(2) The formation of wake can be attributed to the combination of the successive indentation of protrusions arising from the ejecta and the intense shear instability at the interface during the progressive collision. The formation of vortex occurs due to further interfacial shear instabilities and swirling phenomenon. These predictions also explain the specific solidified swirling trajectories within the vortex observed in experiments.

(3) The complex interfacial mixing governed by the wake and vortex instabilities causes a confinement of heating in these regions that promoted the formation of the intermediate pockets. Two different heating mechanisms, i.e., double heating stages due to the contact of ejecta and the onset of impact; triple heating stages due to the contact of ejecta, the onset of impact followed by a swirling motion; are responsible for the wake and vortex morphology, respectively.

(4) The ultra-high heating combined with a rapid expansion caused by depressurization followed by rapid cooling facilitates the sequential phenomena of pore nucleation, coalescence and growth within the melted zone which explains the formation mechanism of sub-micro/micro porous structure. The trapped empty space during the drastic swirling in the vortex zone combined with the favourable thermomechanical conditions of the interface explains the formation of

experimentally observed mesoscale cavities within the intermediate pockets.

Overall, the local impact thermomechanical simulation provides a non-destructive approach to identify the interfacial structures in an impact welded joint. It will be further used to identify a weldability window in next Chapter.

Chapter 7

Prediction of a MPW weldability window of Al/Cu using numerical simulation

7.1. Abstract

This chapter attempts to predict the straight and wave interfaces during a MPW of Al to Cu. Then, a typical simulated interface is systematically investigated. The straight interface, wavy interface, vortex and cavities are successively computed along the welding direction. The statistical analysis show that the dynamic collision angle constantly increases while the collision velocity decreases along the interface. The simulation results reveal a difference in plastic strain, temperature and stress between the Al side and Cu side. Finally, these predicted interface morphologies are used to build a weldability window using an impact velocity–impact angle diagram.

7.2 Results and discussion

7.2.1 Straight and wave morphologies

For the sake of clarity, the impact conditions (V_{impact} and α) and the region where the experimental observations were performed are summarized in Table 7.1.

Table 7.1: Impact conditions and corresponding experimental observations

Name	[FS, Voltage (kV)]	Location of experimental observation (distance along the interface mm)	[α, V_{impact}] obtained at the same distance from CEMM simulation	Type*
straight	[Steel, 8]	7.65	[30°, 500m/s]	1
	[Cuprofor, 6]	6.75	[25°, 450m/s]	2
	[Cuprofor, 6]	5.00	[17.5°, 500m/s]	3
wave	[Cuprofor, 8]	6.75	[25°, 550m/s]	4
	[Cuprofor, 8]	7.50	[27.5°, 600m/s]	5

*Type: the classification of the various interface morphologies

Two types of straight interface (types 1 and 2 in Table 7.1) are shown in (Fig 7.1). The simulated straight interfaces show a reasonable agreement with the experimental observations, in terms of shape. It can be seen that the straight interface sometimes presents no welded zone (Figs. 7.1b and f). The temperature maps (Figs. 7.1c and d) do not predict values above the melting temperature of aluminium at the straight interface for both types of interfaces (see Table 7.1), which concurs with the experimental observations as shown in (Figs. 7.1e and f).

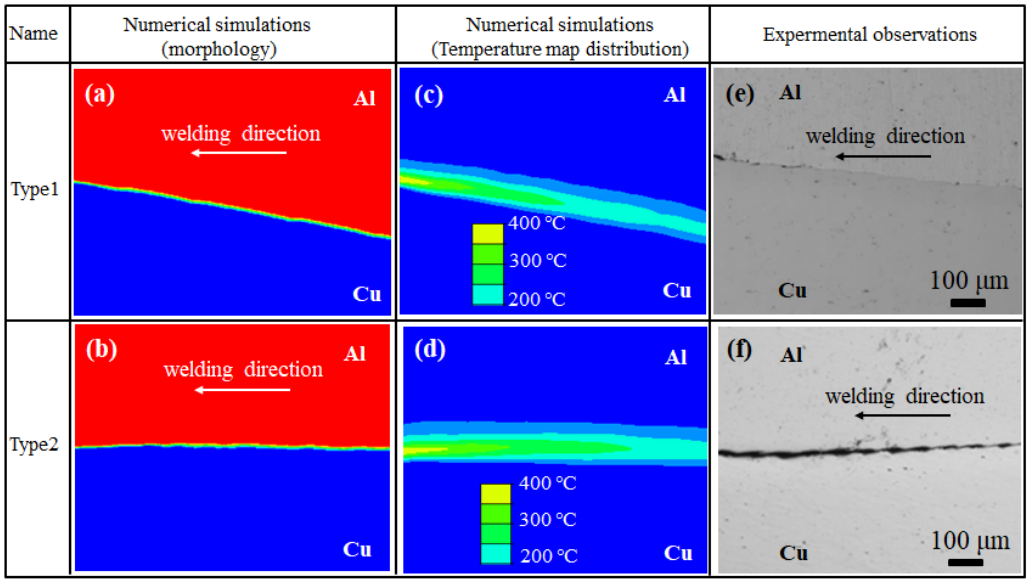

Fig. 7.1. Two types of straight interface morphologies obtained from the numerical simulations (a-b), corresponding temperature distributions (c-d) and experimental observations of the interface (e-f).

Fig. 7.2 shows the numerical predictions of three types of wave morphologies (Type 3-5 in the Table 7.1) and their comparison with the experimental observations. We can clearly see that the predicted waves (Figs. 7.2 a-c) concur well with the experimental observation in terms of wavy morphology pattern as shown in (Figs.7.2 g-i). The micrographs in (Figs. 7.2 g-i) without obvious intermetallic layers indicates that all the wavy interfaces have produced an effective weld without melting. The difference of these wave type depends on the size of the waves. The comparison between the wave Type 3 and 5 with the Type 4, shows that increasing impact

intensities (during the Types 3 and 5) leads to waves with larger amplitude (Figs. 6.12a and c). According to the works reported in [61] and [22], the grains near the wave interface with high amplitude experiences excessive deformation and the interfacial zone can presents extremely fine grains which could significantly increase the dislocation density and improve the ductility of the welded joint. This means below a certain range of safe impact intensity limit; one can increase the impact intensity to increase the wave amplitude so as to achieve a high quality welds. Figs. 7.2d-f display the temperature map of various waves. Similar to the straight interface (Figs. 7.1c and d), a local heating is also observed along the wave interface. However, the maximum temperatures of the wavy interfaces are higher than that of straight interfaces. But those maximum temperatures of the wavy interface are still lower than the melting point of aluminium (660 °C).

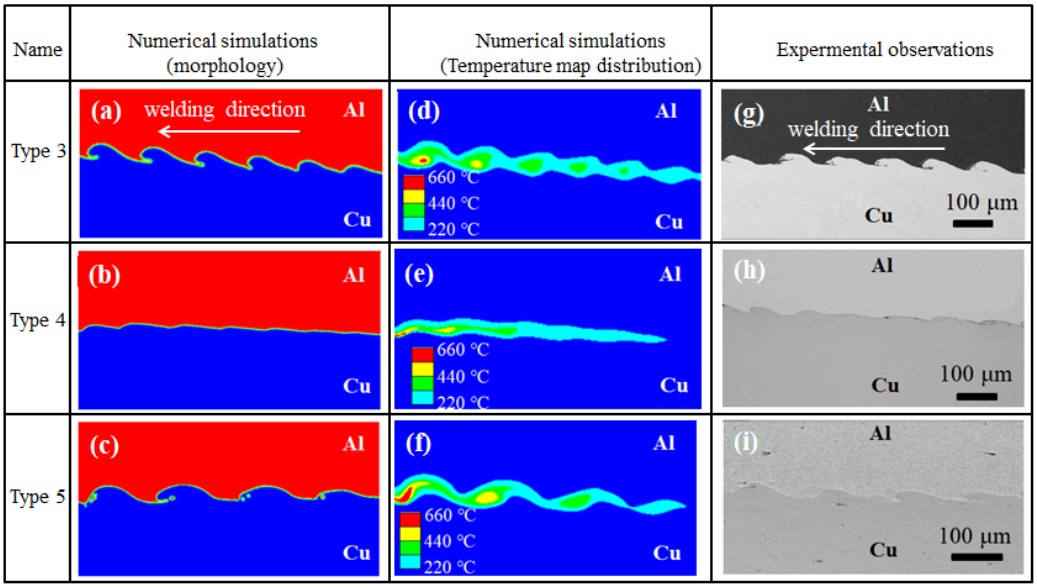

Fig. 7. 2. Three types of wave morphologies obtained from the numerical simulations (a-c), corresponding temperature distributions (d-f) and experimental observations of the waves (g-i).

7.2.2 Interface dynamics of a typical simulated interface

Various interfacial morphologies were predicted along the interface for a given initial impact condition. Therefore, in this section, we chose a typical simulation case

of [17.5°, 600m/s] to understand the formation mechanism of various instabilities along the simulated interface. The simulated interface includes four distinct interface features, i.e., (1) straight interface at the onset of welding (2) a generation of wavy interface, (3) a vortex development forming a complex intermixed interface (4) a cavity formation with the further interface instability, as shown in (Fig. 7.3a). The computed temperature map is shown in Fig. 7.3b. It confirms that a confined heating occurs along the whole interface, while the vortex and cavity zones show significant increase of local temperature (Fig. 7.3b).

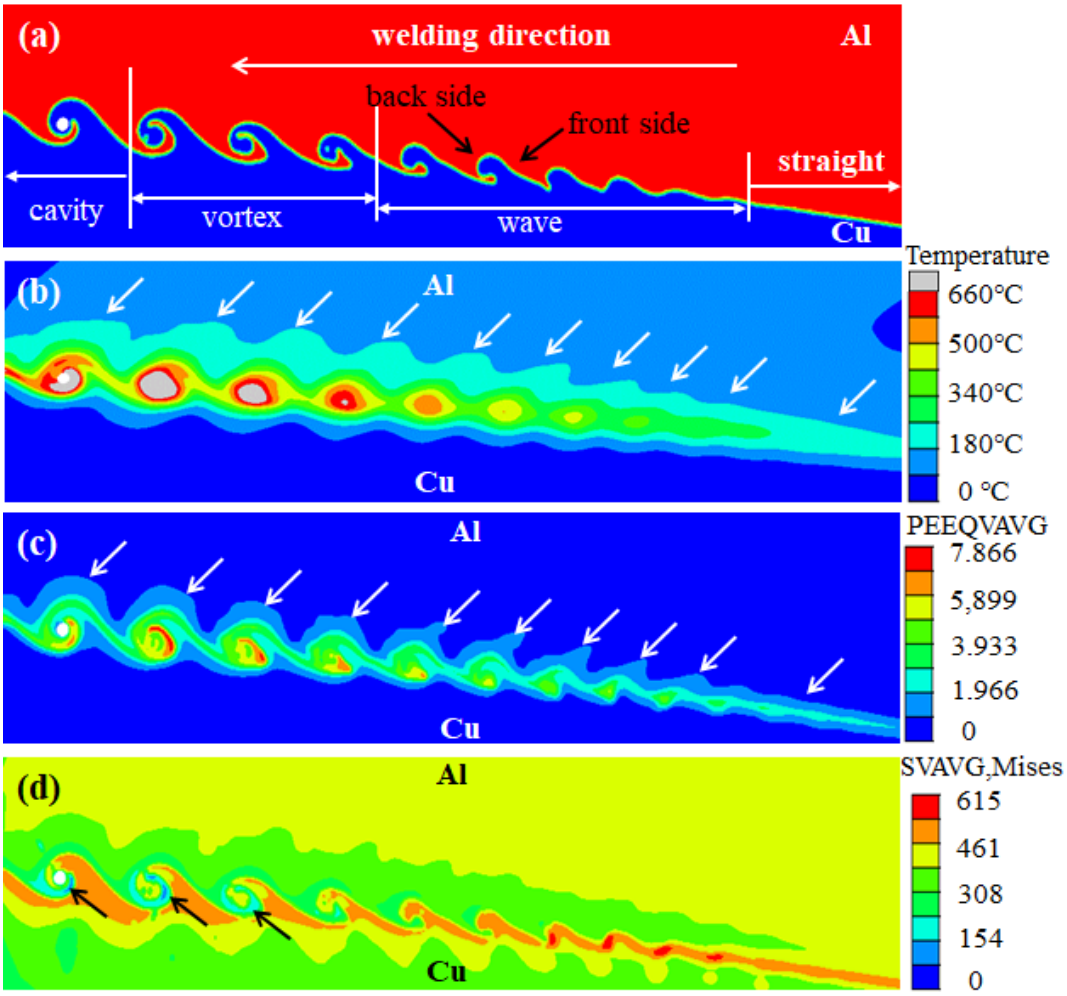

Fig. 7.3. The Eulerian simulation of a typical MPW case with the initial impact conditions of [17.5°, 600 m/s]; (a) sequential development of multiple interface morphologies; (b) temperature distribution along the interface; (c) averaged equivalent plastic strain along the interface; (d) averaged von Mises stress distribution along the interface.

Fig. 7.3c displays the distribution of PEEQVAVG (averaged equivalent plastic strain) along the interface, showing high values in the range of 0.95 to 7.87. Moreover, the strong plastic deformation is concentrated within the series of interface patterns. It is worth noting that the plastic strain and temperature quickly vanishes on the copper side than on the aluminium side (Figs. 7.3b and c). These phenomena can occur due to the following consequences: (1) the heat capacity in the aluminium is significantly higher than that in copper while the thermal conductivity of aluminium is significantly lower than that of copper, enabling higher temperature rise on aluminium side than on the copper side; and (2) it is expected that the aluminium becomes softer prior to the copper due to the higher melting temperature of copper, during the collision process Therefore, the aluminium side nearby the interface experiences a severely localized deformation. Therefore, it facilitates a large plastic strain localization on the aluminium side (Fig. 7.3c). Moreover, these above differences also influence the distribution of SAVAVG, Mises (averaged von Mises stresses) along the interface (Fig. 7.3d). The von Mises stresses are concentrated in both aluminium and copper side, and become lower away from the interface. Some places within the vortex and cavity zones present with near-zero von Mises stresses due to the material in these areas has already melted and lost the capacity to resist further deformation (marked by black arrows in Fig. 7.3d).

The dynamic parameters along the simulated interface (Fig. 7.3a) are further investigated to understand the evolution of interface morphologies. (Figs. 7. 4a and b) depicts the evolution of the dynamic angle and collision velocity along the interface, respectively, based on the analysis of each frame of the simulation. The dynamic angles constantly increase with the welding propagation (Fig. 7. 4a) and the highest dynamic angle can reach up to ~53°. Compared with the dynamic angle, the collision velocity experiences large fluctuations (Fig. 7. 4b). However, the collision velocity from the evolution of wave to vortex exhibits the reverse trend comparing with the dynamic angle, i.e., the collision velocity decreases with the welding propagation. It should be noted that when we combine the dynamic angle and collision velocity, we

can find a range of [collision angle, collision velocity] to produce a specific interface morphology. This range is used here to identify the weldability window which will be further discussed in the following section.

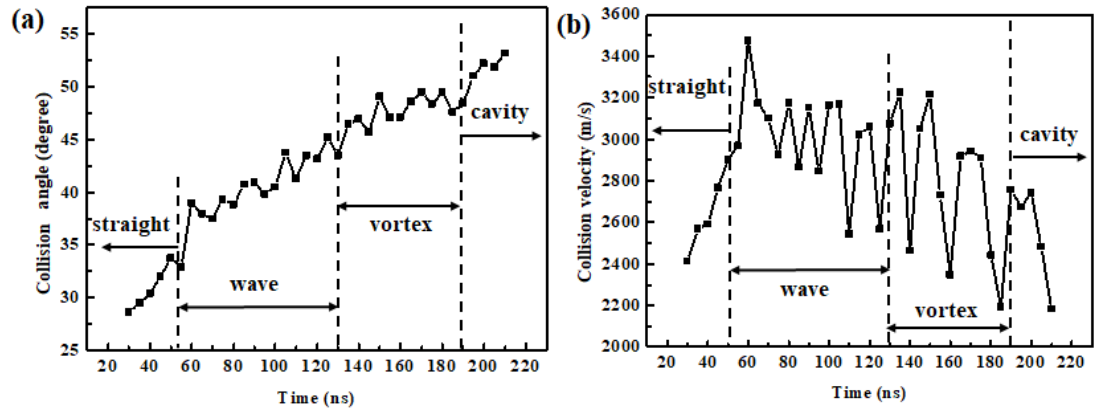

Fig. 7. 4. (a) collision angle and (b) collision velocity versus time along the interface obtained from Eulerian simulation.

Fig. 7.5a shows the values of the computed total mechanical strain rate along the interface that lies in between 2.01×10^8 s^{-1} and 2.07×10^9 s^{-1}. It reveals the interface material subjected to a high-strain rate collision during MPW and the strain rate has significantly fluctuate. The relationship between the ratio of "maximum positive shear stress/ maximum negative shear stress" and collision angle is depicted in Fig. 7.5b. The values of this ratio and the collision angle exhibit an approximately linear correlation, i.e., the collision angles increase with the stress ratio.

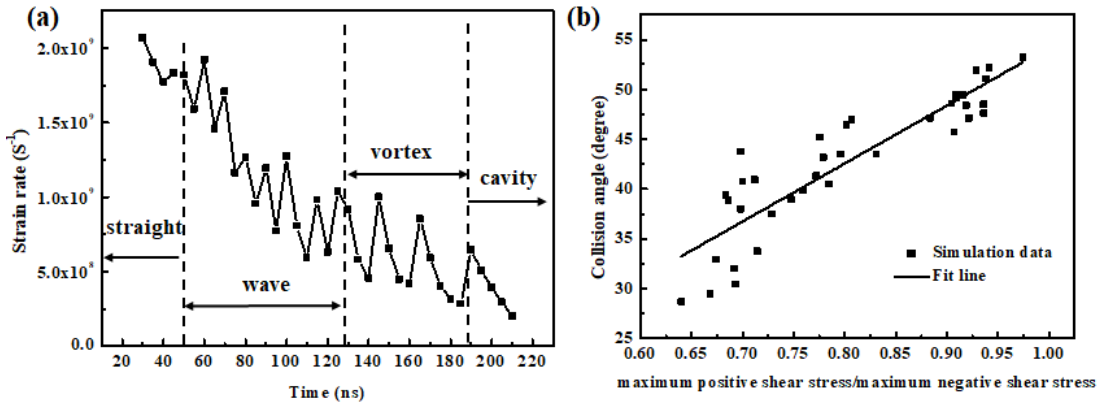

Fig. 7.5 (a) strain rate at collision point versus time obtained from Eulerian simulation, (b) relationship between the collision angle and the ratio of "maximum tensile shear stress/maximum compressive shear stress" at the interface.

7.2.3 Depiction of the weldability window

The previous sections reported various interface morphologies and further insights to determine a weldability window using numerical simulation. A significant number of simulations are required to build a weldability window. In total, 104 simulations with different impact conditions were carried out based on the coupled thermomechanical model. In our study, the impact velocity is from 300 m/s to 900m/s, and the impact angle ranged in between 12.5° and 30° to build a weldability window.

Since the interface morphologies are significantly influenced by the collision velocity and dynamic angle during the welding propagation, these two parameters are used to build the weldability window (Fig. 7.6). The collision velocity and dynamic angle were extracted from the positions corresponding to the specific simulated interface morphology. Assuming that the wavy morphology represents the successful joint formation, one can easily find the lower and right boundaries of the weldability window. This weldability window is usually regarded as the classical welding window using the collision velocity vs collision angle plot. This type of weldability windows is typically used for EXW processes where the collision velocity is directly given by the detonation velocity of the explosive. However, due to the nature of MPW process, the impact velocity is easier to control and access. Therefore, the weldability window for MPW has been developed based on the impact velocity and impact angle.

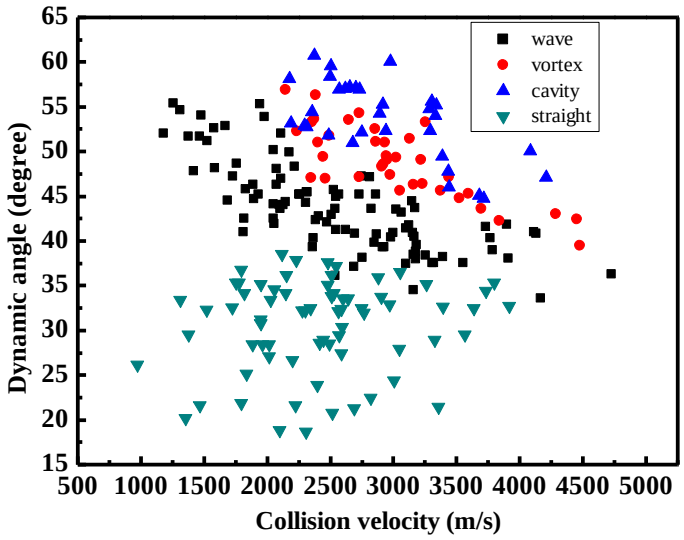

Fig. 7.6 Weldability window based on collision velocity and collision angle.

As we discussed in section 7.2.2, various interface morphologies can be produced during the simulation with the same initial impact conditions. Therefore, we calculate the percentage of each morphology to investigate the welding efficiency for each welding case. The maps of percentage of various interface morphologies based on the impact angle and impact velocity are shown in (Fig. 7.7a-e).

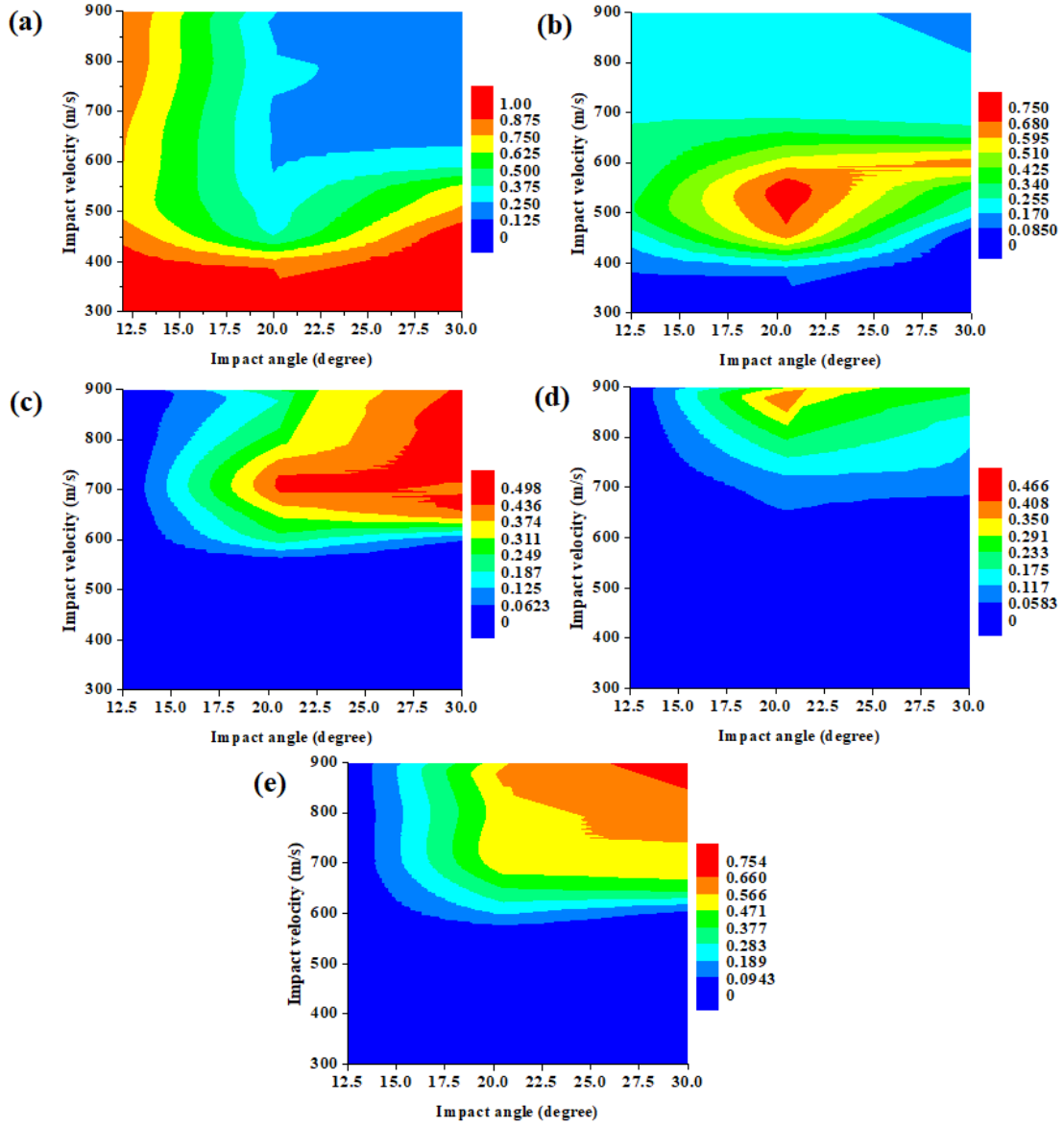

Fig. 7.7 A map showing the percentage of various interface morphologies in (a)-(e) based on the impact angle and impact velocity, wherein, (a), (b), (c), (d), and (e) represents straight, wavy, vortices, cavities and vortex +cavities, respectively.

The values of the right column of each figure represent the percentage. It is clearly seen that the map showing the percentage of straight interface presents an “L”

shape distribution (Fig. 7.7a). At low impact velocity, the impact intensity is not enough to deform the material below the input impact angle and thus the interface shows large percentage of straight interface. It is worth nothing that the combination of high impact velocity and low impact angle can also produce a high percentage of straight interface. This is because the high impact velocity generates high collision velocity leading to a fast welding propagation which results with insufficient time for the interface deformation to occur. As a consequence, the straight interface has a high possibility to contain thin melting layer. The map of wavy interface percentage shows a convex shape that clearly shows a suitable welding range for the combination of impact velocity and impact angle (Fig. 7.7b). One can find that the percentage of vortices and cavities increase under the combination of high impact velocity and high impact angle (Fig. 7. 7c-e). It clearly indicates that the high impact velocity can provide more impact energy while the high impact angle easily enables to form higher dynamic angle which facilitates for the formation of cavities and vortices along the interface, as discussed in section 7.2.2. Cavities and vortices are detrimental to the weld integrity and lead a catastrophic failure since micro cracks are usually initiated in these regions. Therefore, the impact conditions that induce the occurrence of cavities and vortices are considered as unsuitable welding parameters.

7.3. Conclusions

(1) The coupled thermomechanical model successfully predicts the straight interface and wavy interface in terms of morphology, shape and site occurrence.

(2) The straight interface, wavy interface, vortex and cavities are successively computed along the welding direction using Eulerian simulations. Dynamic collision angle constantly increases while the collision velocity decreases along the interface. The simulation results reveal differences in plastic strain, temperature and von Mises stress between the aluminium side and copper side; due to the differences in heat capacity, thermal conductivity and melting temperature. The collision angle increases with the the ratio of “maximum positive shear stress/maximum negative shear stress”.

(3) The map of percentage of straight and wavy morphologies on the impact velocity versus impact angle plot displays “L” shape distribution and convex shape tendency, respectively. A significant increase of vortices and cavities at the interface were observed at high impact velocity and high impact angle.

Chapter 8

Conclusions and perspectives

8.1 Specific contributions to the understanding of the interface dynamic behaviour of magnetic pulse welds

Effects of the welding conditions on the behaviours of Al/Cu magnetic pulse welds: the field-shaper materials and input discharge voltage play an important role on the local microstructure of the weld. The interface shearing instabilities increase with the electrical conductivity of field-shaper materials and the input discharge voltage. These shearing instabilities are essential to the evolution of the microstructure of the interface. Various interface features, i.e., wavy, swirls, vortex, IM layers, cracks and cavities, were found in the welding interfaces. The IM layers composed of Al_2Cu are formed by mechanical mixing combined with melting under low impact intensity. Under high impact intensity, the IM layers are totally melted and composed of Al_2Cu.

Local mechanical behaviour of the welding interface: the interface, especially the IM layers exhibit higher nano-hardness compared to base metal due to the presence of intermetallic compound and grain refinement. The IM layers were characterized by highly heterogeneous porous structure that leads to the heterogeneous nano-hardness in these regions. The nano-hardness increases with decreased porous density. In a P-h curve, IM layers with high porous density exhibits larger displacement shifts due to the increased dislocation mobility. It is suggested that a high strain rate during nanoindentation test can avoid the formation of "pop-in" events which could induce residual stresses on the IM layers.

Numerical predictions of the interface morphologies of the welds: our robust thermomechanical simulations successfully reproduce the various experimentally observed morphologies, i.e., various types of wave, wake, swirling structures, vortex and cavities, in terms of morphology and site occurrence. Moreover, the temperature

distribution and averaged equivalent plastic strain along the interface well correlate with the experimentally observed morphologies.

Thermomechanical kinematics generation during MPW process: Based on thermomechanical simulation for a wide variety of welding conditions, this study has shown that shear instability produces jetting kinematics and a confined plastic deformation along the interface. Moreover, this confined plastic deformation results in a confined heating that within a small surface layer along the interface. The confined heating regions may lead to an interface temperature above the melting point of base metal to promote the formation of IM phases and potential defects.

Wave formation: from the thermodynamic point of view, the wave formation is due to the shear instability including the jetting kinematics and non-uniform distribution of the tensile and compressive strains at the front and back sides of each wave. Moreover, the wave morphology is formed with repeated deformations of the interface rather than with a single-step deformation. From the metallurgical point of view, the wave experiences two bonding mechanisms, i.e., (i) a mixture of local melting and solid-state bonding and (ii) a solid-state bonding alone. The solid-state interface is composed with an interdiffusion zone that is caused by the mechanical lattice instability due to the high-pressure impact combined with an ultrahigh heating and cooling of 10^{13} °C s^{-1}. The wave morphologies are influenced by many parameters. A larger jetting angle enables to increase the vertical displacement of the waves and produces large wave amplitudes. Compared with the collision velocity, the ratio between collision velocity and impact velocity is more suitable for explaining the wavelength.

Wake and vortex formation: from the kinematics point of view, the formation of wake can be attributed to the combination of the successive indentation of protrusions arising from the ejecta and the intense shear instability at the interface. The formation of vortex occurs due to further interfacial shear instabilities and swirling phenomenon. From the thermodynamic point of view, the formation of wake is due to the double heating stages, i.e., the contact of ejecta and the onset of impact

while the formation of vortex is due to the triple heating stages, i.e., the contact of ejecta, the onset of impact and a swirling motion. These predictions also explain the specific solidified swirling trajectories within the experimental vortex.

Various types of pores formation: two types of pores, i.e., submicron and microscale pores, have been identified on the IM phases. The formation of submicron pores structure is due to the combination of the following phenomena: an ultra-high heating, a rapid expansion caused by a depressurization followed by a rapid cooling that facilitate the sequential phenomena of pore nucleation, a coalescence and growth within the melted zone. The trapped empty space during the drastic swirling in the vortex zone combined with the favourable thermomechanical conditions of the interface explains the formation of experimental microscale cavities within the IM phases.

Weldability window: the combinations of impact velocity in the range of 450-550 m/s and impact angle in the range of 17.5° and 22.5° have been found to produce above 50% wavy interface in the simulated welding interface. These welding conditions present a convex shape in the weldability window which are consider as suitable welding range since wavy is regarded to significantly improve the joint efficiency. High impact velocity and high impact angle cause the melting layers and cavities into the weld interface.

8.2 Perspectives

The following aspects are suggested as perspectives that come from results of this research work:

Investigate the effects of porous structures on the deformation behaviours of intermediate layers during nanoindentation test. According to our study, the formation of intermediate layers is inevitable in the magnetic pulse welds. It is necessary to understand the mechanical behaviours of these zones. The intermediate layers have been characterized with small area and porous structure in our study.

Therefore, it is difficult to gain more insight into the material deformation behaviours of these regions by *in-situ* nano-indentaion tests. A porous nano-indentation model based on the intermediate material could be suggested as a way to address this point.

Need to consider the axial symmetry problem. In our study, the position with a homogenous Lorentz force distribution (90° to the slot) was selected for analysis. However, there is still open discussion on the subject of symmetry for the tubular assembly welding cases. The Lorentz force is not uniform due to the presence of the slot in the field-shaper which may results in various interface morphologies. Therefore, further effects are necessary to work on different positions of the weld sample using in-situ experiments and simulations to reveal more insight on the MPW of tubular welding.

Apply the thermomechanical models to other different material combinations. The thermomechanical models have been validated on a specific MPW Al/Cu combination (i.e., the aluminium AA6060 T6 and pure copper). It would be interesting to validate these models on a wide range of dissimilar materials welding.

Explore the dynamic weldability windows. Our simulation studies already showed that higher plastic strain can melt the interface. It suggested that some dynamic parameters such as plastic strain, shear stress and shear strain may have a threshold to melt the interface for specific material combinations. Therefore, it is an interesting approach to use these dynamic parameters to build weldability windows. This can be used to inversely predict the impact conditions to identify the process parameters.

References

[1] M.F. Ashby, Y.J.M. Bréchet, Designing hybrid materials, Acta Materialia. 51 (2003), 5801–5821.

[2] T. Sapanathan, S. Khoddam, S.H. Zahiri, A. Zarei-Hanzaki, R. Ibrahim, Hybrid metallic composite materials fabricated by sheathed powder compaction, Journal of Materials Science. 51 (2016), 3118–3124.

[3] S. Khoddam, L. Tian, T. Sapanathan, P.D. Hodgson, A. Zarei-Hanzaki, Latest Developments in Modeling and Characterization of Joining Metal Based Hybrid Materials, Advanced Engineering Materials. 20 (2018), 1–26.

[4] M. Acarer, Electrical, corrosion, and mechanical properties of aluminum-copper joints produced by explosive welding, Journal of Materials Engineering and Performance. 21 (2012), 2375–2379.

[5] Welding Handbook, welding technology, 1 (1987).

[6] M.L. Su, J.S. Li, W.J. Qi, J.N. Li, Impact performance and microstructures of thick TA1 titanium alloy sheets welded by vacuum electron beam, Physica Scripta. 94 (2019), 115703.

[7] M.L. Su, J.N. Li, K.G. Liu, W.J. Qi, F. Weng, Y. Bin Zhang, J.S. Li, Mechanical property and characterization of TA1 titanium alloy sheets welded by vacuum electron beam welding, Vacuum. 159 (2019), 315-318.

[8] J.N. Li, J.S. Li, W.J. Qi, K.G. Liu, Characterization and mechanical properties of thick TC4 titanium alloy sheets welded joint by vacuum EBW, Vacuum. 168 (2019), 108812.

[9] M.-N. Avettand-Fènoël, A. Simar, A review about Friction Stir Welding of metal matrix composites, Materials Characterization. 120 (2016), 1–17.

[10] A. Simar, M.N. Avettand-Fènoël, Friction stir processing for architectured materials, Architectured Materials in Nature and Engineering. Springer Series in Materials Science, 282 (2019), 195-229.

[11] X. Chen, D. Inao, S. Tanaka, A. Mori, X. Li, K. Hokamoto, Explosive welding of Al alloys and high strength duplex stainless steel by controlling energetic conditions, Journal of Manufacturing Processes. 58 (2020), 1318–1333.

[12] G.H.S.F.L. Carvalho, I. Galvão, R. Mendes, R.M. Leal, A. Loureiro, Explosive welding of aluminium to stainless steel using carbon steel and niobium interlayers, Journal of Materials Processing Technology. 283 (2020), 116707.

[13] Z. Sun, C. Shi, F. Xu, K. Feng, C. Zhou, X. Wu, Detonation process analysis and interface morphology distribution of double vertical explosive welding by SPH 2D/3D numerical simulation and experiment, Materials &. Design. 191 (2020), 108630.

[14] S. Zhang, J. Lueg-Althoff, M. Hahn, A.E. Tekkaya, B.L. Kinsey, Effect of

process parameters on wavy interfacial morphology during magnetic pulse welding, Journal of Manufacturing Science and Engineering. 143 (2021), 011010.

[15] J.S. Li, R.N. Raoelison, T. Sapanathan, Z. Zhang, X.G. Chen, D. Marceau, Y.L. Hou, M. Rachik, An anomalous wave formation at the Al/Cu interface during magnetic pulse welding, Appl. Phys. Lett. 116 (2020), 161601.

[16] H. Wang, A. Vivek, Y. Wang, G. Taber, G.S. Daehn, Laser impact welding application in joining aluminum to titanium, Journal of Laser Applications. 28 (2016), 032002.

[17] X. Wang, M. Shao, H. Jin, H. Tang, H. Liu, Laser impact welding of aluminum to brass, Journal of Materials Processing Technology. 269 (2019), 190–199.

[18] J. Li, B. Schneiderman, S.M. Gilbert, A. Vivek, Z. Yu, G. Daehn, Process characteristics and interfacial microstructure in spot impact welding of titanium to stainless steel, Journal of Manufacturing Processes. 50 (2020), 421–429.

[19] A. Vivek, S.R. Hansen, B.C. Liu, G.S. Daehn, Vaporizing foil actuator: A tool for collision welding, Journal of Materials Processing Technology. 213 (2013), 2304–2311.

[20] T. Sapanathan, R.N. Raoelison, N. Buiron, M. Rachik, Magnetic Pulse Welding: An Innovative Joining Technology for Similar and Dissimilar Metal Pairs, Joining Technology. (2016), Chapter 11, 243-273.

[21] Chady KHALIL, Development ofMagnetic Pulse Welding process for welding dissimilar materials and joining polymeric composites to metals, PhD thesis, L'ÉCOLE CENTRALE DE NANTES, 2018.

[22] Y. Zhang, S.S. Babu, G.S. Daehn, Interfacial ultrafine-grained structures on aluminum alloy 6061 joint and copper alloy 110 joint fabricated by magnetic pulse welding, Journal of Materials Science. 45 (2010), 4645–4651.

[23] K.-J. Lee, S. Kumai, T. Arai, T. Aizawa, Interfacial microstructure and strength of steel/aluminum alloy lap joint fabricated by magnetic pressure seam welding, Material Science and Engineering A. 471 (2007), 95–101.

[24] J. Lueg-Althoff, J. Bellmann, S. Gies, S. Schulze, A.E. Tekkaya, E. Beyer, Influence of the flyer kinetics on magnetic pulse welding of tubes, Journal of Materials Processing Technology. 262 (2018), 189–203.

[25] M. Pourabbas, A. Abdollah-zadeh, M. Sarvari, M. Pouranvari, R. Miresmaeili, Investigation of structural and mechanical properties of magnetic pulse welded dissimilar aluminum alloys, Journal of Manufacturing Processes. 37 (2019), 292–304.

[26] T. Sapanathan, R.N. Raoelison, E. Padayodi, N. Buiron, M. Rachik, Depiction of interfacial characteristic changes during impact welding using computational methods: Comparison between Arbitrary Lagrangian - Eulerian and Eulerian simulations, Materials &. Design. 102 (2016), 303–312.

[27] R.N. Raoelison, T. Sapanathan, E. Padayodi, N. Buiron, M. Rachik, Interfacial kinematics and governing mechanisms under the influence of high strain rate impact conditions: Numerical computations of experimental observations, Journal of the Mechanics and Physics of Solids. 96 (2016) 147–161.

[28] D. N. Lysenko et al, METHOD OF PRESSURE WELDING, US Patent. US3520049A, July 14, 1970.

[29] T. Aizawa, M. Kashani, K. Okagawa, Application of magnetic pulse welding for aluminum alloys and SPCC steel sheet joints, Welding Journal. 86 (2007), 119–124.

[30] V. Shribman, Magnetic pulse welding of automotive HVAC parts, rapport technique, Pulsar Ltd. 8 (2007), 41–42.

[31] J. Bellmann, S. Schettler, S. Schulze, M. Wagner, J. Standfuss, M. Zimmermann, E. Beyer, C. Leyens, Improving and monitoring the magnetic pulse welding process between dissimilar metals, Welding in the World. (2020).

[32] Bruno Manuel Coelho Tomas, Magnetic pulse welding MPW, Master thesis, Universidade nova de lisboa, (2010).

[33] A. Kapil, A. Sharma, Magnetic pulse welding: An efficient and environmentally friendly multi-material joining technique, Journal of Cleaner Production. 100 (2015), 35–58.

[34] K. Faes, Electromagnetic pulse Tube Welding, International Impulse Forming Group, (2014).

[35] G. Zittel, A historical review of high speed metal forming, 4th International Conference on High Speed Forming, March 9th-10th 2010 Columbus, Ohio, USA. (2010), 2–15.

[36] T. Aizawa, K. Okagawa, M. Kashani, Application of magnetic pulse welding technique for flexible printed circuit boards (FPCB) lap joints, Journal of Materials Processing Technology. 213 (2013), 1095–1102.

[37] K. Mori, N. Bay, L. Fratini, F. Micari, A.E. Tekkaya, Joining by plastic deformation, CIRP Annals. 62 (2013), 673–694.

[38] M. Kashani, T. Aizawa, K. Okagawa, Y. Sugiyama, Welding of Manganin and Copper sheets by Using Magnetic Pulse Welding (MPW) Technique, IEICE Technical. Report. EMD. 109 (2009), 29–31.

[39] I. Kwee, V. Psyk, K. Faes, Effect of the Welding Parameters on the Structural and Mechanical Properties of Aluminium and Copper Sheet Joints by Electromagnetic Pulse Welding, World Journal of Engineering and Technology. 4 (2016), 538–561.

[40] F. Deng, Q. Cao, X. Han, L. Li, Electromagnetic pulse spot welding of aluminum to stainless steel sheets with a field shaper, The International Journal of Advanced Manufacturing Technology volume. 98 (2018) 1903–1911.

[41] T. Aizawa, Electromagnetic Energy Transmission in Magnetic Pulse Welding of Al / Cu Sheets using 1 , 3 , 4 and 6 Turn Flat Coils, Materials Science, 2017.

[42] V. Psyk, M. Linnemann, C. Scheffler, Experimental and numerical analysis of incremental magnetic pulse welding of dissimilar sheet metals, Manufacturing Review. 6 (2019), 7.

[43] R. Schäfer, P. Pasquale, Robot automated EMPT sheet welding, 5th International Conference on High Speed Forming, April 24th - 26th 2012, Dortmund, Germany, (2012), 189–196.

[44] R.N. Raoelison, J. Li, T. Sapanathan, E. Padayodi, N. Buiron, D. Racine, Z. Zhang, D. Marceau, M. Rachik, A new nature of microporous architecture with hierarchical porosity and membrane template via high strain rate collision, Materialia. 5 (2019), 100205.

[45] R.N. Raoelison, JS. Li, T. Sapanathan, M. Rachik, Instabilités à forte vitesse de déformation lors de collisions balistiques en soudage par impact et conséquences structurales et thermomécaniques. (Belfort, France, du 09/06/2020 au 12/06/2020). In: Annales du Congrès annuel de la SFT 2020.

[46] P.Q. Wang, D.L. Chen, Y. Ran, Y.Q. Yan, X.W. She, H. Peng, X.Q. Jiang, Electromagnetic pulse welding of Al/Cu dissimilar materials: Microstructure and tensile properties, Materials Science and Engineering: A. 792 (2020), 139842.

[47] R.N. Raoelison, D. Racine, Z. Zhang, N. Buiron, D. Marceau, M. Rachik, Magnetic pulse welding: Interface of Al/Cu joint and investigation of intermetallic formation effect on the weld features, Journal of Manufacturing Processes. 16 (2014), 427-434.

[48] M. Pourabbas, A. Abdollah-Zadeh, M. Sarvari, F. Movassagh-Alanagh, M. Pouranvari, Role of collision angle during dissimilar Al/Cu magnetic pulse welding, Science and Technology of Welding and Joining. 25 (2020), 549-555.

[49] X. Wu, J. Shang, An investigation of magnetic pulse welding of Al/Cu and interface characterization, Journal of Manufacturing Science and Engineering. 136 (2014), 051002.

[50] J.S. Li, R.N. Raoelison, T. Sapanathan, G. Racineux, M. Rachik. Assessing the influence of field-shaper material on magnetic pulse welded interface of Al/Cu joints. Procedia Manufacturing, 29(2019), 337-344.

[51] T. Sapanathan, R.N. Raoelison, K. Yang, N. Buiron, M. Rachik, Formation of porous inner architecture at the interface of magnetic pulse welded Al/Cu joints, AIP Conference Proceddings. 1769 (2016), 100011.

[52] R.N. Raoelison, T. Sapanathan, N. Buiron, M. Rachik, Magnetic pulse welding of Al/Al and Al/Cu metal pairs: Consequences of the dissimilar combination on the interfacial behavior during the welding process, Journal of Manufacturing Processes. 20 (2015), 112–127.

[53] J. Cui, L. Ye, C. Zhu, H. Geng, G. Li, Mechanical and Microstructure

Investigations on Magnetic Pulse Welded Dissimilar AA3003-TC4 Joints, Journal of Materials Engineering and Performance. 29 (2020), 712–722.

[54] M. Watanabe, S. Kumai, G. Hagimoto, Q. Zhang, K. Nakayama, Interfacial microstructure of aluminum/metallic glass lap joints fabricated by magnetic pulse welding, Materials Transactions. 50 (2009), 1279–1285.

[55] V. Shribman, Magnetic Pulse Welding for Dissimilar and Similar Materials, 3rd International Conference on High Speed Forming. (2008), 13–22.

[56] A. Ben-Artzy, A. Stern, N. Frage, V. Shribman, Interface phenomena in aluminium–magnesium magnetic pulse welding, Science and Technology of Welding and Joining. 13 (2008), 402–408.

[57] J. Cui, Y. Li, Q. Liu, X. Zhang, Z. Xu, G. Li, Joining of tubular carbon fiber-reinforced plastic/aluminum by magnetic pulse welding, Journal of Materials Processing Technology. 264 (2019), 273–282.

[58] D. Wang, N. Li, L. Liu, Magnetic pulse welding of a Zr-based bulk metallic glass with aluminum plate, Intermetallics. 93 (2018), 180–185.

[59] R. Shotri, K. Faes, A. De, Magnetic pulse welding of copper to steel tubes–Experimental investigation and process modelling, Journal of Manufacturing Processes. 58 (2020), 249–258.

[60] M. Watanabe, S. Kumai, Interfacial morphology of magnetic pulse welded aluminum/aluminum and copper/copper lap joints, Materials Transactions. 50 (2009), 286–292.

[61] R.N. Raoelison, N. Buiron, M. Rachik, D. Haye, G. Franz, M. Habak, Study of the elaboration of a practical weldability window in magnetic pulse welding, Journal of Materials Processing Technology. 213 (2013), 1348–1354.

[62] J. Cui, S. Wang, W. Yuan, G. Li, Effects of Standoff Distance on Magnetic Pulse Welded Joints Between Aluminum and Steel Elements in Automobile Body, Automotive Innovation. 3 (2020), 231–241.

[63] S.D. Kore, P.P. Date, S. V Kulkarni, Electromagnetic impact welding of aluminum to stainless steel sheets, Journal of Materials Processing Technology. 208 (2008), 486–493.

[64] M. Marya, S. Marya, D. Priem, On the characteristics of electromagnetic welds between aluminium and other metals and alloys, Welding in the World. 49 (2005), 74–84.

[65] Z. Fan, H. Yu, C. Li, Plastic deformation behavior of bi-metal tubes during magnetic pulse cladding: FE analysis and experiments, Journal of Materials Processing Technology. 229 (2016), 230–243.

[66] A.K. Rajak, S.D. Kore, Application of electromagnetic forming in terminal crimping using different types of field shapers, Journal of Mechanical Science and Technology. 32 (2018), 4291–4297.

[67] B. Saadouki, T. Sapanathan, P.H. Pelca, M. Elghorba, M. Rachik, Fatigue damage in fieldshapers used during electromagnetic forming and welding processes at high frequency impulse current, International Journal of Fatigue. 109 (2018), 93–102.

[68] R. Shotri, G. Racineux, A. De, Magnetic pulse welding of metallic tubes–experimental investigation and numerical modelling, Science and Technology of Welding and Joining. 25 (2020), 273-281.

[69] J.S. Li, R.N. Raoelison, T. Sapanathan, Y.L. Hou, M. Rachik, Interface evolution during magnetic pulse welding under extremely high strain rate collision: mechanisms, thermomechanical kinetics and consequences, Acta Materialia. 195 (2020), 404-415.

[70] Y. Zhang, S.S. Babu, C. Prothe, M. Blakely, J. Kwasegroch, M. LaHa, G.S. Daehn, Application of high velocity impact welding at varied different length scales, Journal of Materials Processing Technology. 211 (2011), 944–952.

[71] J.S. Li, T. Sapanathan, R.N. Raoelison, Z. Zhang, X.G. Chen, D. Marceau, A. Simar, M. Rachik, Inverse prediction of local interface temperature during electromagnetic pulse welding via precipitate kinetics, Materials. Letters. 249 (2019), 177–179.

[72] S. Hisashi, S. Isao, R. Sherif, M. Hidekazu, Numerical Study of Joining Process in Magnetic Pressure Seam Welding Transactions of JWRI, 38 (2009), 63–68.

[73] Z. Fan, H. Yu, C. Li, Interface and grain-boundary amorphization in the Al/Fe bimetallic system during pulsed-magnetic-driven impact, Scripta. Materialia. 110 (2016), 14–18.

[74] H. Geng, J. Mao, X. Zhang, G. Li, J. Cui, Formation mechanism of transition zone and amorphous structure in magnetic pulse welded Al-Fe joint, Materials. Letters. 245 (2019), 151–154.

[75] A. Nassiri, T. Abke, G. Daehn, Investigation of melting phenomena in solid-state welding processes, Scripta. Materialia. 168 (2019), 61–66.

[76] H. Yu, Z. Xu, Z. Fan, Z. Zhao, C. Li, Mechanical property and microstructure of aluminum alloy-steel tubes joint by magnetic pulse welding, Materials Science and Engineering: A. 561 (2013), 259–265.

[77] W.F. Brown, J. Bandas, N.T. Olson, Pulsed magnetic welding of breeder reactor fuel pin end closures, Transactions of the American Nuclear Society. 30 (1978), 186-187.

[78] K. Faes, T. Baaten, W. De Waele, N. Debroux, Joining of Copper to Brass Using Magnetic Pulse Welding, 4th International Conference on High Speed Forming, Columbus, (2010), 84-96.

[79] K. Faes, I. Kwee, W. De Waele, Electromagnetic pulse welding of tubular products: Influence of process parameters and workpiece geometry on the joint characteristics and investigation of suitable support systems for the target tube,

Metals. 9 (2019), 514.

[80] E. Uhlmann, L. Prasol, A. Ziefle, Potentials of pulse magnetic forming and joining, Advanced Materials Research. 907 (2014), 349–364.

[81] V. Psyk, D. Risch, B.L. Kinsey, A.E. Tekkaya, M. Kleiner, Electromagnetic forming—A review, Journal of Materials Processing Technology. 211 (2011), 787–829.

[82] M. Hahn, C. Weddeling, J. Lueg-Althoff, A.E. Tekkaya, Analytical approach for magnetic pulse welding of sheet connections, Journal of Materials Processing Technology. 230 (2016), 131–142.

[83] G. Göbel, J. Kaspar, T. Herrmannsdörfer, B. Brenner, E. Beyer, Insights into intermetallic phases on pulse welded dissimilar metal joints, 4th International Conference on High Speed Forming. (2010), 127–136.

[84] P. Groche, M.F.X. Wagner, C. Pabst, S. Sharafiev, Development of a novel test rig to investigate the fundamentals of impact welding, Journal of Materials Processing Technology. 214 (2014), 2009-2017.

[85] B.-H. Yoon, J.-Y. Shim, B.-Y. Kang, Joint Properties of Dissimilar Al/Steel Sheets Formed by Magnetic Pulse Welding, Journal of Welding and Joining. 38 (2020), 374–379.

[86] H. Yu, Y. Tong, Magnetic pulse welding of aluminum to steel using uniform pressure electromagnetic actuator, The International Journal of Advanced Manufacturing Technology. 91 (2017), 2257–2265.

[87] A. Stern, M. Aizenshtein, G. Moshe, S.R. Cohen, N. Frage, The nature of interfaces in Al-1050/Al-1050 and Al-1050/Mg-AZ31 Couples Joined by Magnetic Pulse Welding (MPW), Journal of Materials Engineering and Performance. 22 (2013), 2098–2103.

[88] M.-N. Avettand-Fènoël, M. Marinova, R. Taillard, Atomic scale characterization of a pure Al – galvanized steel spot magnetic pulse joint interface, Materials Characterization. 153 (2019), 251–260.

[89] T. Sapanathan, R.N. Raoelison, N. Buiron, M. Rachik, In situ metallic porous structure formation due to ultra high heating and cooling rates during an electromagnetic pulse welding, Scripta. Materialia. 128 (2017), 10–13.

[90] A. Garg, A. Bhattacharya, Strength and failure analysis of similar and dissimilar friction stir spot welds: Influence of different tools and pin geometries, Materials &. Design. 127 (2017), 272–286.

[91] S.D. Kore, J. Imbert, M.J. Worswick, Y. Zhou, Electromagnetic impact welding of Mg to Al sheets, Science and Technology of Welding and Joining. 14 (2009), 549–553.

[92] H. Geng, Z. Xia, X. Zhang, G. Li, J. Cui, Microstructures and mechanical properties of the welded AA5182/HC340LA joint by magnetic pulse welding,

Materials Characterization. 138 (2018), 229–237.

[93] S. Patra, K.S. Arora, M. Shome, S. Bysakh, Interface characteristics and performance of magnetic pulse welded copper-Steel tubes, Journal of Materials Processing Technology. 245 (2017), 278–286.

[94] J. Cui, G. Sun, J. Xu, Z. Xu, X. Huang, G. Li, A study on the critical wall thickness of the inner tube for magnetic pulse welding of tubular Al–Fe parts, Journal of Materials Processing Technology. 227 (2016), 138–146.

[95] H. Geng, J. Mao, X. Zhang, G. Li, J. Cui, Strain rate sensitivity of Al-Fe magnetic pulse welds, Journal of Materials Processing Technology. 262 (2018), 1–10.

[96] M. Watanabe, K. Ishiuchi, S. Kumai, Interfacial microstructure and hardness of magnetic pulse welded copper/nickel lap joint, Materials Transactions. 59 (2018), 425-431.

[97] H. Yu, H. Dang, Y. Qiu, Interfacial microstructure of stainless steel/aluminum alloy tube lap joints fabricated via magnetic pulse welding, Journal of Materials Processing Technology. 250 (2017), 297–303.

[98] A. Stern, M. Aizenshtein, Magnetic pulse welding of Al to Mg alloys: Structural-mechanical properties of the interfacial layer, Materials Science and Technology. 27 (2011), 1809–1813.

[99] N. Wang, W.Y. Yu, B.Y. Tang, L.M. Peng, W.J. Ding, Structural and mechanical properties of Mg17Al12 and Mg24Y5 from first-principles calculations, Journal of Physics D: Applied. Physics. 41 (2008), 3–8.

[100] A. Berlin, T.C. Nguyen, M.J. Worswick, Y. Zhou, Metallurgical analysis of magnetic pulse welds of AZ31 magnesium alloy, Science and Technology of Welding and Joining. 16 (2011), 728–734.

[101] J. Cui, G. Sun, G. Li, Z. Xu, P.K. Chu, Specific wave interface and its formation during magnetic pulse welding, Applied Physics Letters, 105 (2014), 221901.

[102] T. Sato, K. Kawauchi, A. Muto, Magnetic impulse welding of aluminium tube and copper tube with various core materials, Welding International. 12 (1998), 619–626.

[103] I.A. Bataev, S. Tanaka, Q. Zhou, D.V. Lazurenko, A.M.J. Junior, A.A. Bataev, K. Hokamoto, A. Mori, P. Chen, Towards better understanding of explosive welding by combination of numerical simulation and experimental study, Materials &. Design. 169 (2019), 107649.

[104] A.S. Bahrani, T. J. Black, B. Crossland, The mechanics of wave formation in explosive welding, Philosophical Magazine. 296 (1967), 123-136.

[105] E. Carton, Wave forming mechanisms in explosive welding, Materials Science Forum, 465–466 (2004), 219-224.

[106] A. Ben-Artzy, A. Stern, N. Frage, V. Shribman, O. Sadot, Wave formation mechanism in magnetic pulse welding, International Journal of Impact Engineering. 37 (2010), 397–404.

[107] J.L. Robinson, The mechanics of wave formation in impact welding, Philosophical Magazine. 31 (1975), 587–597.

[108] A. Nassiri, B. Kinsey, G. Chini, Shear instability of plastically-deforming metals in high-velocity impact welding, Journal of the Mechanics and Physics of Solids. 95 (2016), 351–373.

[109] T. Lee, S. Zhang, A. Vivek, G. Daehn, B. Kinsey, Wave formation in impact welding: Study of the Cu–Ti system, CIRP Annals. 68 (2019), 261–264.

[110] S.R. Reid, A discussion of the mechanism of interface wave generation in explosive welding, International Journal of Mechanical Sciences. 16 (1974), 399–413.

[111] G.R. Cowan, O.R. Bergmann, A.H. Holtzman, Mechanism of bond zone wave formation in explosion-clad metals, Metallurgical and Materials Transactions B. 2 (1971), 3145–3155.

[112] S.D. Kore, P. Dhanesh, S. V. Kulkarni, P.P. Date, Numerical modeling of electromagnetic welding, International Journal of Applied Electromagnetics and Mechanics, 32 (2010), 1-19.

[113] S.R. Reid, Wake instability mechanism for wave formation in explosive welding, International Journal of Mechanical Sciences. 20 (1978), 247–253.

[114] J.F. Kowalick, D.R. Hay, A mechanism of explosive bonding, Metallurgical Transactions. 2 (1971), 1953-1958.

[115] X. Wang, X. Wang, F. Li, J. Lu, H. Liu, Interface Kinematics of Laser Impact Welding of Ni and SS304 Based on Jet Indentation Mechanism, Metallurgical and Materials Transactions A. 51 (2020), 2893-2904.

[116] A. Vivek, B.C. Liu, S.R. Hansen, G.S. Daehn, Accessing collision welding process window for titanium/copper welds with vaporizing foil actuators and grooved targets, Journal of Materials Processing Technology. 214 (2014), 1583–1589.

[117] M. Hartmann, G. Mahler, O. Hess, Fundamentals of Nano-Thermodynamics, Materials Science, (2004), 117–126.

[118] M. Chizari, S.T.S. Al-Hassani, L.M. Barrett, Effect of flyer shape on the bonding criteria in impact welding of plates, Journal of Materials Processing Technology. 209 (2009), 445–454.

[119] T. Lee, S. Zhang, A. Vivek, B. Kinsey, G. Daehn, Flyer thickness effect in the impact welding of aluminum to steel, Journal of Manufacturing Science and Engineering. 140 (2018), 121002.

[120] A. Nassiri, G. Chini, A. Vivek, G. Daehn, B. Kinsey, Arbitrary

Lagrangian–Eulerian finite element simulation and experimental investigation of wavy interfacial morphology during high velocity impact welding, Materials &. Design. 88 (2015), 345–358.

[121] A. Nassiri, G. Chini, B. Kinsey, Spatial stability analysis of emergent wavy interfacial patterns in magnetic pulsed welding, CIRP Annals. 63 (2014), 245–248.

[122] S. Zhang, B. Kinsey, Interfacial Morphology Prediction of Impact Welding by Eulerian Method, 8th International Conference on High Speed Forming. (2018).

[123] W. Xu, X. Sun, Numerical investigation of electromagnetic pulse welded interfaces between dissimilar metals, Science and Technology of Welding and Joining. 21 (2016), 592–599.

[124] S.P. Kiselev, V.I. Mali, Numerical and experimental modeling of jet formation during a high-velocity oblique impact of metal plates, Combustion, Explosion, and Shock Waves. 48 (2012), 214-225.

[125] S.P. Kiselev, Numerical simulation of wave formation in an oblique impact of plates by the method of molecular dynamics, Journal of Applied Mechanics and Technical Physics. 53 (2012), 907-917.

[126] O. Saresoja, A. Kuronen, K. Nordlund, Atomistic simulation of the explosion welding process, Advanced Engineering Materials. 12 (2012), 201100211.

[127] J. Cheng, X. Hu, X. Sun, A. Vivek, G. Daehn, D. Cullen, Multi-scale characterization and simulation of impact welding between immiscible Mg/steel alloys, Journal of Materials Science & Technology. 59 (2020), 149–163.

[128] Y. Y. Emurlaeva, N. S. Aleksandrova, I. A. Bataev, SPH simulation of plastic deformation in high velocity impact welding process of 6061-T6 alloy plates, IOP Conference Series: Materials Science and Engineering 795 (2020), 012003.

[129] S. J. Chen, X. Q. Jiang, Microstructure evolution during magnetic pulse welding of dissimilar aluminium and magnesium alloys, Journal of Manufacturing Processes, 19 (2015), 14-21.

[130] T. Lee, A. Nassiri, T. Dittrich, A. Vivek, G. Daehn, Microstructure development in impact welding of a model system, Scripta Materialia. 178 (2020), 203—206.

[131] Q. Chu, M. Zhang, J. Li, C. Yan, Experimental and numerical investigation of microstructure and mechanical behavior of titanium/steel interfaces prepared by explosive welding, Materials Science and Engineering: A. 689 (2017), 323–331.

[132] S.A.A. Akbari Mousavi, S.T.S. Al-Hassani, Finite element simulation of explosively-driven plate impact with application to explosive welding, Materials &. Design. 29 (2008), 1–19.

[133] A.A. Akbari Mousavi, S.T.S. Al-Hassani, Numerical and experimental

studies of the mechanism of the wavy interface formations in explosive/impact welding, Journal of the Mechanics and Physics of Solids. 53 (2005), 2501–2528.

[134] F. Management, Coupled FEM-Simulation of Magnetic Pulse Welding for Nonsymmetric Applications, 5th International Conference on High Speed Forming, April 24th - 26th 2012, Dortmund, Germany, (2012), 303–314.

[135] X. Wang, Y. Zheng, H. Liu, Z. Shen, Y. Hu, W. Li, Y. Gao, C. Guo, Numerical study of the mechanism of explosive/impact welding using Smoothed Particle Hydrodynamics method, Materials &. Design. 35 (2012), 210–219.

[136] X. Wang, Y. Gu, T. Qiu, Y. Ma, D. Zhang, H. Liu, An experimental and numerical study of laser impact spot welding, Materials &. Design. 65 (2015), 1143–1152.

[137] R. Raoelison, M. Rachik, N. Buiron, D. Haye, M. Morel, B. Dos, D. Jouaffre, G. Frantz, Determination of the Welding Conditions and Weldability Window in Magnetic Pulse Welding, 5th International Conference on High Speed Forming. (2012).

[138] M. M. H. Athar, B. Tolaminejad, Weldability window and the effect of interface morphology on the properties of Al/Cu/Al laminated composites fabricated by explosive welding, Materials &. Design. 86 (2015), 516–525.

[139] J.B. Ribeiro, R. Mendes, A. Loureiro, Review of the weldability window concept and equations for explosive welding, Journal of Physics: Conference Series. 500 (2014), 052038.

[140] S.A.A. Akbari Mousavi, P. Farhadi Sartangi, Experimental investigation of explosive welding of cp-titanium/AISI 304 stainless steel, Materials &. Design. 30 (2009), 459–468.

[141] R.N. Raoelison, N. Buiron, M. Rachik, D. Haye, G. Franz, Efficient welding conditions in magnetic pulse welding process, Journal of Manufacturing Processes. 14 (2012), 372–377.

[142] Y. Zhang, S.S. Babu, G.S. Daehn, Impact Welding in a Variety of Geometric Configurations, 4th International Conference on High Speed Forming, March 9th-10th 2010 Columbus, Ohio, USA, (2010).

[143] I. V. Oliveira, A.J. Cavaleiro, G.A. Taber, A. Reis, Magnetic pulse welding of dissimilar materials: Aluminum-copper, In: Silva L. (eds) Materials Design and Applications. Advanced Structured Materials, 65 (2017), 419–431.

[144] V. Psyk, C. Scheffler, M. Linnemann, D. Landgrebe, Manufacturing of hybrid aluminum copper joints by electromagnetic pulse welding - Identification of quantitative process windows, AIP Conference Proceedings. 1896 (2017), 110001.

[145] A. Nassiri, G.P. Chini, B.L. Kinsey, Arbitrary Lagrangian Eulerian FEA Method to Predict Wavy Pattern and Weldability Window During Magnetic Pulsed Welding, ASME 2015 International Manufacturing Science and

Engineering Conference, June 8–12, 2015 Charlotte, North Carolina, USA (2015), 1–6.

[146] D. Risch, J. Nebel, V. Psyk, E. Vogli, W. Tillmann, A.E. Tekkaya, Hybrid Material Design for Coils Used in Electromagentic Forming Processes, Proceedings of the 7th International Conference Coatings in Manufacturing Engineering, 1-3 October 2008, Chalkidiki, Greece. (2008), 269–278.

[147] Y. Zhang, Investigation of magnetic pulse welding on lap joint of similar and dissimilar materials, PhD thesis, The Ohio State University, 2010.

[148] T.T. Zhang, W.X. Wang, J. Zhou, X.Q. Cao, Z.F. Yan, Y. Wei, W. Zhang, Investigation of Interface Bonding Mechanism of an Explosively Welded Tri-Metal Titanium/Aluminum/Magnesium Plate by Nanoindentation, JOM. 70 (2018), 504–509.

[149] A. Kapil, T. Lee, A. Vivek, R. Cooper, E. Hetrick, G. Daehn, Spot impact welding of an age-hardening aluminum alloy: Process, structure and properties, Journal of Manufacturing Processes. 37 (2019), 42–52.

[150] T. Sapanathan, N. Jimenez-Mena, I. Sabirov, M.A. Monclús, J.M. Molina-Aldareguía, P. Xia, L. Zhao, A. Simar, A new physical simulation tool to predict the interface of dissimilar aluminum to steel welds performed by friction melt bonding, Journal of Materials Science & Technology. 35 (2019), 2048–2057.

[151] K. Wang, S.-L. Shang, Y. Wang, A. Vivek, G. Daehn, Z.-K. Liu, J. Li, Unveiling non-equilibrium metallurgical phases in dissimilar Al-Cu joints processed by vaporizing foil actuator welding, Materials &. Design. 186 (2020), 108306.

[152] D. Andre, T. Burlet, F. Körkemeyer, G. Gerstein, J.S.K.-L. Gibson, S. Sandlöbes-Haut, S. Korte-Kerzel, Investigation of the electroplastic effect using nanoindentation, Materials &. Design. 183 (2019), 108153.

[153] C.A. Schuh, Nanoindentation studies of materials, Materials Today. 9 (2006), 32–40.

[154] C.A. Schuh, T.G. Nieh, A nanoindentation study of serrated flow in bulk metallic glasses, Acta Materialia. 51 (2003), 87–99.

[155] A. Loureiro, R. Mendes, J.B. Ribeiro, R.M. Leal, I. Galvão, Effect of explosive mixture on quality of explosive welds of copper to aluminium, Materials &. Design. 95 (2016), 256-267.

[156] S.-P. Wang, J. Xu, Incipient plasticity and activation volume of dislocation nucleation for TiZrNbTaMo high-entropy alloys characterized by nanoindentation, Journal of Materials Science & Technology. 35 (2019), 812–816.

[157] C.J. Ruestes, E.M. Bringa, A. Stukowski, J.F. Rodríguez Nieva, Y. Tang, M.A. Meyers, Plastic deformation of a porous bcc metal containing nanometer

sized voids, Computational Materials Science. 88 (2014), 92–102.

[158] P. Groche, M. Becker, C. Pabst, Process window acquisition for impact welding processes, Materials &. Design. 118 (2017), 286–293.

[159] P. L'Eplattenier, G. Cook, C. Ashcraft, M. Burger, J. Imbert, M. Worswick, Introduction of an electromagnetism module in LS-DYNA for coupled mechanical-thermal-electromagnetic simulations, Steel Research International. 80 (2009), 351-358.

[160] K. Kondo, M. Makino, Crash simulation of large-number-of-elements car model by LS-DYNA on highly parallel computers, Computer Science Fujitsu Scientific & Technical Journal. 44 (2008), 467-474.

[161] Y.-Y. Lin, J. Wang, Performance of the Hybrid LS-DYNA on Crash Simulation with the Multicore Architecture, 7th European LS-DYNA Conference, (2009).

[162] N.K. Gupta, M.A. Iqbal, G.S. Sekhon, Experimental and numerical studies on the behavior of thin aluminum plates subjected to impact by blunt- and hemispherical-nosed projectiles, International Journal of Impact Engineering. 32 (2006), 1921–1944.

[163] V. Gupta, T. Lee, A. Vivek, K.S. Choi, Y. Mao, X. Sun, G. Daehn, A robust process-structure model for predicting the joint interface structure in impact welding, Journal of Materials Processing Technology. 264 (2019), 107–118.

[164] A.H. Clausen, T. Børvik, O.S. Hopperstad, A. Benallal, Flow and fracture characteristics of aluminium alloy AA5083-H116 as function of strain rate, temperature and triaxiality, Material Science and Engineering A. 364 (2004), 260–272.

[165] V.S. J.-P. Cuq-Lelandais, G. Avrillaud, S. Ferreira, G. Mazars, A. Nottebaert, G. Teilla, 3D Impacts Modeling of the Magnetic Pulse Welding Process and Comparison to Experimental Data, 7th International Conference on High Speed Forming, April 27th-28th 2016, Dortmund, Germany, (2016), 13–22.

[166] V. Psyk, C. Hofer, K. Faes, C. Scheffler, E. Scherleitner, Testing of magnetic pulse welded joints - Destructive and non-destructive methods, AIP Conference Proceedings. 2113 (2019), 050010.

[167] V.I. Lysak, S. V. Kuzmin, Lower boundary in metal explosive welding. Evolution of ideas, Journal of Materials Processing Technology. 212 (2012), 150–156.

[168] P. Parchuri, S. Kotegawa, H. Yamamoto, K. Ito, A. Mori, K. Hokamoto, Benefits of intermediate-layer formation at the interface of Nb/Cu and Ta/Cu explosive clads, Materials &. Design. 166 (2019), 107610.

[169] A. Stern, V. Shribman, A. Ben-Artzy, M. Aizenshtein, Interface Phenomena and Bonding Mechanism in Magnetic Pulse Welding, Journal of Materials Engineering and Performance. 23 (2014), 3449–3458.

[170] I.A. Bataev, D. V. Lazurenko, S. Tanaka, K. Hokamoto, A.A. Bataev, Y. Guo, A.M. Jorge, High cooling rates and metastable phases at the interfaces of explosively welded materials, Acta Materialia. 135 (2017), 277–289.

[171] V. V. Rybin, B.A. Greenberg, O. V. Antonova, O.A. Elkina, M.A. Ivanov, A. V. Inozemtsev, A.M. Patselov, I.I. Sidorov, Formation of vortices during explosion welding (titanium-orthorhombic titanium aluminide), The Physics of Metals and Metallography. 108 (2009), 353–364.

[172] I.A. Bataev, A.A. Bataev, V.I. Mali, V.G. Burov, E.A. Prikhod'ko, Formation and structure of vortex zones arising upon explosion welding of carbon steels, The Physics of Metals and Metallography. 113 (2012), 233–240.

[173] X. Jiang, S. Chen, Texture evolution and plastic deformation mechanism in magnetic pulse welding of dissimilar Al and Mg alloys, Welding in the World. 62 (2018), 1159–1171.

[174] A. Stern and M. Aizenshtein, On the Bonding Zone Formation in Magnetic Pulse Welds, Science and Technology of Welding and Joining, 7 (2002), 339–342.

[175] A. Nassiri, A. Vivek, T. Abke, B. Liu, T. Lee, G. Daehn, Depiction of interfacial morphology in impact welded Ti/Cu bimetallic systems using smoothed particle hydrodynamics, Applied Physics Letters. 110 (2017), 231601.

[176] O. Becher, M. Nahmany, D. Ashkenazi, V. Shribman, A. Stern, On bond formation in magnetic pulse welded joints, The Annals of "Dunarea de Jos" University of Galati. Fascicle XII : Welding Equipment and Technology. 25 (2014), 23-28.

[177] A. Stern, O. Becher, M. Nahmany, D. Ashkenazi, V. Shribman, Jet composition in magnetic pulse welding: Al-Al and Al-Mg couples, Welding Journal. 94 (2015), 257-264.

[178] A. Mao, J. Zhang, S. Yao, A. Wang, W. Wang, Y. Li, C. Qiao, J. Xie, Y. Jia, The diffusion behaviors at the Cu-Al solid-liquid interface: A molecular dynamics study, Results in Physics. 16 (2020), 102998.

[179] J.R. Rice, D.M. Tracey, On the ductile enlargement of voids in triaxial stress fields, Journal of the Mechanics and Physics of Solids. 17 (1969), 201–217.

[180] Y. Hamada, K. Koga, H. Tanaka, Phase equilibria and interfacial tension of fluids confined in narrow pores, The Journal of Chemical Physics. 127 (2007), 084908.

[181] N. Jimenez-Mena, T. Sapanathan, J.M. Drezet, T. Pirling, P.J. Jacques, A. Simar, Residual stresses of friction melt bonded aluminum/steel joints determined by neutron diffraction, Journal of Materials Processing and Technology. 266 (2019), 651–661.

[182] J.S. Li, T. Sapanathan, R.N. Raoelison, Y.L. Hou, A. Simar, M. Rachik, On the complete interface development for Al/Cu magnetic pulse welding via

experimental characterizations and multiphysics numerical simulations, Journal of Materials Processing Technlogy. 296 (2021), 117185.

[183] Kate Doyle. Here's everying you need to know about cyclons. ABC NEWS. accessed 18/03/2017.